Recommendations for the Analysis and Design of Naturally Ventilated Buildings in Urban Areas

by

Phan Hue Truong

B.A. Architecture, University of California, Berkeley (2004)
S.M. Arch. Studies, Massachusetts Institute of Technology (2010)

Submitted to the Department of Architecture
in partial fulfillment of the requirements for the degree of

Master of Science in Building Technology

at the

MASSACHUSETTS INSTITUTE OF TECHNOLOGY

February 2012

Author . . . .
Department of Architecture
January 19, 2012

Certified by . . . .
Leslie K. Norford
Professor of Building Technology
Thesis Supervisor

Accepted by . . . .
Takehiko Nagakura
Associate Professor of Design and Computation
Chair, Department Committee on Graduate Students

Rex E. Britter
Visiting Scientist, Senseable City Laboratory and Building Technology Group
Thesis Reader

Recommendations for the Analysis and Design of Naturally Ventilated Buildings in Urban Areas

by

Phan Hue Truong

Submitted to the Department of Architecture
on January 19, 2012, in partial fulfillment of the
requirements for the degree of
Master of Science in Building Technology

Abstract

The motivation behind this work was to obtain a better understanding of how a building's natural ventilation potential is affected by the complexities introduced by the urban environment. To this end, we have derived in detail the physical principles of wind- and buoyancy-driven natural ventilation for a standard apartment geometry, documented and analyzed the existing data on wind pressure coefficients in terms of urban morphological parameters, and examined the flow in the urban boundary layer and how it relates to the boundary layer at the rural site of the meteorological station. The information and understanding that emerged from this research has been assembled into a set of graphical methods and simple guidelines that can be applied by designers to the early design phases of natural ventilation projects in urban areas. These methods can be used to estimate indoor-outdoor temperature differences and airflow rates for several opening geometries. Our hope is for these methods to offer a good overview of how natural ventilation calculations can be applied to urban areas and to help resolve some of the main difficulties that a designer might encounter during this process. While the approach is primarily intended to inform decision-making during the beginning design stages, we imagine that, from applying it, designers will also acquire a more physical and intuitive understanding of how the forces of natural ventilation are altered in progressively denser urban sites and that this could also aid in the interpretation of results at the simulation stage.

Thesis Supervisor: Leslie K. Norford
Title: Professor of Building Technology

Acknowledgments

I want to thank Professors Les Norford and Rex Britter for their guidance, enthusiasm, and support throughout this past year. I also want to thank my colleagues Bruno Bueno and Terianne Hall for sharing their research with me during several stages of this project. This project was in part funded by the National Science Foundation Graduate Research Fellowship Program and I am grateful for their support.

To my parents, for their courage and never-ending hard work
and to Fred, we are a team.

Contents

List of Figures

List of Tables

Chapter 1

Introduction to natural ventilation in urban areas

As the world's population is rapidly becoming urbanized, with over half now living in cities [11], it is imperative to develop strategies of conservation and sustainability applicable to urban areas. In particular, energy-efficient strategies applied to buildings could significantly reduce the overall carbon footprint of cities. Natural ventilation is one such strategy that can provide thermal comfort to occupants by relying on natural driving forces as opposed to mechanical forces to ventilate and cool the interiors of buildings.

However, the study of natural ventilation of buildings is difficult since it requires a good understanding of the exterior airflows around the building as well as the physics that govern the flows through the interior of the building. For urban areas these exterior flows are often complex and quite different from the airflows usually observed around more isolated buildings. Hence, for a designer of naturally ventilated buildings in urban areas, it is essential to understand the complexities introduced by the urban environment and their impact on a building's natural ventilation potential.

This chapter introduces the basic driving forces of natural ventilation, continues with a discussion of the main difficulties associated with building natural ventilation studies in urban areas followed by a summary of the current state of research on the topic, and concludes with the motivation and approach behind the present work.

1.1 Driving forces of natural ventilation

Natural ventilation through openings in buildings is a result of pressure differences, which can be generated by wind forces, buoyancy forces, turbulent fluctuations, or more realistically, a combination of all of the above. This section defines each driving force and summarizes the relevant aspects.

1.1.1 Wind

For building ventilation studies, surface pressures due to wind are commonly expressed as mean surface wind pressure coefficients, C_p,

$$C_p = \frac{2(\overline{p} - p_{ref})}{\rho u_{ref}^2} \tag{1.1}$$

where $\overline{p}$ is the mean, time-averaged value of the instantaneous surface pressure, p_{ref} is an arbitrary reference pressure in the flow, ρ is the density of the air, and u_{ref} is an arbitrary reference velocity. Typically, the difference $\overline{p} - p_{ref}$ is simply a gauge pressure, the surface pressure not including the hydrostatic component [10]. For u_{ref}, a common reference condition is the velocity measured at building height at or near the location of the building; however this is not always the case and care should be taken to match the reference condition. Since the purpose for using pressure coefficients is to facilitate obtaining surface pressures, it is crucial that the velocity used to transform the pressure coefficient back to a surface pressure is taken at the same reference condition as the one that was originally used in deriving the pressure coefficient. Values of C_p defined at one reference condition should never be used with another [10].

Pressure coefficients can be based on a local pressure measurement at a point on a facade or computed as a surface-averaged value of the pressure measurements of a whole facade. In either case, values of C_p depend primarily on the wind direction, the geometry of the building, and the geometry of the surrounding environment [1]. While the surface pressure also depends on the magnitude of the wind speed, the pressure coefficient itself does not, as long as the flow is turbulent, which is the case for the high-Reynolds-number flows and sharp-edged geometries with which we are concerned. Hence, for the geometry of a given building and its surroundings and for a given wind direction, the mean pressure coefficients on the facades will be approximately independent of the wind speed [10].

1.1.2 Buoyancy

Temperature differences between the indoor and outdoor environment produce density differences and corresponding pressure differences that generate a buoyancy-driven flow through the building. This flow depends not only on the indoor-outdoor temperature difference, which is a function of the heat gains inside the zone, but also on the height between the openings. A special case of buoyancy-driven flow is set up for a zone that has windows placed at equal heights above the floor. If a thermal difference between the indoor and outdoor environment exists, bidirectional or two-way buoyancy-driven flow is obtained. In this case, the pressures are a function of the height of the opening. Figure 1-1 depicts the airflow paths and velocity profiles for bidirectional buoyancy-driven flow in the absence of wind forces for an indoor temperature that is larger than the outdoor temperature. Cooler outdoor air enters through the lower half of each window, and warmer indoor air exits through the upper half of each window. This exchange of air is a necessary consequence of the principle of mass conservation for an incompressible fluid.

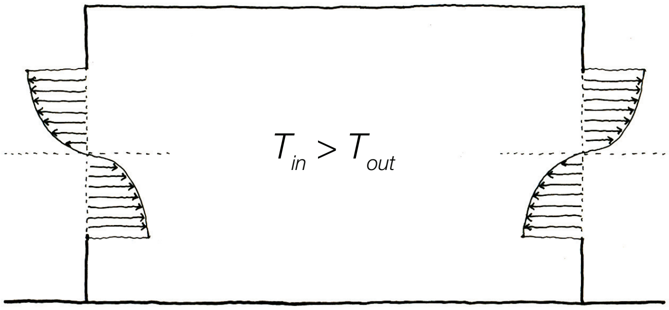

Figure 1-1: Airflow paths and velocity profiles for bidirectional buoyancy-driven flow in the absence of wind forces.

1.1.3 Turbulent fluctuations

The turbulence of the approaching wind and the unsteady character of separated flows cause surface pressures to fluctuate [1]. Any instantaneous pressure $p(t)$ can then be expressed as the sum of the mean, time-averaged value $\overline{p}$ and the essentially random fluctuating component $p'(t)$, and hence any instantaneous pressure difference $\Delta p(t)$ can also be expressed as the sum of the two [10],

$$\Delta p(t) = \Delta\overline{p} + \Delta p'(t) \tag{1.2}$$

The influence of the time-averaged component on ventilation has been discussed above. Since the fluctuating component can either instantaneously increase or decrease mean ventilation rates, mean values are a good estimate for computing ventilation rates, especially since thermal comfort is typically assessed over a period of time. Hence, the effects of turbulent fluctuations on ventilation will not be covered in the present study.

1.2 Difficulties associated with natural ventilation studies in urban areas

For a building situated in an urban area, the driving force due to wind and buoyancy, and consequently the potential for natural ventilation, is significantly altered by the surrounding environment. Figure 1-2 schematically depicts the questions that inevitably arise when the building under consideration for natural ventilation is now sited in an urban context.

For a building located in an isolated or more open area, the magnitudes of the driving forces due to wind and buoyancy can be determined in a fairly straightforward manner. Pressure coefficients for the facades of isolated buildings are well documented; a common source for building scientists is [1]. Wind speeds can easily be obtained from meteorological data, either directly at the measurement height

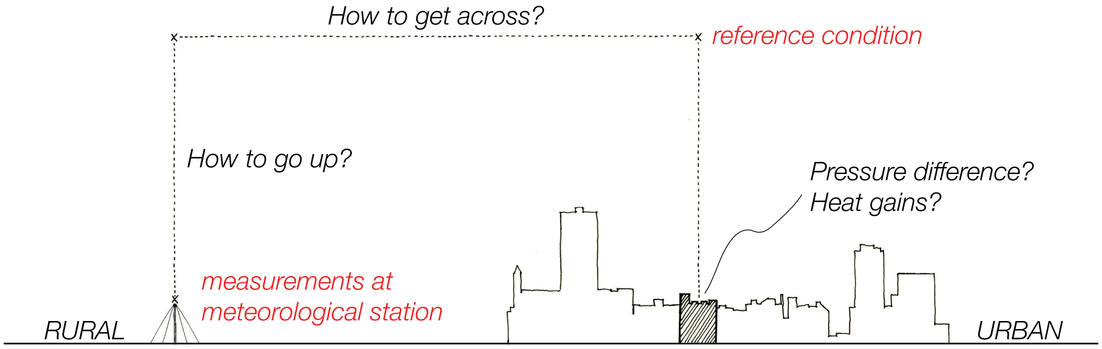

Figure 1-2: Building natural ventilation in an urban context.

of ten meters or at a different height by applying velocity profile laws such as the power law. Since meteorological stations are generally located in open areas, the environmental conditions for the building of interest and the environmental conditions for the available wind speed data align, and no additional work needs to be done in terms of matching the reference location. The same applies to the outdoor temperature value that is needed for calculating buoyancy-driven flows. Building thermal loads are another necessary input for determining the pressure difference generated by buoyancy, but since the building is isolated, these can be approximated from a simple solar analysis and knowledge of the internal heat gain values.

Once the building is placed in an urban area, however, estimating these values is no longer as straightforward. The surface pressures, since they are a function of the environmental surroundings, will certainly change and pressure coefficients for buildings as a function of urban geometry are not as readily available. Furthermore, obtaining wind speeds also becomes a more difficult task since we would expect the wind speeds measured at the meteorological station to be quite different from those in the urban area. Both outdoor temperature and building thermal loads will be affected by the urban surroundings as well. The urban heat island effect results in an increase in air temperatures for urban areas [23]. Surrounding buildings tend to offer increased shading from solar radiation, and this affects the building heat gains and ultimately both the amount of cooling required as well as the potential for buoyancy-driven flow. From this discussion, it is clear that assessing natural ventilation in an urban context introduces difficulties and complexities that deserve further study. The next section summarizes the current state of the research on this topic.

1.3 Literature survey

1.3.1 Classification of flow regimes for arrays of buildings

The flow over large arrays of identical buildings can be grouped into three types of flow regimes that have a functional dependence on the group spacing. This classification was first suggested by Morris [22] for a two-dimensional case, confirmed for three-dimensional roughness elements by Soliman and Lee [27] and Hussain and Lee [20], and further disseminated by Oke [23] in the context of urban planning and street design. The distinguishing characteristics of each flow regime are shown in Figure 1-3. For buildings that are spaced widely apart, where the spacing distance is at least ten times the building height, there will be relatively little interaction between the individual flow fields. The flow field around each building is similar to that of an isolated building. As the spacing distance is decreased, the wakes get disturbed and this isolated roughness flow becomes a wake interference flow. The recirculation zones change in size and shape and secondary flows appear between the buildings.

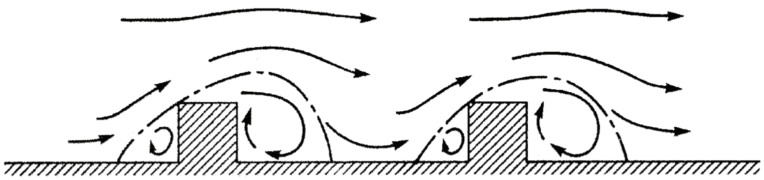

(a) Isolated roughness flow

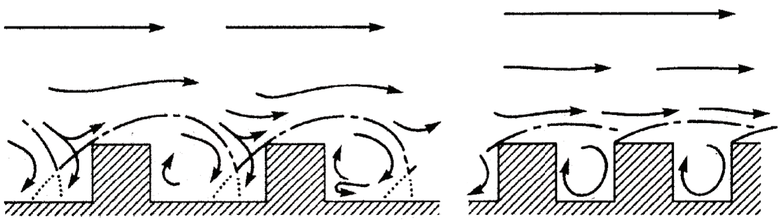

(b) Wake interference flow

(c) Skimming flow

Figure 1-3: Flow regimes associated with airflow over buildings arrays [23].

With further decrease in spacing, the flow transitions to a skimming flow and a stable circulatory vortex forms in the space between the buildings. In this regime, the main flow does not enter this space but skims over the top of the array [19, 20, 23].

The classification of flow regimes offers a basic overview of how the flow in an urban area might change as the building density is increased. One would expect that the changes in flow described here would also affect the surface pressures that drive the natural ventilation. Both physical and numerical experiments have been conducted that directly study the impact of the flow changes in urban areas on pressure differences and natural ventilation potential. These will be discussed in subsequent sections.

1.3.2 Full-scale experimental investigations of natural ventilation in urban canyons

As part of the European Projects *UrbVent* and *ResHyVent*, researchers at the University of Athens performed field study experiments during the summers of 2001 and 2002 in seven pedestrian deep street canyons in Athens, Greece [25]. A canyon is a relatively narrow street with buildings that line up continuously along both sides. Deep canyons are characterized by canyon aspect ratios $\frac{H}{W} \geq 2$, where the canyon aspect ratio is defined as the height of the building H divided by the width of the street W [12]. Experiments took place over three consecutive days and for 12 or 24 hours per day. For each canyon, a mobile meteorological station was used to take measurements of air velocities and temperatures both inside the canyon at several heights as well as outside the canyon [25].

From this extensive experimental campaign, a large set of publications emerged. Of particular relevance is a study by Georgakis and Santamouris that, in addition to an analysis of the experimental data discussed above, also presented results of airflow and temperature measurements inside a naturally ventilated apartment that was located in one of the canyons, with the intention of studying the impact of the urban environment on the efficiency of natural ventilation techniques. Both single-sided and cross-ventilated experiments were carried out, and airflow rates were obtained using tracer gas techniques. In order to evaluate the impact of the decreased wind speed in canyons, the measured airflow results were compared to results from two simulation cases: the first case used wind speed and temperature values inside the canyon as inputs, while the second case relied on undisturbed data above the canyon for inputs [12]. The simulation software utilized was the *AIOLOS* software [2], a validated airflow network model that also includes the subroutine *CPCALC+* [17] to calculate pressure coefficients for different values of urban geometrical parameters. Based on a comparison of their results, the authors concluded that the potential for natural ventilation in urban canyons is seriously reduced, a reduction of about 82 and 68% in airflow rate for the single-sided and cross-ventilation configuration, respectively [12]. These conclusions align with those obtained from another study conducted by Geros and Santamouris focused on night ventilation [15].

From an analysis of the experimental data, Georgakis and Santamouris developed a model for the calculation of wind speed and direction at any location inside an urban canyon. For high ambient wind speeds, a coupling exists between the undisturbed flow above the canyon and the flow inside the canyon, and the model selects the appropriate algorithm for flow along the canyon, oblique to the canyon, or perpendicular to the canyon [13]. For ambient wind speeds below a certain threshold (< 4m/s), this coupling is lost, and airflow in urban canyons is characterized by a high scatter and important fluctuation. For these cases, simplified data-driven methods were derived from a graphical analysis of the experimental measurements discussed above. The model has been validated against the experimental data and was shown to exhibit good agreement [25]. This methodology for estimating wind speed has also been coupled to another model capable of assessing the indoor-outdoor transfer of noise and pollution [14, 16]. While the overall approach is quite comprehensive, it is not entirely clear what purpose the wind speeds at locations inside the canyon serve when used in conjunction with surface wind pressure coefficients, particularly if those coefficients are referenced to a height outside the canyon. This is discussed further in Chapters 4 and 5.

1.3.3 Small-scale salt bath modeling of natural ventilation in urban canyons

Syrios and Hunt studied the combined wind- and buoyancy-driven flow of a building in an urban canyon using small-scale salt bath modeling. They considered a naturally ventilated enclosure that has high- and low-level vents and a plume of warm air rising from a heat source at floor level inside the building. The experimental set up consisted of a clear Perspex box with high-level and low-level rectangular vents (total opening area fixed at approximately 1% of the total floor area) and urban canyons formed upstream and downstream by positioning two additional plastic boxes, of identical dimensions to the Perspex box, parallel to and on either side of the Perspex box. The entire model was suspended in a recirculating flume and a pump-driven horizontal turbulent flow along the flume simulated a wind normal to the canyon axis. No attempt was made to simulate the atmospheric boundary layer. The release of salt solution through a nozzle at constant buoyancy flux simulated the convection from a localized heat source at floor level. Two openings configurations were considered. For Case 1, the high-level vents are located on the windward facade and the low-level vents are located on the leeward facade; for Case 2, vice versa. For each case, the effect of varying the wind speed for a square canyon ($\frac{H}{W} = 1$) and the effect of varying the canyon aspect ratio ($\frac{1}{5} < \frac{H}{W} < 2$) was investigated. Observed steady ventilation flows and internal stratifications were documented for the range of wind speeds and canyon widths [30].

From their observations, the authors determined that placing a building within the confines of an urban canyon reversed the effect of wind on thermally-driven ventilation. That is, for Case 1, the wind opposed the buoyancy-driven flow in the absence of canyons, which is the expected result for this type of opening configuration. However, introduction of surrounding canyons resulted in assisting winds as observed by shadowgraph images of the steady internal stratification. For Case 2, an assisting wind condition was observed in the absence of canyons but opposing wind conditions in the presence of surrounding canyons [30]. The authors explain this reversal effect by referencing dye injection experiments that showed flow patterns in the upstream and downstream canyons responsible for the surface pressures on the leeward facade exceeding that of the windward facade of the ventilated building [29].

However, the present investigation only considers a setup with three rows of buildings, that is two canyons in total, and it seems that it cannot be immediately deduced that these conclusions would still be valid for a larger group of canyons that is more representative of a real urban area.

1.3.4 CFD simulations of natural ventilation behavior for arrays of buildings

Cheung and Liu investigated the effect of building interference on the natural ventilation of high-rise buildings using the computational fluid dynamics technique based on the Reynolds-averaged Navier-Stokes equations. The sensitivity of ventilation rate to wind direction, building separation, and array layout was studied. They determined that a building separation distance of about five times the building width is sufficient for minimizing the unfavorable interference between buildings. They also observed that arrays laid out in an irregular or staggered fashion can significantly improve natural ventilation performance, and in that case the ideal separation distance could be reduced to three times the building width [6].

1.4 Motivation and approach for the research

The motivation behind our research was to obtain a better understanding of what constitutes the problem of natural ventilation building design in urban areas. In particular, the objective was to identify the dominant physics, variables, and parameters, to utilize this information to simplify the problem, and to still deliver practical and meaningful information to designers that could help guide decision-making in the beginning stages of the design process.

When a designer is considering natural ventilation for a building, he or she will generally conduct an analysis to assess the viability of this strategy. This analysis typically consists of a series of steps that begins with estimating the surface pressures on the building's facades and concludes with final predictions of indoor temperature and thermal comfort. The approach of the present work was to carefully retrace each of these steps as they are applied to a simplified residential geometry, to determine some of the main difficulties that would likely be encountered during this process of analysis, and to develop appropriate recommendations to resolve these.

For this reason, the present investigation does not focus solely on wind speeds or solely on pressure coefficients, but rather on how these and other elements interact to form the landscape of analysis that a designer would need to navigate. This approach would provide a designer unfamiliar with the problem of natural ventilation building design in urban areas the most valuable information and the necessary guidance to conduct an early-design-stage analysis. While noise and pollution are clearly important considerations in assessing whether a particular building is suitable for natural ventilation, our focus here mainly concerns the estimation of airflow potential and hence these criteria are beyond the scope of this study.

The investigation is divided into four main parts that comprise the remaining four chapters of this work:

I Developing the natural ventilation physics for a simplified geometry

II Obtaining surface wind pressure coefficients as a function of urban morphology

III Estimating suitable reference velocities

IV Design implications and recommendations

The final product of this work consists of simple-to-use graphical methods that were naturally obtained from retracing the steps of natural ventilation analysis discussed above. These graphical methods can be used to estimate airflow rates and indoor-outdoor temperature differences for several opening geometries and to assist a designer in visually understanding the physics of natural ventilation in progressively more dense urban layouts. If one is interested in assessing the effect of other opening geometries or alternate inputs in general, a script that runs in the numerical computing environment *MATLAB* and that can generate additional figures is provided in the Appendix. It is important to note that these graphical methods form a simple approach to guide decision-making during the initial stages of the design process and hence are not intended as a substitute for the more detailed experiments or simulations of later design stages.

Chapter 2

Natural ventilation physics for a simple geometry

2.1 Geometry

We considered the main cross-ventilated living space of a typical apartment unit for our geometry. This space has minimal interior partitions and is thus modeled as one large open room with two windows of equal area placed on opposite walls at equal heights above the floor. The floor area is 40m^2 (approximately 450ft^2), with actual dimensions shown in Figure 2-1. Applying a typical window-to-wall-ratio for residential buildings of 0.25 gives a glazing area of 3.4m^2 on each facade. The glazing area is assumed to be equal to the operable area for ventilation. Two opening heights are considered, 1.5m and 0.75m, as shown in Figure 2-1. For this geometry, natural ventilation can be driven by both wind and buoyancy forces. In the case of buoyancy, the flow pattern would be that of a bidirectional flow as discussed and sketched in Section 1.1.2. The following section presents a derivation of the indoor temperature solution for combined wind and buoyancy forcing.

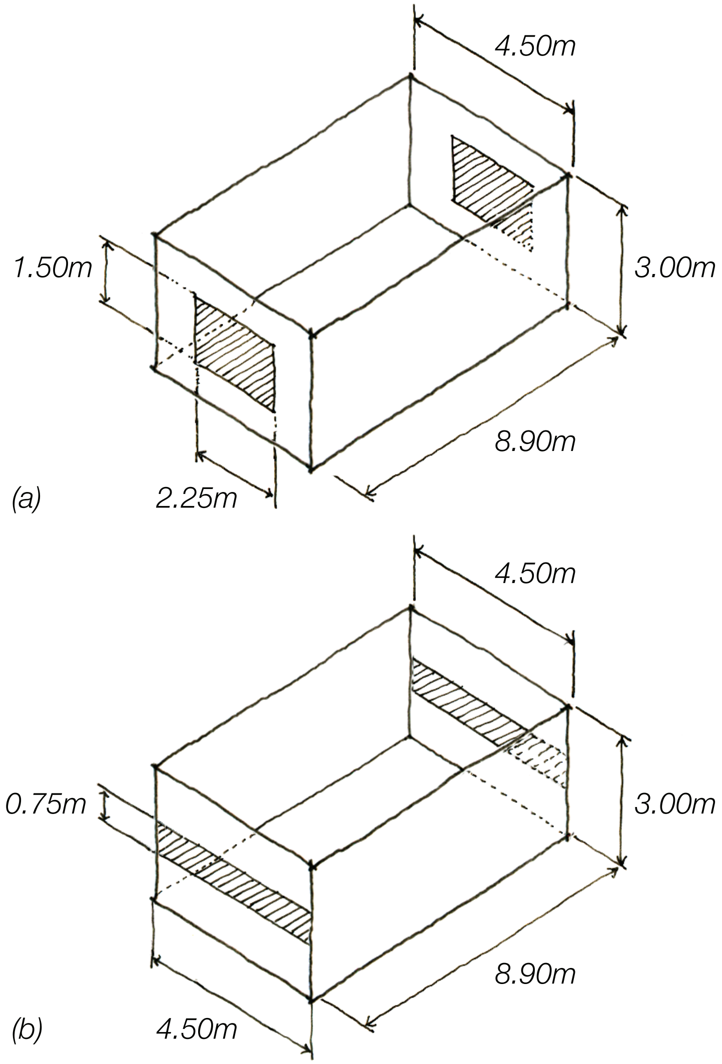

Figure 2-1: Geometry: a) $h = 1.5$m, b) $h = 0.75$m.

2.2 Analytical solution to combined wind and buoyancy problem

Bernoulli's equation, a statement of conservation of energy per unit volume along a streamline, can be applied to determine the theoretical velocity profile for an opening with bidirectional flow in the *presence* of wind forces. This velocity profile can then be integrated along the height of the opening to obtain the flow rate per unit width, and subsequently by enforcing conservation of energy on the room control volume, one can then obtain the desired expression for the indoor-outdoor temperature difference.

We begin with Etheridge and Sandberg's application of the Bernoulli equation to a small opening or orifice followed by their extension of the same method to a larger opening with bidirectional flow in the *absence* of wind forces [10]. The orifice connects two large stationary reservoirs of different densities, as shown in Figure 2-2. The densities in the two reservoirs are ρ_H and ρ_C, the height is measured from the floor and is denoted by z, and the base pressures at the floor are $p_H(0)$ and $p_C(0)$. In this chapter, pressure refers to the mean, time-averaged value of the instantaneous pressure. Using the Bernoulli equation, we can write the conservation of energy per

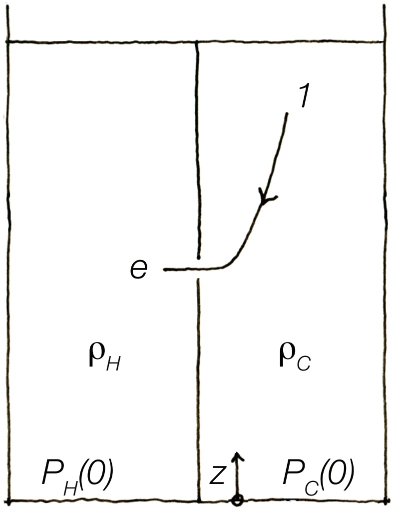

Figure 2-2: Flow through a small orifice connecting reservoirs of different densities.

unit volume for the streamline shown in the figure above,

$$p_1 + \rho_C g z_1 = p_e + \rho_C g z + \rho_C \frac{u_e(z)^2}{2} \tag{2.1}$$

Since the reservoirs are large, far from the opening it can be assumed that the velocities are zero. The pressure at point 1, p_1, can then be written as

$$p_1 = p_C(0) - \rho_C g z_1 \tag{2.2}$$

If the jet streamlines are assumed to be horizontal and parallel, the pressure of the jet exiting the orifice is equal to the pressure at the same height in the receiving reservoir,

$$p_e = p_H(0) - \rho_H g z \tag{2.3}$$

Substituting Equations 2.2 and 2.3 into Equation 2.1 yields an expression for the velocity profile of a jet exiting an orifice from a reservoir of high density to a reservoir of low density,

$$\rho_C \frac{u_e(z)^2}{2} = p_C(0) - p_H(0) - (\rho_C - \rho_H) g z \tag{2.4}$$

To extend this orifice model to larger openings, such as windows and doors, Etheridge and Sandberg applied the same assumptions used to derive Equations 2.2 and 2.3, that is zero velocity far from the opening and horizontal, parallel streamlines at the opening, to opening heights that are not small relative to the wall height [10]. The general validity of these assumptions is discussed at the end of this chapter. The problem sketch for a large opening with bidirectional flow and the corresponding velocity profile solution are shown in Figure 2-3. The variables are the same as in the orifice case with the addition of temperatures T_H and T_C representing the temperatures in the warm and cool room, respectively, the opening height h, and the height of the neutral plane h_n that denotes the height at which the pressures in both rooms are assumed to be equal and therefore the velocity is also zero. Equation 2.4 above then applies to a streamline from the cool room to the warm room, and an analogous

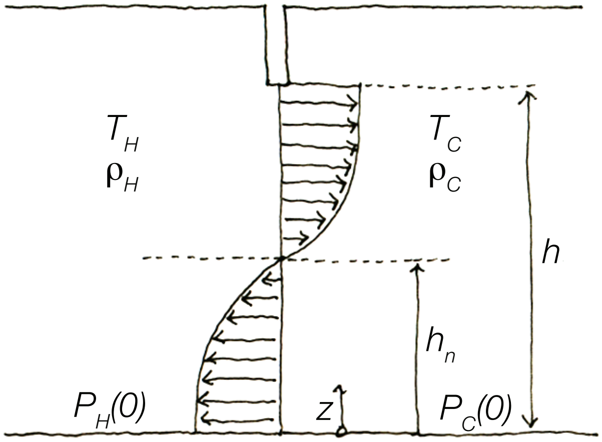

Figure 2-3: Flow through a large opening in the *absence* of wind forces.

statement can be written for a streamline from the warm room to the cool room,

$$\rho_H \frac{u_e(z)^2}{2} = p_H(0) - p_C(0) + (\rho_C - \rho_H)gz \tag{2.5}$$

The base pressure difference $p_H(0) - p_C(0)$ is unknown but can be expressed in terms of the neutral height since $u_e(h_n) = 0$,

$$p_C(0) - p_H(0) = g\Delta\rho h_n \tag{2.6}$$

where $\Delta\rho$ is $\rho_C - \rho_H$. The same can be done for the base pressure difference of the stream flowing from the cool to the warm room. Substituting both expressions into Equations 2.5 and 2.4, respectively, and solving for the velocities, we obtain

$$u_{CH}(z) = (2g'_H(z - h_n))^{\frac{1}{2}} \tag{2.7}$$

$$u_{HC}(z) = (2g'_C(h_n - z))^{\frac{1}{2}} \tag{2.8}$$

where the reduced gravity terms are defined as

$$g'_C = g\left(\frac{\rho_C - \rho_H}{\rho_H}\right) \tag{2.9}$$

$$g'_H = g\left(\frac{\rho_C - \rho_H}{\rho_C}\right) \tag{2.10}$$

These velocities can be integrated along the height of the opening to give expressions for the total volumetric flow rate per unit width through a large opening with bidirectional flow, where any contraction of the streamlines is neglected:

$$q_{HC} = \int_0^{h_n} u(z)dz = \frac{1}{3}{g'_c}^{\frac{1}{2}} 2^{\frac{3}{2}} {h_n}^{\frac{3}{2}} \tag{2.11}$$

$$q_{CH} = \int_{h_n}^{h} u(z)dz = \frac{1}{3}{g'_h}^{\frac{1}{2}} 2^{\frac{3}{2}} (h - h_n)^{\frac{3}{2}} \tag{2.12}$$

q_{HC} denotes the volumetric flow rate per unit width entering the warm room and q_{CH} denotes the volumetric flow rate per unit width leaving the warm room. In the absence of wind forces, q_{HC} and q_{CH} are equal by mass conservation, and h_n is located approximately mid-height of the opening.

To account for wind forces, we can extend Etheridge and Sandberg's derivation by adding a wind pressure component. We begin with a qualitative understanding of how the velocity profile changes in the presence of an approaching wind normal to the face of the opening, as shown in Figure 2-4. We see that when wind forces are introduced, the neutral plane shifts and is no longer located at mid-height of the opening. On the windward side, the neutral plane shifts upwards, and on the leeward side, the neutral plane shifts downwards. We thus have two different neutral planes, one for each opening, and we denote the heights of these neutral planes $h_{n,w}$ and $h_{n,l}$ for the windward and leeward opening, respectively. As increasing wind pressure is applied, the neutral plane continues to shift upwards (or downwards for the leeward facade) until the flow through the openings eventually becomes unidirectional (Figure 2-4c). For sufficiently large wind pressures, there are no neutral planes, and the flow

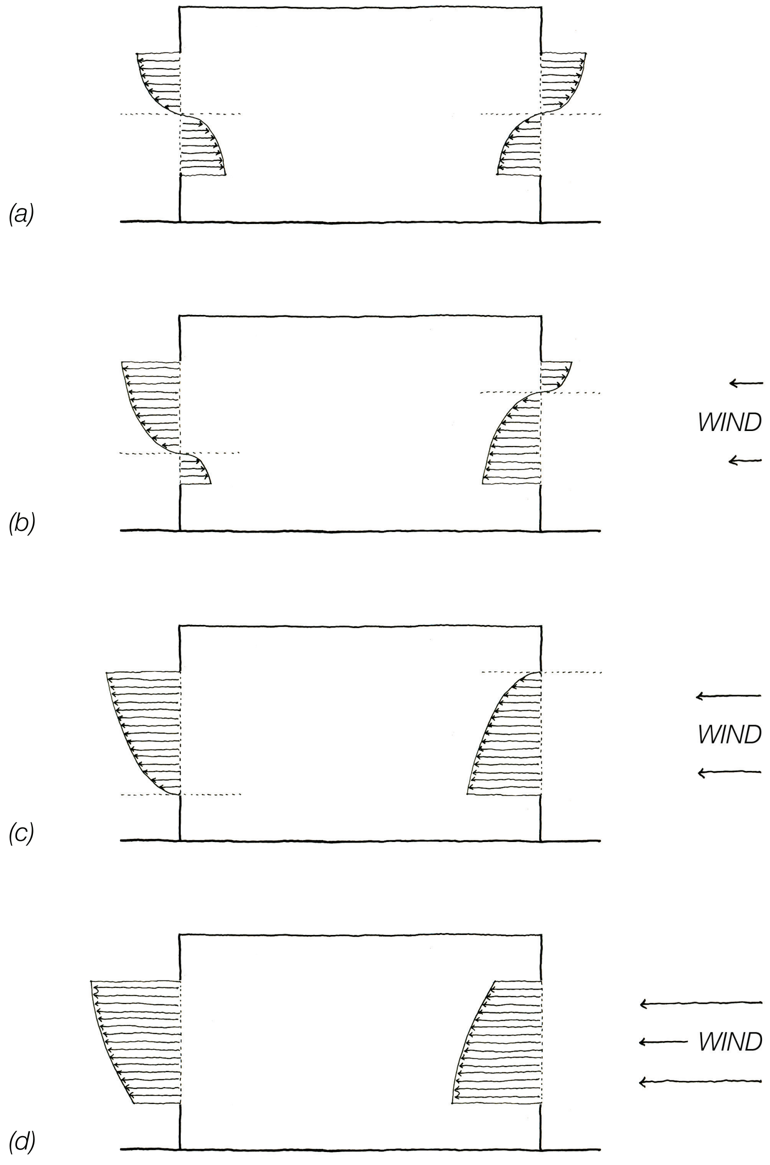

Figure 2-4: Development of velocity profile with increasing wind pressure.

is basically entirely wind-driven with a negligible buoyancy component (Figure 2-4d). Assuming density differences are small, all figures depict windward and leeward velocity profiles that are 180° rotations of each other and hence clearly show that mass must be conserved in all cases.

The key to determining the flow rate through an opening in the combined wind and buoyancy problem is to obtain expressions for the two neutral heights. Focusing on the geometry sketched in Figure 2-1, the cold room now represents the exterior environment and the warm room the interior space, as shown in Figure 2-5. A streamline connects point 1, located at the surface on the exterior side, with point e, located slightly downstream of the opening where the streamlines are assumed to be parallel. In wind tunnel experiments, surface pressure coefficients are typically obtained from models with solid surfaces, that is the actual openings are not present. For this reason, the velocity at the surface at point 1 would be zero and the pressure at that point is the stagnation pressure that makes use of the pressure coefficient (Equation 2.14). The Bernoulli equation applied to the streamline from point 1 to point e is then

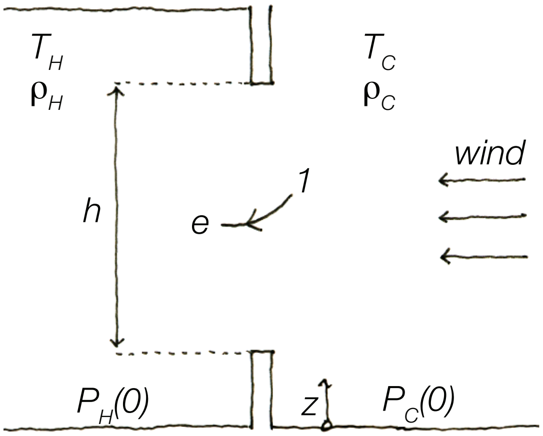

Figure 2-5: Flow through a large opening in the *presence* of wind forces.

$$p_1 + \rho_C g z_1 = p_e + \rho_C g z + \rho_C \frac{u_e(z)^2}{2} \tag{2.13}$$

where the pressures p_1 and p_e can be rewritten as

$$p_1 = p_C(0) - \rho_C g z_1 + C_p \frac{1}{2} \rho_C u^2 \tag{2.14}$$

$$p_e = p_H(0) - \rho_H g z \tag{2.15}$$

Comparing this expression for p_1 with the one derived for the orifice model (Equation 2.2), p_1 in this case accounts for the additional wind pressure component. C_p is the surface wind pressure coefficient and u is the wind speed taken at a point that matches the reference condition of the pressure coefficient. We can substitute the pressure expressions into Equation 2.13 to obtain

$$\frac{1}{2} \rho_C u_e(z)^2 = p_C(0) - p_H(0) - (\rho_C - \rho_H) g z + C_p \frac{1}{2} \rho_C u^2 \tag{2.16}$$

where the quantity on the right hand side represents the pressure difference across the opening that drives the flow. As before, if we assume zero velocity at the neutral height, $u_e(h_n) = 0$, then

$$h_n = \frac{p_C(0) - p_H(0) + C_p \frac{1}{2} \rho_C u^2}{g(\rho_C - \rho_H)} \tag{2.17}$$

It follows that the neutral height is a function of the surface wind pressure when wind forces are present. When Equations 2.16 and 2.17 are combined to eliminate the base pressure difference, the surface wind pressure term also cancels and the result is identical to the set of equations derived for the purely buoyancy case (Equations 2.7-2.10). Adding wind forcing does not change the overall velocity profiles, but only shifts them up or down resulting in neutral planes that are no longer located at mid-height of the opening. Hence, Equations 2.11 and 2.12 for calculating the volumetric flow rate per unit width through an opening are also valid in the case of buoyancy-driven bidirectional flow when wind forces are present.

We can write Equation 2.17 for both openings of the geometry we are considering by setting $u_e(h_{n,w}) = 0$ and $u_e(h_{n,l}) = 0$ and solving for the two neutral heights:

$$h_{n,w} = \frac{p_C(0) - p_H(0) + C_{p,w}\frac{1}{2}\rho_C u^2}{g(\rho_C - \rho_H)} \tag{2.18}$$

$$h_{n,l} = \frac{p_C(0) - p_H(0) + C_{p,l}\frac{1}{2}\rho_C u^2}{g(\rho_C - \rho_H)} \tag{2.19}$$

where the surface pressure on the windward side is $C_{p,w}\frac{1}{2}\rho_c u^2$ and the surface pressure on the leeward side is $C_{p,l}\frac{1}{2}\rho_c u^2$. The two equations can be combined to eliminate the base pressure difference $p_C(0) - p_H(0)$ to yield a single relation for the two neutral heights,

$$h_{n,l} = h_{n,w} - \frac{\frac{1}{2}\rho_c u^2 (C_{p,w} - C_{p,l})}{g(\rho_C - \rho_H)} \tag{2.20}$$

This equation makes physical sense. If the wind speed u or the wind pressure coefficient difference $C_{p,w} - C_{p,l}$ is increased, the difference between the neutral heights also increases, and the flow approaches a wind-dominated solution (Figure 2-4d). When either u is zero or $C_{p,w} - C_{p,l}$ is zero in the case of wind parallel to the facades, the difference $h_{n,l} - h_{n,w}$ is also zero, and one obtains a purely buoyancy-driven flow with both neutral heights located at mid-height of the opening (Figure 2-4a).

To solve for the neutral heights, we need another constraint to the system. We know from symmetry and mass conservation that

$$h_{n,l} + h_{n,w} = h \tag{2.21}$$

Combining these two equations yields

$$h_{n,w} = \frac{1}{2}\left[h + \frac{\frac{1}{2}\rho_c u^2 (C_{p,w} - C_{p,l})}{g(\rho_C - \rho_H)}\right] \tag{2.22}$$

Furthermore, assuming compressibility effects are small, that is density variations are only due to temperature variations and not pressure variations, then the changes in density can be described by the coefficient of thermal expansion of a gas β,

$$\beta \equiv \frac{1}{\rho}\frac{\partial \rho}{\partial T} \tag{2.23}$$

and for an ideal gas,

$$\beta = \frac{1}{T} \tag{2.24}$$

which yields,

$$\frac{\Delta T}{T} \approx \frac{\Delta \rho}{\rho} \tag{2.25}$$

Consequently, the densities in Equation 2.22 can be approximated as temperatures, that is

$$h_{n,w} = \frac{1}{2}\left[h + \frac{T_{in}}{g(T_{in} - T_{out})}\tfrac{1}{2}u^2(C_{p,w} - C_{p,l})\right] \tag{2.26}$$

It follows that $h_{n,w}$ is a linear function of the wind pressure coefficient difference. If the indoor temperature is known, one can analytically solve for both neutral heights and use Equation 2.11 to calculate the total volumetric flow rate through the room:

$$\begin{aligned} Q_{total} &= \frac{A}{h}(q_{HC,w}) + \frac{A}{h}(q_{HC,l}) \\ q_{HC,w} &= \frac{1}{3}{g'_c}^{\frac{1}{2}}2^{\frac{3}{2}}{h_{n,w}}^{\frac{3}{2}} \\ q_{HC,l} &= \frac{1}{3}{g'_c}^{\frac{1}{2}}2^{\frac{3}{2}}{h_{n,l}}^{\frac{3}{2}} \end{aligned} \tag{2.27}$$

where $q_{HC,w}$ is the volumetric flow rate per unit width entering the room through the windward opening and $q_{HC,l}$ is the volumetric flow rate per unit width entering the room through the leeward opening (see Figure 2-4a and 2-4b), and A and h are the opening area and height, respectively. Alternately, one could have used Equation 2.12 to calculate the outflow through each opening and taken their sum them to obtain the same total flow rate, since the inflow must be balanced by the outflow.

The process is straightforward if the indoor temperature is known a priori. Most of the time, however, the indoor temperature is unknown, since in natural ventilation studies the motivation for calculating flow rates in the first place is to determine how much the ventilation can lower the indoor temperature. To derive a second equation relating flow rate to indoor temperature, we apply a simplified form of conservation of energy to the room:

$$\frac{dE}{dt} = \dot{E}_{gen} + \dot{E}_{conv} + \dot{E}_{cond} \tag{2.28}$$

$\frac{dE}{dt}$ is the rate of change of energy in the room, $\dot{E}_{gen}$ is the rate of energy generated in the room, $\dot{E}_{conv}$ is the rate of energy entering the room by convection, and $\dot{E}_{cond}$ is the rate of energy entering the room by conduction. If we assume the room is well-insulated, then $\dot{E}_{cond}$ is negligible. Additionally, if we also assume that the heat transfer due to infiltration of outside air is much smaller than that due to ventilation, then at steady state, the heat gains are balanced by the heat losses due to ventilation:

$$\dot{E}_{gen} = \rho c_p Q_{total}(T_{in} - T_{out}) \tag{2.29}$$

where $\dot{E}_{gen}$ is the sensible portion of the room heat gains, usually a combination of internal gains and solar gains.

We now have two equations relating our two unknown variables, indoor temperature and flow rate. Substituting Equation 2.27 into Equation 2.29, and rewriting the densities as temperatures and h_{nl} in terms of h_{nw} (Equations 2.25 and 2.21, respectively), gives

$$\dot{E}_{gen} = \rho c_p \left[\frac{1}{3}\left(\frac{A}{h}\right) 2^{\frac{3}{2}} g^{\frac{1}{2}} \left(\frac{T_{in} - T_{out}}{T_{in}}\right)^{\frac{1}{2}} \left(h_{n,w}^{\frac{3}{2}} + (h - h_{n,w})^{\frac{3}{2}}\right)\right] (T_{in} - T_{out}) \tag{2.30}$$

As the air moves through the opening, streamline contraction and energy losses from flow separation result in a reduction in airflow rate that the Bernoulli equation does not account for. In natural ventilation studies, the usual remedy is to multiply the flow rate by a discharge coefficient C_d that effectively reduces the heat transfer due to the ventilation:

$$\dot{E}_{gen} = C_d \rho c_p \left[\frac{1}{3}\left(\frac{A}{h}\right) 2^{\frac{3}{2}} g^{\frac{1}{2}} \left(\frac{T_{in} - T_{out}}{T_{in}}\right)^{\frac{1}{2}} \left(h_{n,w}^{\frac{3}{2}} + (h - h_{n,w})^{\frac{3}{2}}\right)\right] (T_{in} - T_{out}) \tag{2.31}$$

for $0 \leq h_{n,w}, h_{n,l} \leq h$

where $h_{n,w}$ and $h_{n,l}$ are computed using Equations 2.21 and 2.26. This expression can be solved numerically for the indoor temperature when both neutral heights are less than the opening height, that is, $0 \leq h_{n,w}, h_{n,l} \leq h$. The moment $h_{n,w} > h$ (and hence, by Equation 2.21, $h_{n,l} < 0$), the term $(h - h_{n,w})^{\frac{3}{2}}$ produces complex values. This can be explained by looking at Equations 2.11 and 2.12, where we see that the bounds of integration for q_{HC} and q_{CH} assume that the neutral heights are always less than the opening height. For cases with no bidirectional flow, that is $h_{n,w} > h$ ($h_{n,l} < 0$), the velocity profile needs to be integrated over the entire opening height,

$$q_{HC} = \int_{0}^{h} u(z)dz = -\frac{1}{3} g_c'^{\frac{1}{2}} 2^{\frac{3}{2}} \left[(h_n - h)^{\frac{3}{2}} - h_n^{\frac{3}{2}} \right] \tag{2.32}$$

for $h_{n,w}, h_{n,l} \geq h$

The total volumetric flow rate is now simply (see Figure 2-4c and 2-4d),

$$Q_{total} = \frac{A}{h}(q_{HC,w}) \tag{2.33}$$

since the only inflow is through the windward opening and there is no inflow through the leeward opening. Combining Equations 2.32 and 2.33 with Equation 2.29, and making the same modifications as for Equation 2.30 above, we obtain a second expression that can be solved numerically for the indoor temperature, this one valid for $h_{n,w}, h_{n,l} > h$,

$$\dot{E}_{gen} = C_d \rho c_p \left[-\frac{1}{3} \left(\frac{A}{h} \right) 2^{\frac{3}{2}} g^{\frac{1}{2}} \left(\frac{T_{in} - T_{out}}{T_{in}} \right)^{\frac{1}{2}} \left((h_{n,w} - h)^{\frac{3}{2}} - h_{n,w}^{\frac{3}{2}} \right) \right] (T_{in} - T_{out}) \tag{2.34}$$

for $h_{n,w}, h_{n,l} > h$

If the interest is in airflow rates, the total volumetric flow rates can be determined from the indoor temperatures using

$$Q_{total} = \frac{1}{3}\left(\frac{A}{h}\right)2^{\frac{3}{2}}g^{\frac{1}{2}}\left(\frac{T_{in}-T_{out}}{T_{in}}\right)^{\frac{1}{2}}\left(h_{n,w}^{\frac{3}{2}} + (h-h_{n,w})^{\frac{3}{2}}\right) \tag{2.35}$$

for $0 \leq h_{n,w}, h_{n,l} \leq h$

$$Q_{total} = -\frac{1}{3}\left(\frac{A}{h}\right)2^{\frac{3}{2}}g^{\frac{1}{2}}\left(\frac{T_{in}-T_{out}}{T_{in}}\right)^{\frac{1}{2}}\left((h_{n,w}-h)^{\frac{3}{2}} - h_{n,w}{}^{\frac{3}{2}}\right) \tag{2.36}$$

for $h_{n,w}, h_{n,l} > h$

2.2.1 Graphical representation in terms of indoor-outdoor temperature difference

Equations 2.31 and 2.34 were solved numerically for the indoor temperature values assuming a T_{out} value of 300K. Since the dependence of T_{in} on T_{out} is negligible for T_{out} values typically encountered in natural ventilation (∼10-30°C), we can use this T_{out} value to write the indoor temperature results as indoor-outdoor temperature differences for more general applicability. The resulting values were plotted as a function of wind pressure coefficient difference for three values of room heat gain densities and two values of wind speeds, generating a total of six curves. Both opening heights (see Section 2.1) were considered, as shown in Figure 2-6. From the figures, it follows that as the heat gains are increased, the temperature difference increases as well, and as the wind speed is increased, the temperature difference decreases. These observations align with our physical intuition of the problem. Now, as the wind pressure coefficient difference is decreased, the temperature difference does increase, but only for wind pressure coefficient differences above a certain value. For values smaller than this critical value, the temperature difference levels off and no longer changes with decreasing pressure difference. For the geometry under consideration with an opening height of $h = 1.5$m, Figure 2-6a suggests that the critical value of the wind pressure coefficient difference for a heat gain density of 20W/m^2 and a wind speed of 5m/s is around 10^{-3}. In general, the figures indicate that the critical value is a function of both heat gains and wind speed. Physically, the constant

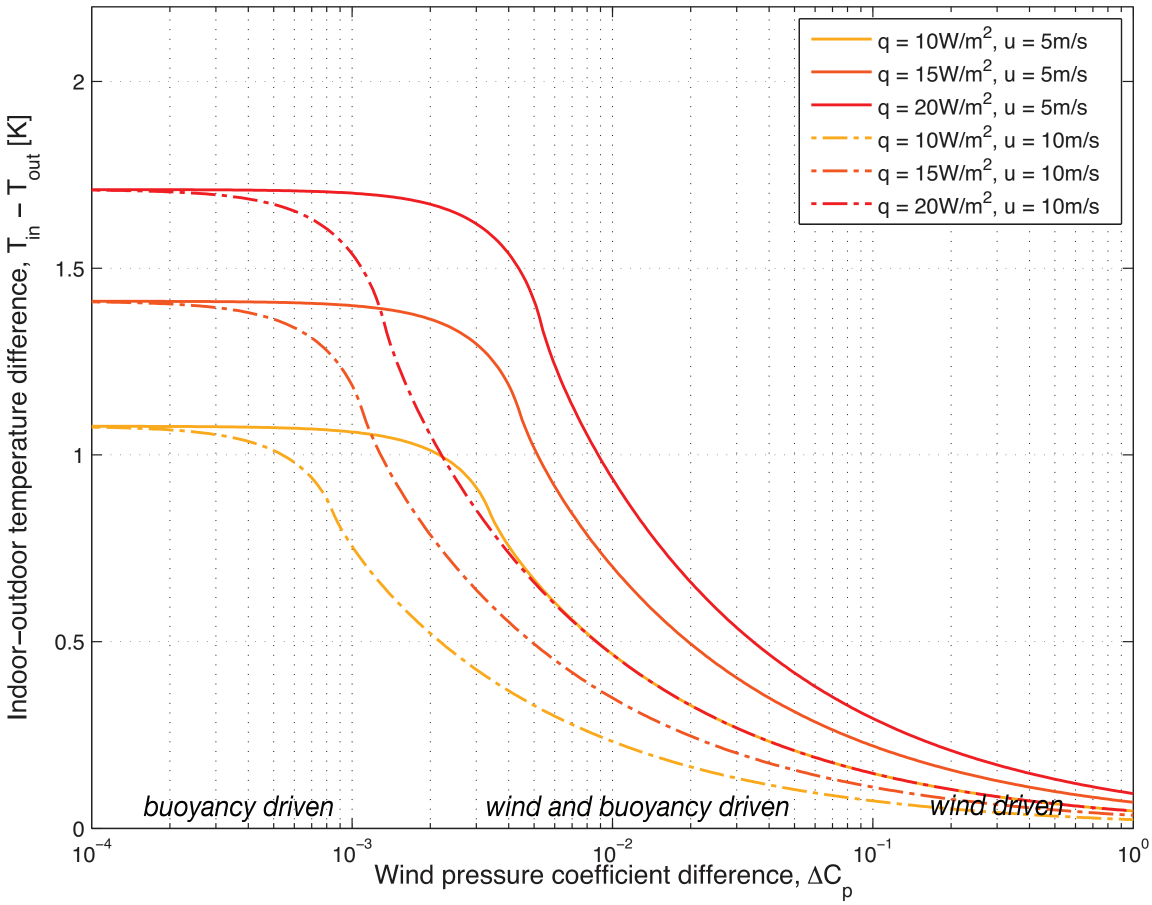

(a) Geometry with opening height h = 1.5m.

Figure 2-6: Indoor-outdoor temperature difference as a function of wind pressure coefficient difference. q is the zone heat gain density and u is the wind speed measured at a location that matches the reference condition of the pressure coefficient.

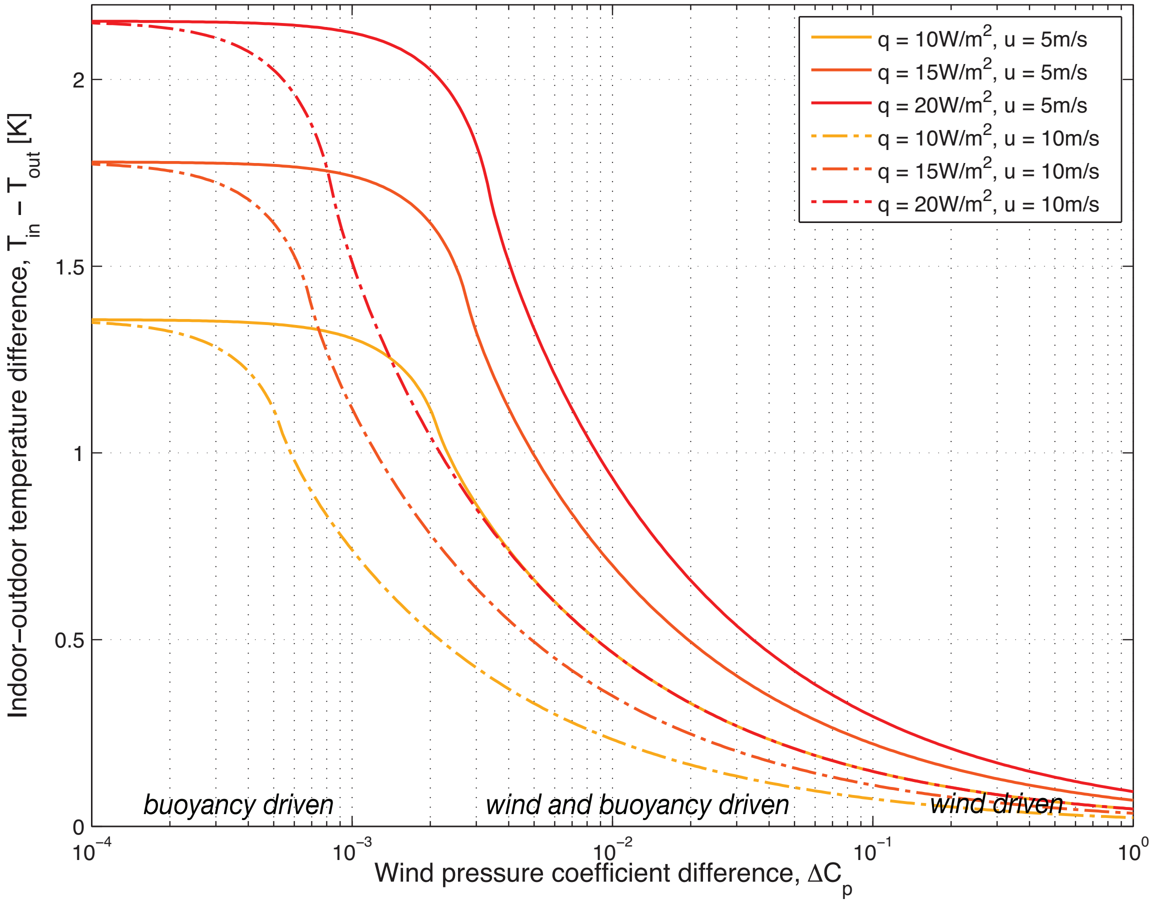

(b) Geometry with opening height h = 0.75m.

Figure 2-6: Indoor-outdoor temperature difference as a function of wind pressure coefficient difference. q is the zone heat gain density and u is the wind speed measured at a location that matches the reference condition of the pressure coefficient.

temperature difference can be understood as follows. At very low wind pressure coefficient differences below the critical value, the driving force due to wind becomes negligible, and the only natural ventilation through the zone will be from a buoyancy-driven bidirectional flow through each opening. Since this flow is independent of the wind pressure coefficient difference, the temperature difference approaches a constant value for a given heat gain density and opening height.

We can therefore recognize three distinct flow regimes from the graphical representation of the numerical solution to Equations 2.31 and 2.34. Looking again at Figure 2-6, at the very far right when wind pressure coefficient differences are of order 1, the flow is dominantly wind-driven, the natural ventilation potential is high, and the indoor temperatures are very close to the outdoor temperatures. At the very far left, the flow is dominantly buoyancy-driven, and the indoor-outdoor temperature difference approaches a constant value; this upper bound can be calculated from knowledge of the heat gains and opening height. In-between, the flow is driven by both wind and buoyancy forces, and while we might expect the prediction of indoor temperatures to be more difficult in this regime, Section 2.2.4 will present and discuss a simplification that is valid in this case. For a given heat gain density, all curves converge to a temperature difference of roughly zero at the far right; at the far left, all curves converge again, but in this case to a temperature difference generated from purely buoyancy-driven forces. In-between, the curves diverge and take on different values that depend on the magnitude of the wind speed.

Figure 2-6 can be used to estimate the indoor temperature for the geometry under consideration if the heat gain density, the outdoor temperature, the wind pressure coefficient difference, and the wind speed at the reference location are known. The heat gain densities used to compute the curves for this figure were obtained from a resistance-capacitance network model that can account for the energy interactions between buildings and their urban environment [4]. Using typical residential values for the glazing ratio and internally generated heat gains, as well as default construction definitions and heat transfer properties, the average daily profile of heat gain density was computed for a typical summer period in Boston. The simulations were run for four different canyon aspect ratios $\frac{H}{W}$ to study the effect of building interactions on zone thermal loads, and the results are summarized in Figure 2-7. q_{sol} is defined as the transmitted solar radiation in W/m^2 of floor area, and q_{sens} is the total sensible heat gain in W/m^2 due to both internal and solar loads. In these definitions, the envelope heat gains and losses are assumed to be negligible. The transmitted solar radiation is modulated by the thermal mass that is part of the default construction definitions. Hence at any point in time, q_{sol} can be greater than q_{sens}, but over a period of a day, the sum of all q_{sol} will be less than the sum of all q_{sens}. From Figure 2-7, we can see that as the canyon aspect ratio is increased, the sensible heat gains decrease for all hours of the day. Since the transmitted solar radiation values also decrease with canyon aspect ratio, one could deduce that as the buildings get closer, the increased shading between buildings reduces the amount of solar radiation entering per zone. To obtain the sensible heat gain densities used in Figure 2-6, the mean of the daily values was calculated for each aspect ratio, and the resulting values were split into three intervals of heat gain density, 10W/m^2, 15W/m^2, and 20W/m^2. Based on the range of canyon aspect ratios chosen, these heat gain densities are intended to be reasonable estimates of typical thermal loads for residential buildings in urban areas.

The resistance-capacitance model can similarly be used to calculate an outdoor temperature that accounts for the effects of the urban environment. For the wind parameters, as discussed in Section 1.1.1, it is crucial that the wind speeds used to compute the wind pressures are taken at the reference condition of the wind speed used to derive the wind pressure coefficients. In Figure 2-6, the wind speed values approximate measurements in the urban area at a height of 100m, and thus the pressure coefficients to be used with this figure should likewise be referenced to a velocity at 100m in the urban area. Chapter 4 discusses both the choice for this reference condition and how one might obtain the requisite wind speeds. Values for the wind pressure coefficient difference, in particular the magnitude of the reduction in pressure difference that one might encounter in urban areas due to the shielding of neighboring buildings, is investigated in Chapter 3.

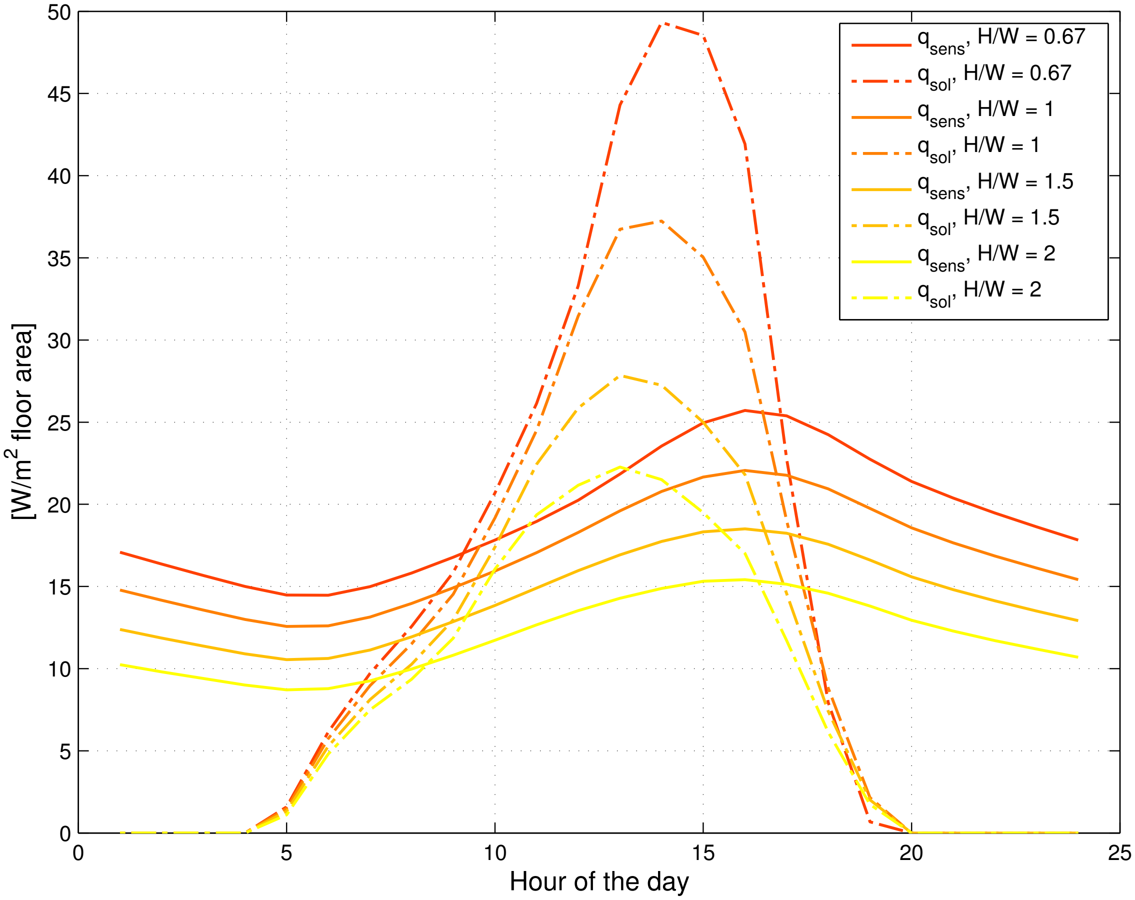

Figure 2-7: Heat gain density profiles for various canyon aspect ratios.

2.2.2 Comparison of results to *CONTAM*

CONTAM is a widely-used multi-zone airflow and contaminant transport analysis program that can calculate airflow rates for simple geometries if the temperatures are known a priori [33]. It can thus be used to check for consistency between flow rates computed from the derivation in Section 2.2.1 and those obtained from the program. We consider the case of $h = 1.5$m, heat gains of 20W/m^2, and a wind speed of 5m/s (red curve in Figure 2-6a). Using the already computed indoor temperatures, and again assuming $T_{out} = 300$K, we can calculate the flow rates from Equations 2.35 and 2.36 and plot them as a function of wind pressure coefficient difference. We can then model the same geometry in *CONTAM*, and use the program to compute the flow rates for several wind pressure coefficient differences and their corresponding temperature differences as determined from Figure 2-6a. The analytical results are shown in Figure 2-8 and compared to the simulation results for a few values of ΔT and ΔC_p in Table 2.1. It is clear that the results obtained analytically from the derivations in Section 2.2.1 are nearly identical to those calculated by *CONTAM*. When appropriate, designers can thus confidently rely on the graphical representations of the preceding section in lieu of more black-box type multi-zone airflow analysis tools.

Table 2.1: Comparison of airflow rates calculated from analytical derivation and *CONTAM*

ΔT (K)	ΔC_p	$Q_{analytical}$ (m^3/s)	Q_{CONTAM} (m^3/s)
~ 0.295	10^{-1}	2.264	2.233
~ 0.937	10^{-2}	0.712	0.702
~ 1.701	10^{-3}	0.392	0.382

2.2.3 Implications for design and analysis

Figure 2-6 indicates that for cases when the wind pressure coefficient difference is very low, as what one might expect of dense urban areas, a designer need not consider wind-

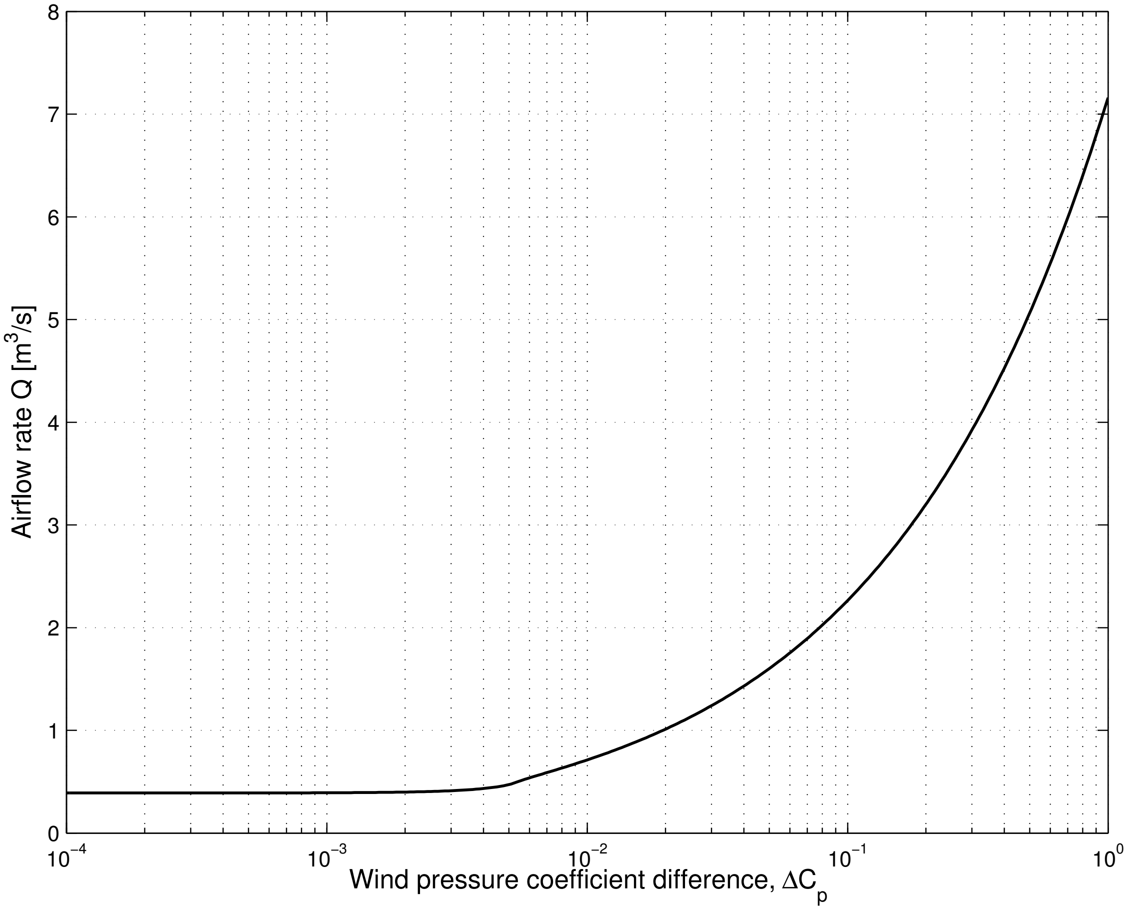

Figure 2-8: Volumetric flow rate as a function of wind pressure coefficient difference for geometry with opening height $h = 1.5$m, wind speed $u = 5$m/s, and heat gain density $q = 20$W/m^2.

driven effects and can focus solely on enhancing the buoyancy-driven ventilation of the space. Furthermore, the analysis of a buoyancy-dominated flow is significantly simpler than that of a wind-dominated flow, as the indoor-outdoor temperature difference can be estimated directly from knowledge of the heat gains and opening height (see Section 2.2.2). For example, the set of curves in Figure 2-6a and that of Figure 2-6b each follow a similar shape that arises from the three flow regimes discussed in Section 2.2.2; the only difference is that for the opening height of 0.75m, the upper bounds of the indoor-outdoor temperature differences are lower by several tenths of a degree centigrade than those for the opening height of 1.5m. These differences would be even more pronounced for higher heat gains, such as for small commercial spaces, or if a designer was considering opening heights less than 0.75m. Hence, in dense urban areas, it is likely that the opening height is the most important variable that a designer can control to enhance the natural ventilation potential of a space.

We can further study how much buoyancy-driven flow is actually contributing to lowering the indoor temperature in this buoyancy-dominated regime. If we consider a hypothetical scenario in which there was no buoyancy-driven bidirectional flow, then the only cooling would be due to wind-driven flow. However, since this regime is characterized by very small wind pressure coefficient differences, the cooling that the wind can provide would be very small as well and consequently we would expect the indoor temperatures to be quite high. Figure 2-9 illustrates this scenario for the geometry with the opening height of 1.5m and a wind speed of 5m/s. Three heat gain densities are depicted, similar to Figure 2-6. The solid colored lines represent the hypothetical temperature curves if bidirectional flow did not exist; in the case of very lightweight wall constructions, these temperatures would take on lower values due to conductive heat transfer that here has been assumed to be negligible. The dashed lines are lines of constant indoor-outdoor temperature difference if hypothetically there was no wind-driven flow. The gray lines refer to the real scenario, and are therefore identical to the curves in Figure 2-6a, where both wind and buoyancy forces interact to influence the natural ventilation potential and the indoor temperature. From this information, we can deduce that for a heat gain density of 15W/m^2, the

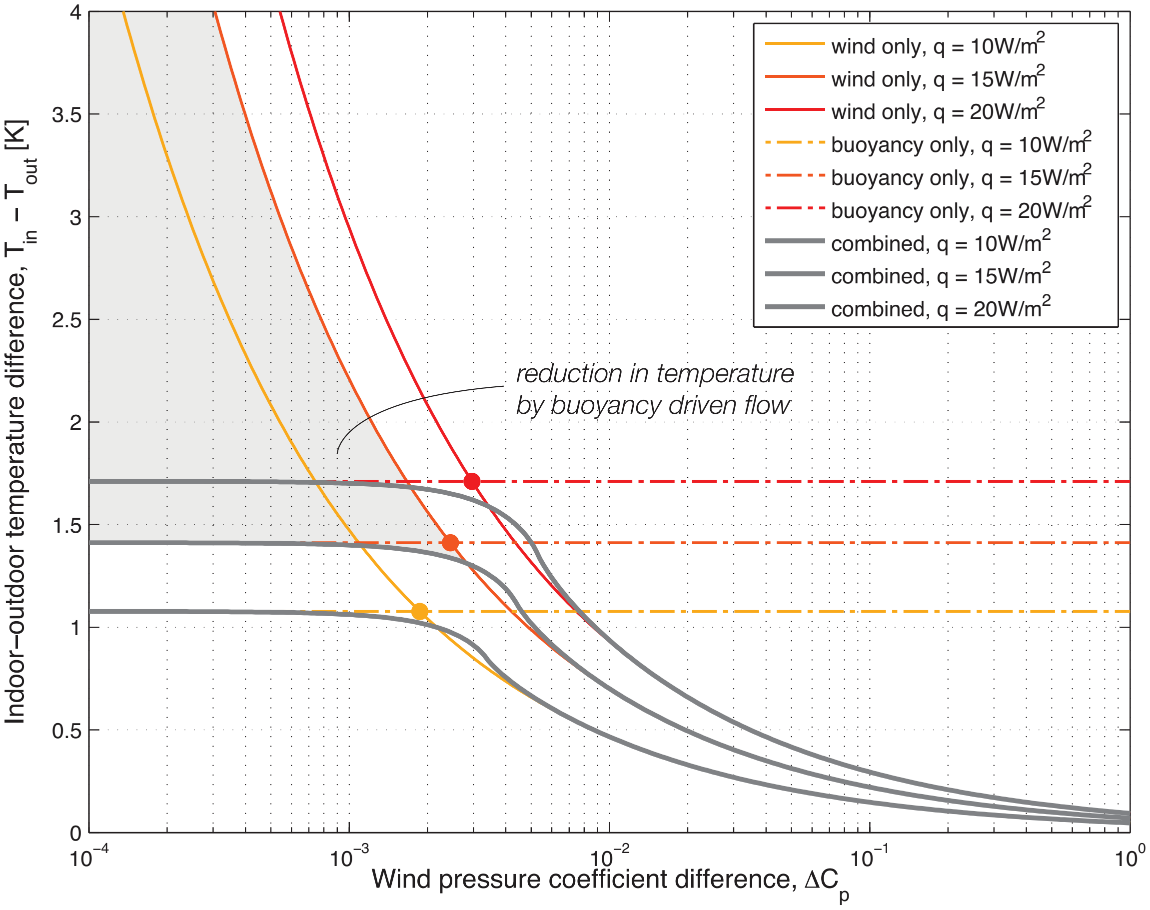

Figure 2-9: Indoor-outdoor temperature difference as a function of wind pressure coefficient difference for geometry with opening height $h = 1.5$m, with shaded area showing reduction in temperature by buoyancy-driven flow. q is the zone heat gain density.

shaded area in Figure 2-9 indicates the reduction in indoor temperature that can be attributed to bidirectional flow. Physically, since buoyancy-driven flow increases with temperature difference, the indoor temperature does not continue to rise as the wind pressure difference gets smaller because at these higher temperatures, the bidirectional flow is large enough to exactly offset the heat gains. The temperature is capped at the system's steady state temperature. It is evident that buoyancy effects can reduce the indoor temperatures by several degrees centigrade and can thus provide a considerable amount of cooling and contribute tremendously to thermal comfort in urban areas where the potential for wind-driven ventilation is very low.

Using Figure 2-9 we can also compare how the temperatures of a hypothetical purely wind-driven flow or a hypothetical purely buoyancy-driven flow compare to those of the combined flow that happens in actuality. The gray lines representing the realistic case trace over the solid colored lines exactly up to $\Delta C_p \sim 10^{-2}$, then there is a small region where the gray lines diverge until they again reconnect at $\Delta C_p \sim 10^{-3}$ to trace over the buoyancy-driven dashed lines. These curves suggest that a combined calculation accounting for the interaction between the two driving forces is not entirely necessary; fairly accurate results can be obtained from a separate analysis that switches from wind-driven to buoyancy-driven flow at the intersection point (shown as colored circles in Figure 2-9).

This section has highlighted the importance of buoyancy-driven bidirectional flow. Airflow patterns in dense urban areas are complex and a challenge to predict, but if it can be shown that natural ventilation is generated primarily by buoyancy effects in these dense urban areas, much of the complexity can be stripped away. The analysis can be considerably simplified, since a readily computed upper bound to the indoor-outdoor temperature difference can provide designers with a reasonable first-order estimate of thermal comfort.

2.3 Assumptions and limitations of this model

The derivation of the analytical solution in Section 2.2.1 relied on the Bernoulli equation and the orifice model and their respective assumptions. One key assumption concerned itself with the streamlines of the flow entering the room, requiring them to be parallel and horizontal at the opening. A consequence to this is that the pressure distribution of the inflow stream is assumed to be equal to the pressure at the same height in the receiving room. While these assumptions are likely to be valid for small openings or orifices, they become more difficult to justify when they are applied to openings that are large relative to the wall height, as was done in the derivation of the analytical solution. In real flows, the streamlines are often far from horizontal and parallel, as can be seen in the sketch below of an actual flow observed through a doorway (Figure 2-10). Here, the difference in temperatures between the adjoining spaces gives rise to curved plumes [10].

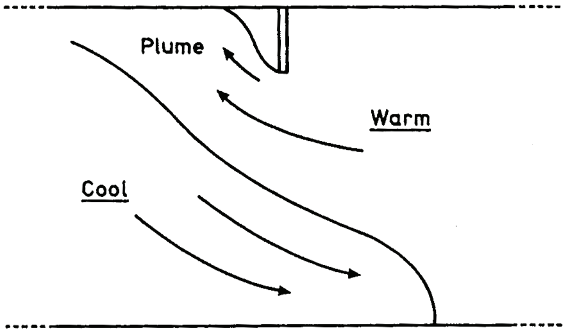

Figure 2-10: Sketch of observed flow through a doorway [10]

An alternate model, the two-layer hydraulics model, accounts for the opening geometry and consequently does not assume the streamlines to be horizontal [8]. It also allows for flow separation at the opening edges, which the orifice model does not but corrects using a discharge coefficient (Equation 2.31). However, despite these differences, for the case of purely buoyancy-driven bidirectional flow, both models yield a flow rate that is proportional to $A(g'h)^{\frac{1}{2}}$ where only the constant of proportionality differs. For the orifice model, the constant of proportionality $C = \frac{1}{3}C_d$ while for the hydraulics model, $C = \frac{1}{4}$ for a window and 0.243 for a typical doorway [10]. If C_d is assumed to be the typical value for sharp-edged openings of 0.6, then the coefficients for the two models are very similar. Coefficients obtained from both small-scale and full-scale experiments range from 0.15-0.27 [10], and hence the theoretical values agree quite well with each other and also with the experimental data available.

Chapter 3

Wind pressure coefficients for buildings in urban areas

A key aspect to estimating the indoor-outdoor temperature difference from Figure 2-6 is first determining an appropriate value of the wind pressure coefficient difference for the building situated at the urban site. This chapter presents results from published work on this topic, assembles and processes the data to allow for a graphical representation in terms of morphological parameters, and concludes with a brief discussion on some of the limitations of this data.

3.1 Existing data

This section discusses the findings from a literature survey conducted on surface wind pressure coefficients. It is important to note that the published data is rather limited; specifically, most of the experiments discussed here are based on idealized urban areas, usually large arrays of equally-sized blocks with no variation in height, and subsequently can be difficult to extend to more realistic urban sites.

3.1.1 Wind tunnel and numerical studies

In the 1970s a team of investigators from the University of Sheffield conducted a series of extensive wind tunnel experiments that were the first of their kind to examine the surface pressure field and flow phenomena of groups of roughness elements for the purpose of ventilation studies of low-rise buildings. Soliman and Lee investigated the influence of group density and pattern and incident flow type and direction on the mean pressure distributions experienced by three-dimensional cubic bodies immersed in a turbulent boundary layer. A low-speed wind tunnel with a 2.80m long by 0.61m square working section was used for the tests. Both the central instrumented model and the roughness elements used for the arrays had a side dimension of 20mm. All pressure measurements were taken from a total of 24 tappings equally distributed between the two opposite faces of the model. In order to cover the three different flow regimes discussed in Section 1.3.1, detailed pressure measurements were made for a wide range of element grouping densities, ranging from a plan area density λ_p of 3.125% to 50%, where λ_p is the ratio of the element footprint to the element lot area, with the element lot area being equal to the total area of the array divided by the number of elements (see also Figure 3-13). These plan area densities correspond to canyon aspect ratios $\frac{H}{W}$ of 0.2 to 2.5. In all cases, the size of the array was kept constant at a layout radius to element height ratio $\frac{R}{H} = 14$, a value sufficiently large for the flow to be considered fully-developed at the location of the central model. For a normal layout pattern (Figure 3-1), Figure 3-2 shows the variation of the windward and leeward mean centerline pressure coefficient profiles with plan area density for a wind direction normal to the windward face. The variation of the element drag coefficient C_D with density is shown in Figure 3-3 [27].

Since pressure or form drag is substantially larger than skin friction or viscous drag for flow over bluff bodies, we can estimate the difference in wind pressure coefficients by the drag coefficient C_D. As expected, the wind pressure coefficient difference decreases significantly as plan area density is increased. At a layout density of 50% corresponding to a canyon aspect ratio of 2.5, ΔC_p is 10^{-2} or less, which can be

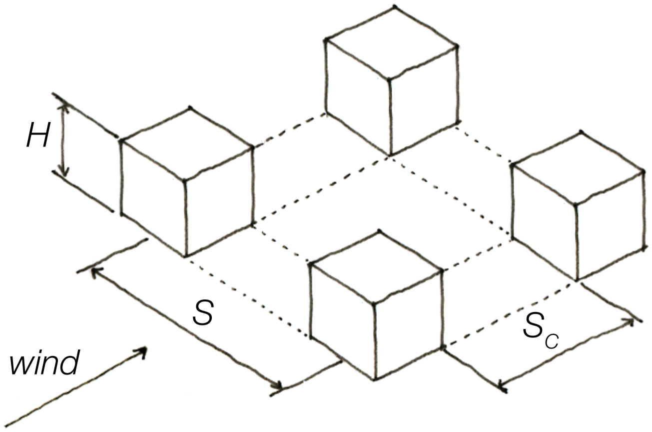

Figure 3-1: Normal layout pattern with element height H, centerline spacing S, and clear spacing S_c between elements in the flow direction.

contrasted with that of an essentially isolated building of canyon aspect ratio 0.2, which has a ΔC_p of about 0.3, several orders of magnitude larger. It is important to clarify here that the pressure coefficients shown in these figures are referenced to a wind speed at free stream, and for these to be applicable to Figure 2-6, they would first need to be converted to a reference condition at 100m. This transformation is carried out in Section 3.2.2.

Hussain and Lee repeated the experiments of Soliman and Lee using a similar but slightly more rigorous approach. They conducted their experimental tests in the Sheffield University Boundary Layer Wind Tunnel, which was rebuilt to have a cross-section of 1.2 x 1.2m and a length of 7.2m as well as a larger speed range. The incident flow consisted of a simulated atmospheric boundary layer wind appropriate for urban terrain. The boundary layer had the following characteristics: a depth of 800m, a power law exponent of 0.28, and a scale ratio of 1:350. The central instrumented model was fitted with 26 pressure tappings on one face. Mean pressure measurements were made on the windward and leeward faces with the wind direction normal to the windward face in all cases. A model array fetch of $\frac{R}{H} = 25$ was used for the low density arrays reducing to $\frac{R}{H} = 10$ for the highest density arrays of the test program; these values were shown to result in fully-developed flow at the location of the central model [20].

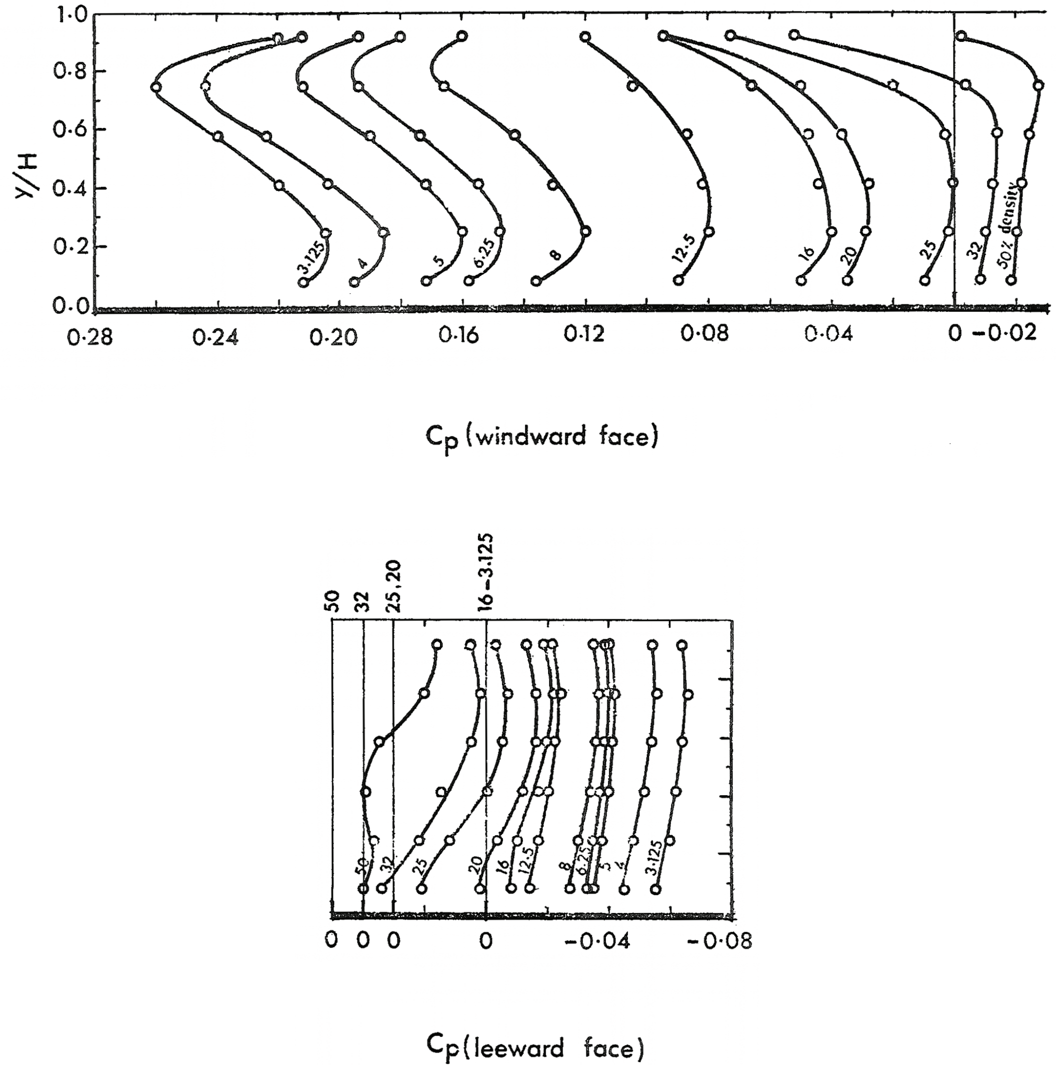

Figure 3-2: Distribution of the windward and leeward mean centerline pressure coefficients for all plan area densities studied [27].

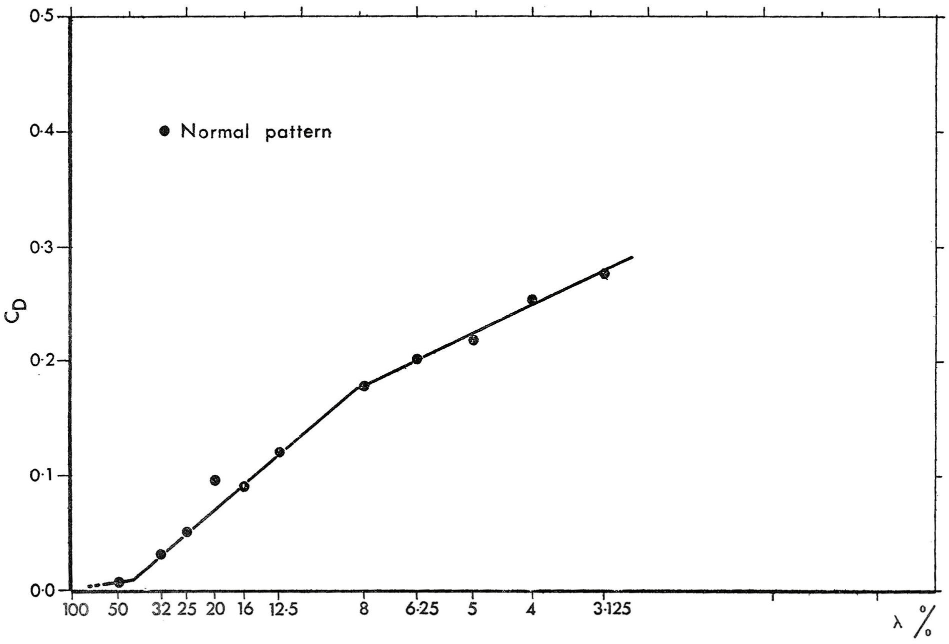

Figure 3-3: Variation of the element drag coefficient with plan area density. Modified from [27].

The test program was divided into a number of parts which utilized different model forms. The initial tests were performed with cubic elements to compare to the findings of Soliman and Lee discussed above. Both the central instrumented model and the roughness elements used for the arrays had a side dimension of 36mm. Thirteen cases of plan area density ranging from 3.1% to 50% were investigated. Figure 3-4 shows the variation of the surface-averaged windward and leeward pressure coefficients, denoted by $C_{p,w}$ and $C_{p,l}$ respectively, and the surface-averaged drag coefficient C_D with plan area density for a normal layout. As in the Soliman and Lee studies, the pressure coefficients were referenced to the free stream velocity [20]. If we examine the data, we see that the values agree with those of the previous study, especially at the higher plan area densities, where ΔC_p again approaches a value of about 10^{-2}.

In the second and third phases of the investigation, central models of different plan forms were used, while the remaining elements in the array were always of the same shape as the central instrumented model. The second series of tests used models with a frontal aspect ratio $A_f = \frac{L}{H}$ of 0.5, 1.0, 1.5, 2.0, and 4.0, where in each case the side aspect ratio $A_s = \frac{D}{H}$ remained square with a 36mm length (Figure 3-5a). Mean

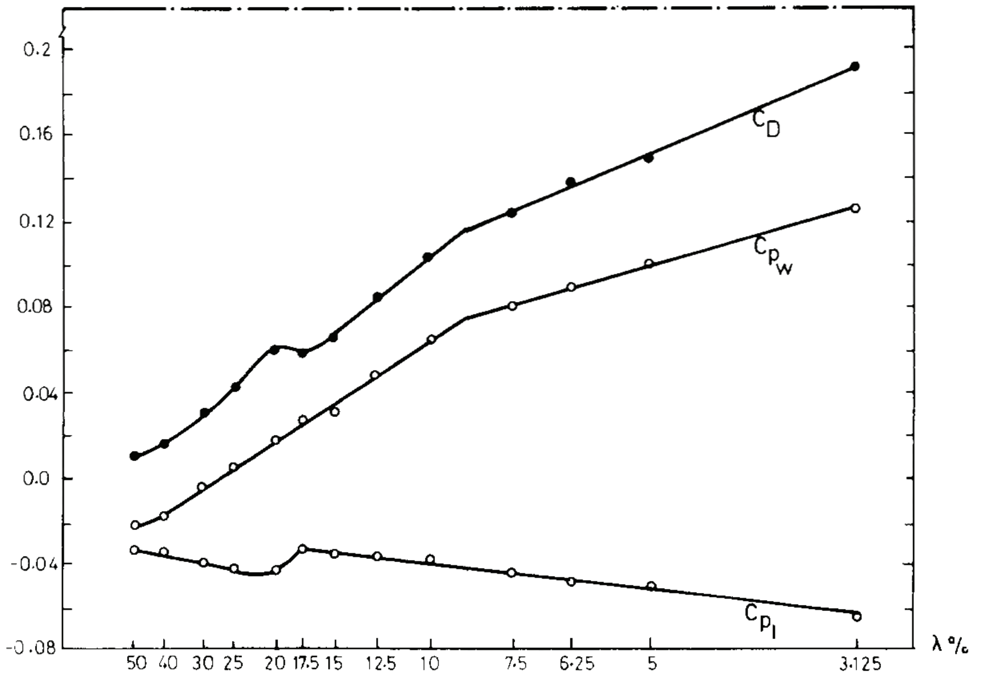

Figure 3-4: Variation of the surface-averaged windward and leeward pressure coefficients and element drag coefficient with plan area density. Modified from [20].

pressure measurements were recorded over a range of 15 plan area densities ranging from 2.5% to 60%. The third series of tests covered the same layout densities but applied to models with A_s of 0.5, 1.0, 1.5, and 2.0, where this time A_f remained square (Figure 3-5b). Figure 3-6 shows the results as a function of element spacing ratio $\frac{S}{H}$ and $\frac{S_c}{H}$, where S is the element centerline spacing, S_c is the clear spacing between elements in the flow direction, and H is the height of the element (Figure 3-1) [20]. There is a clear trend of decreasing drag coefficient with increasing frontal aspect ratio for all values of the element spacing ratio (Figure 3-6a). This suggests that the wind pressure coefficient difference is likely to be smaller for buildings situated along urban canyons than for more cube-like buildings grouped into arrays. For increasing side aspect ratio, the same trend is not as clearly defined (Figure 3-6b).

Tsutsumi et al. carried out a series of wind tunnel experiments focused on blocks of rectangular shape. The blocks were representative of apartment buildings of different number of stories, and a total of three cases of building heights were studied: Model A, B, and C, each 5 stories, 10 stories, and 15 stories tall, respectively. The scale of

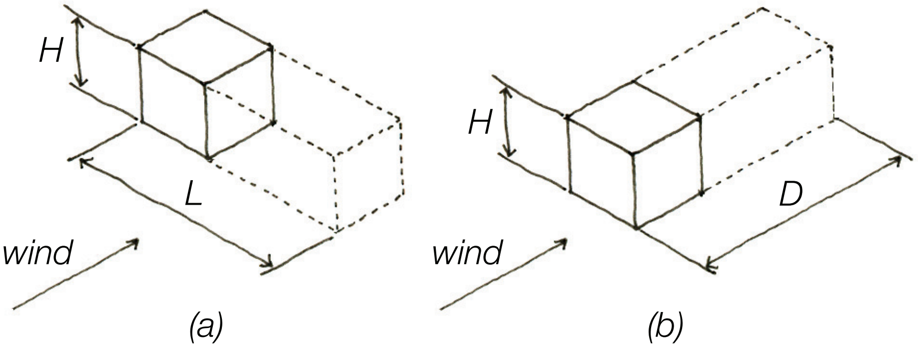

Figure 3-5: a) Varying the frontal aspect ratio $A_f = \frac{L}{H}$ with the side aspect ratio remaining square, b) Varying the side aspect ratio $A_s = \frac{D}{H}$ with the frontal aspect ratio remaining square.

the models was 1/400, and Figure 3-7 and Table 3.1 summarize the full-scale sizes of the models and their layouts. The building volume ratio ϕ is defined as

$$\phi = \frac{nLD}{(a+D)(b+L)} \tag{3.1}$$

where n is the number of stories, L is the length of the building, D is the depth of the building, a is the depthwise spacing and b is the lengthwise spacing between buildings. The building volume ratio is hence similar to the plan area density, except that it accounts for the total floor area of the building rather than only the building's footprint. To investigate the effect of layout density on wind pressure coefficients, ϕ was varied by changing the depthwise direction a. For each model, the lengthwise direction b was kept fixed during all tests with a value proportional to the building height. The length and depth of the building were invariant across all models. The elements in the array were always identical in size to the central instrumented model. For one half of each of the windward and leeward face, the central model was fitted with 12, 16, and 20 pressure tappings for Models A, B, and C, respectively. The tests were conducted in a wind tunnel 25m long with a test section 4.3m in length, 1.5m in width, and 1.5m in height. The approaching wind was a turbulent shear flow that simulated the natural wind over a built-up area and was oriented normal to the windward face. The power law exponent was approximately 0.25, and the reference

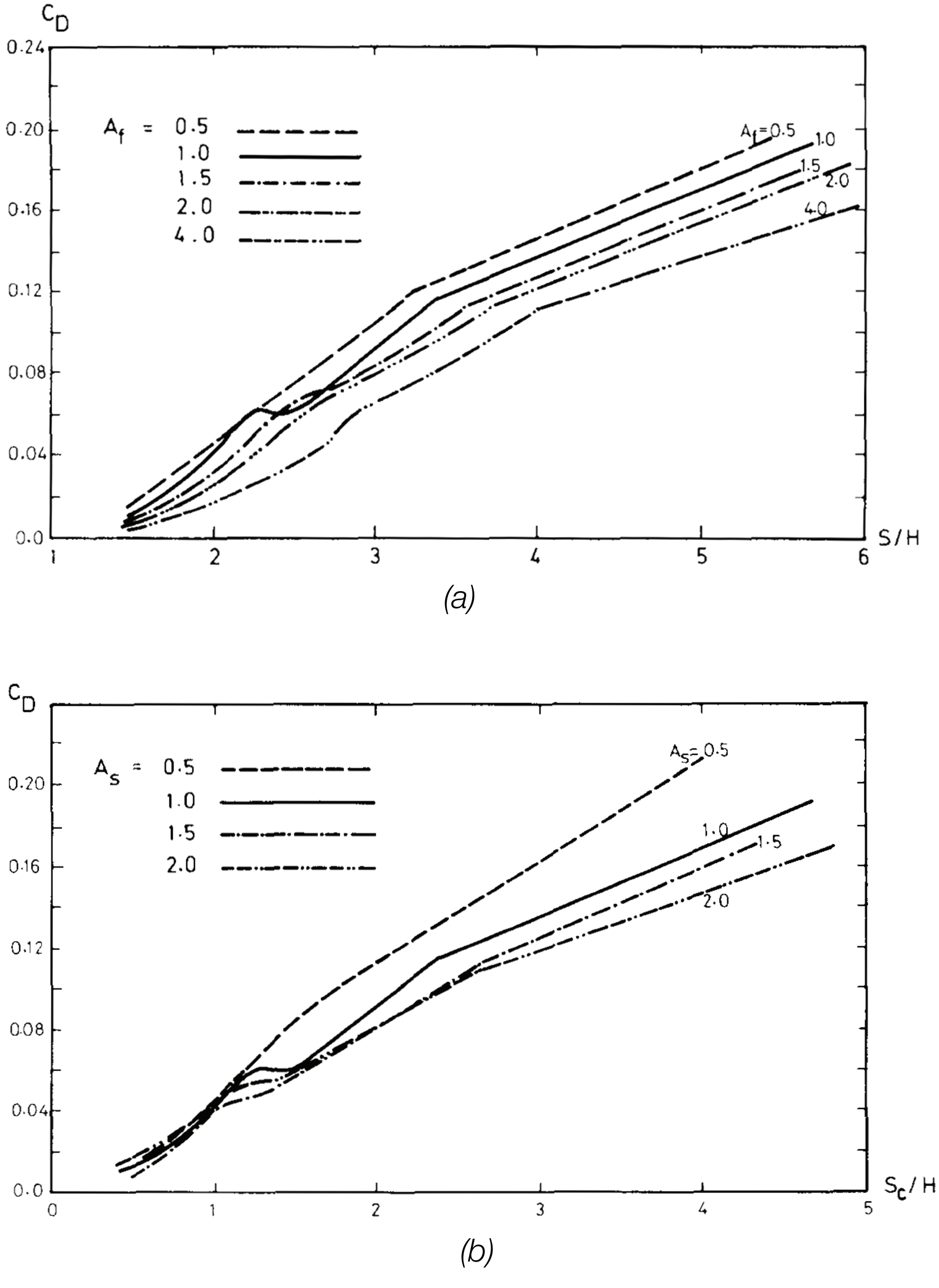

Figure 3-6: a) Variation of drag coefficient with element spacing ratio $\frac{S}{H}$ for arrays of different frontal aspect ratio models, b) Variation of drag coefficient with element spacing ratio $\frac{S_c}{H}$ for arrays of different side aspect ratio models. H is the height of the element, S is the element centerline spacing, and S_c is the clear spacing between elements in the flow direction (see also Figure 3-1). Modified from [20].

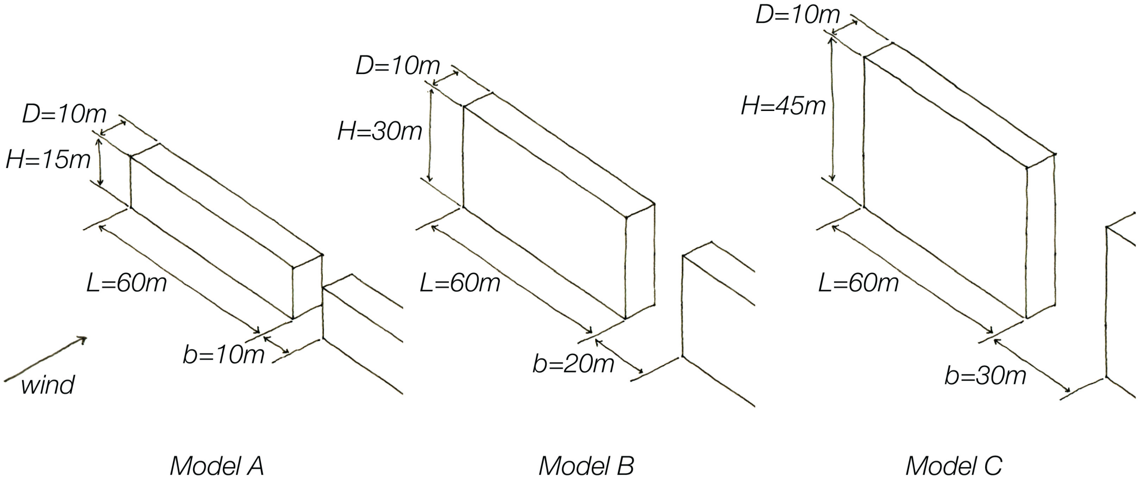

Figure 3-7: Sketch of geometrical parameters.

Table 3.1: Depthwise spacing a

ϕ	Model A	Model B	Model C
50	76.5m	–	–
75	47.2m	89.2m	123.2m
100	32.8m	65.2m	90.0m
125	24.4m	50.0m	70.0m
150	18.4m	40.0m	56.8m

velocity had a value of 8m/s measured without the models present at a height of 750mm (300m full-scale) and a distance 1.5m downstream from the test section inlet. The main results are shown in terms of surface-averaged wind pressure coefficient differences for a normal layout (Figure 3-8). Here, the wind pressure coefficient difference is abbreviated as the wind pressure coefficient. The line numbers refer to the rows of elements in the array, where Line 1 denotes the row closest to the wind tunnel inlet. The array was composed of 10 lines total. For each line, the instrumented model was placed at the center [31].

In this study, the highest building volume ratio tested was 150% which corresponds to a canyon aspect ratio of about 0.8, while in the studies by Soliman and Lee and Hussain and Lee, deeper canyons with aspect ratios as high as 2.5 were included.

Nevertheless, from Figure 3-8 we can still observe a clear reduction in ΔC_p for all model types as ϕ is increased; this is most evident for the center rows of the array where the flow is more fully developed. It is also interesting to note that at the higher densities of the Model A studies, ΔC_p takes on negative values, but only in the second row. If we recall the results by Syrios and Hunt (Section 1.3.3), the authors concluded that negative pressure differences lead to flow reversal for a building flanked by two urban canyons. Based on the results of Figure 3-8, it seems that this phenomenon might only apply to the second row of an array of buildings where the flow is still developing, since ΔC_p takes on quite different and non-negative values in rows further downstream.

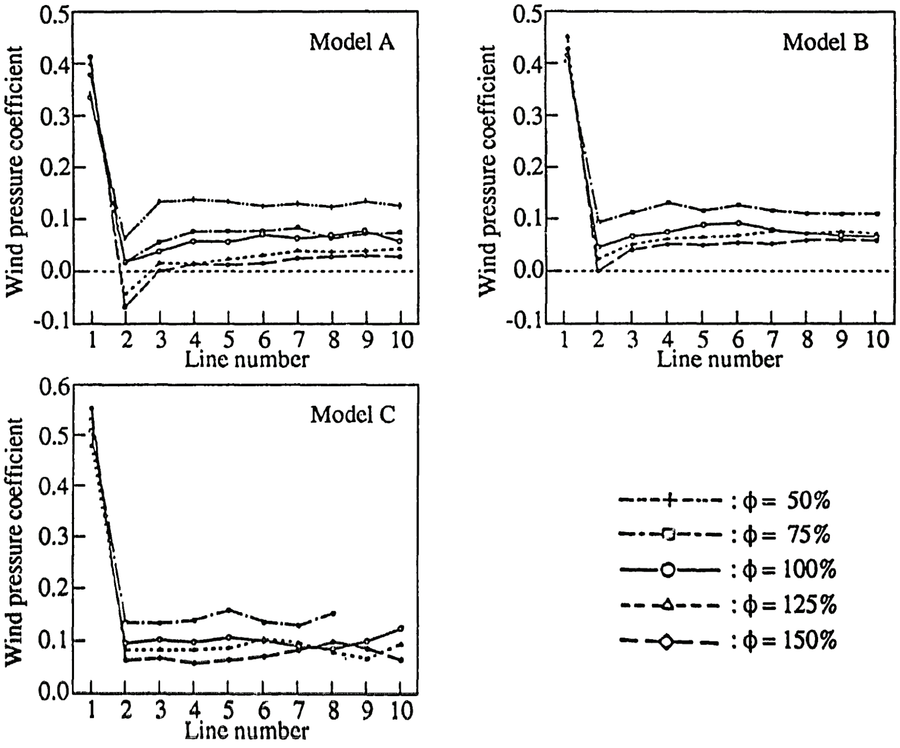

Figure 3-8: Surface-averaged wind pressure coefficient differences for all models and building volume ratios studied. The wind pressure coefficient difference is abbreviated as the wind pressure coefficient [31].

Figure 3-9a summarizes the variation of wind pressure coefficient difference with layout density for Line 5 of the Model A studies. At the highest density, ΔC_p is about 10^{-2}, which agrees well with the results from the Sheffield University experiments.

However, it is important to keep in mind that the pressure coefficients here are referenced to a velocity at a full-scale height of 300m, while the Sheffield experimental results were all normalized to a free stream velocity. To enable cross-comparison, the reference condition will be matched across all the available data in Section 3.2.2. For the same building volume ratio and position within the array, Figure 3-9b illustrates how ΔC_p varies with model height. It follows that buildings with more square frontal aspect ratios similar to Model C yield larger wind pressure coefficient differences than buildings with more elongated frontal aspect ratios similar to Model A. This observation agrees well with the results from Hussain and Lee's frontal aspect ratio studies and further supports the argument that ΔC_ps are likely of lesser magnitude for buildings situated along urban canyons than for more cube-like buildings grouped into arrays.

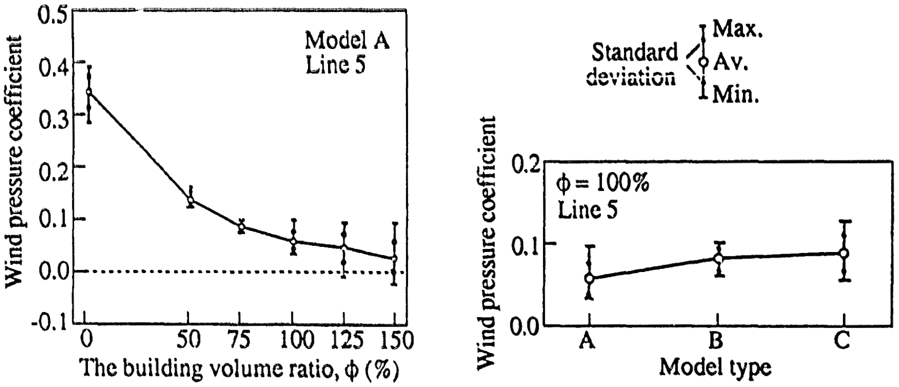

Figure 3-9: Surface-averaged wind pressure coefficient differences for a) Model A Line 5, b) Line 5 of all models at $\phi = 100\%$. The wind pressure coefficient difference is abbreviated as the wind pressure coefficient [31].

Tsutsumi also documented the distribution of the wind pressure coefficient difference for select building volume ratios (Figure 3-10). Except for the isolated model, all data is based on Line 5 of the array [31]. The plots suggest that the variation in ΔC_p across a face is quite small for the layout densities shown. This is true in particular for the shorter model, but even for the taller model, we see that most of the face undergoes little variation. The choice between using local pressure coefficients and surface-averaged pressure coefficients for natural ventilation calculations is discussed in Section 3.2.1.

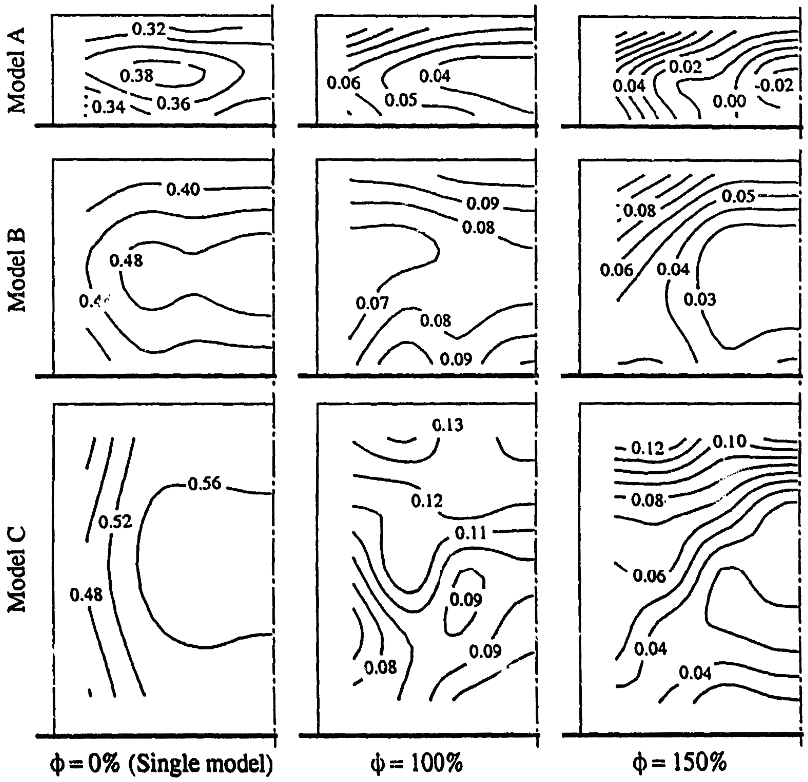

Figure 3-10: Distribution of the wind pressure coefficient difference over the model surface for select building volume ratios [31].

Sini et al. applied numerical simulation to the study of small-scale atmospheric flows within the urban canopy layer for the asymptotic case of infinitely long street canyons. While their main focus was on pollutant transfer, they also investigated the variation of ΔC_p with canyon aspect ratio. The numerical code *CHENSI* was used, and the studies were restricted to 2-D simulations of the street canyon flow field where a moderate horizontal wind blows normal to the street axis. Details of the numerical setup and solution algorithm can be found in [26]. The canyon height H was 20m and the width was varied from $W = 6.6$m to 299.1m, corresponding to canyon aspect ratios $\frac{H}{W}$ of 0.1 to 3. Inlet logarithmic wind profiles for a wind speed of 5m/s at the surface layer height of 100m were chosen to simulate a flow over a surface with roughness length $z_0 = 5$cm. Figure 3-11 illustrates the variation of surface-averaged windward and leeward pressure coefficients with street aspect ratio. Note that this ratio is defined here as $\frac{W}{H}$. All wind pressure coefficients were referenced to a mid-canyon velocity at building height [26].

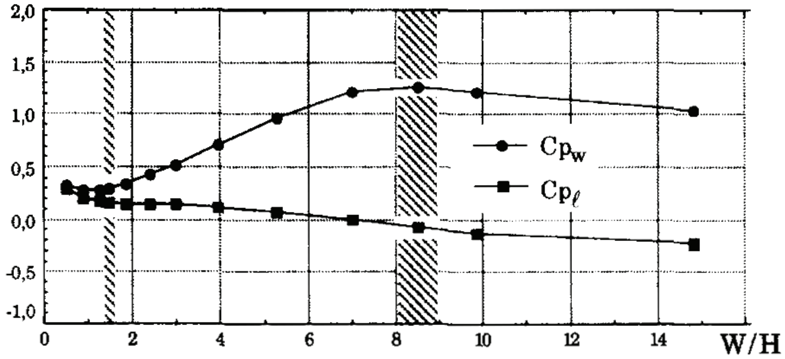

Figure 3-11: Variation of the surface-averaged windward and leeward pressure coefficients with street aspect ratio $\frac{W}{H}$. Modified from [26].

Similar to the previous studies, we observe a significant reduction in ΔC_p as the layout density is increased. For the deepest canyon, $\frac{H}{W} = 3$, ΔC_p takes on a value of about 10^{-2} based on a reference velocity at building height. If these wind pressure coefficient differences were referenced to free stream, we would expect the ΔC_p values to be even smaller than 10^{-2}. From the Hussain and Lee and Tsutsumi studies, we have seen that as the element frontal face is elongated, the difference in wind pressure coefficients decreases. Since an infinitely long street canyon represents the most extreme case of increasing the crosswind length, this ΔC_p estimate of less than 10^{-2} further supports the trend we have seen.

3.1.2 Databases and models

The previous section discussed wind pressure coefficients obtained directly from the experimental data of wind tunnel or numerical studies. Another possibility is to estimate wind pressure coefficients using one of several available databases or analytical models, of which the *AIVC* and *ASHRAE* databases and *CpCalc+* and *CpGenerator* models are just a few examples [7]. However, in many cases, the majority of the original data on which these secondary sources are based is in fact the same experimental data discussed above; in particular the work of Hussain and Lee is frequently referenced [17]. Furthermore, to generate databases or tools from this primary data, the data itself is often times extrapolated and interpolated, basically processed in such a way that the original range of applicability, together with the original assumptions and limitations, is lost [7]. A prime example is a dataset's reference condition, of which there is no mention in one of the most well-known and widely-used databases [1]. A more detailed discussion on the difficulties and inconsistencies of C_p data obtained from secondary sources, especially in regards to sheltered buildings, is available in [7]. For these reasons, the approach chosen for this project was to start with the original experimental data, apply only the most necessary processing that would allow for working consistency among the different datasets, and graphically represent these results in terms of data points rather than regressions or statistics. The next section describes how the experimental data was handled to ensure consistency.

3.2 Processing the data

3.2.1 Local vs. surface-averaged values

A few of the studies discussed in Section 3.1.1 documented pressure distributions or pressure profiles in addition to surface-averaged data. The pressure profiles of the centerline mean pressure coefficients from the Soliman study were shown in Figure 3-2, and the pressure distributions of the wind pressure coefficient differences from the Tsutsumi study were shown in Figure 3-10. Since this work focuses on natural ventilation in urban areas, that is obtaining appropriate estimates of ΔC_p for buildings that are closely spaced, we are most interested in the surface variation of C_p for studies of high layout densities. As an example, we can consider the case of 50% density in Figure 3-2 and the case of $\phi = 150\%$ for Model A in Figure 3-9. For both of these, the variation of ΔC_p over the face of the model is relatively small, certainly smaller than the variation between different layout densities, which is the primary interest of this work. Additionally, in the beginning stages of the design process, the precise locations and configurations of windows are rarely known, hence working at the level of local pressure coefficients would be unnecessarily detailed. We will thus proceed with only the surface-averaged values of the wind pressure coefficient differences, which are more appropriate to the purpose at hand.

3.2.2 Matching the reference condition

For the wind pressure coefficient data to be useful, all the values must be normalized to the same reference condition. Chapter 4 discusses our choice for a reference condition at a height of 100m above the urban area; in the present section, we will focus on the procedure that was used to convert the ΔC_ps from the original reference condition to the new reference at 100m.

The definition of the pressure coefficient was provided in Equation 1.1, where u_{ref} is the chosen reference velocity. To transform this pressure coefficient to a different reference condition, the value needs to be multiplied by a conversion factor that is essentially a function of the ratio of the original reference velocity to the new reference velocity,

$$C_{p,new} = C_{p,orig}\left(\frac{u_{ref,orig}}{u_{ref,new}}\right)^2 = \left(\frac{p - p_{ref}}{\frac{1}{2}\rho u_{ref,orig}^2}\right)\left(\frac{u_{ref,orig}}{u_{ref,new}}\right)^2 = \frac{p - p_{ref}}{\frac{1}{2}\rho u_{ref,new}^2} \tag{3.2}$$

For both the Hussain and Lee and Soliman and Lee studies, characteristics of the simulated atmospheric boundary layer were used to calculate the conversion factors. Table 3.2 summarizes the boundary layer characteristics. For the Hussain and Lee study, the conversion factor was readily computed by applying the power law using

Table 3.2: Boundary layer characteristics for Hussain and Lee and Soliman and Lee studies [20, 27].

	Original reference	Profile	δ	α
Hussain and Lee	Free stream above central model	Power law	800m	0.28
Soliman and Lee	Free stream above central model	Power law	320mm (scaled dimension)	0.18

the given exponent and boundary layer depth,

$$\frac{u_{ref,orig}}{u_{ref,new}} = \frac{u_{\infty}}{u_{ref,100}} = \left(\frac{\delta}{100}\right)^{\alpha} \tag{3.3}$$

where u_{∞} is the free stream reference velocity and $u_{ref,100}$ is the new reference velocity at $z = 100$m at the urban site. For the Soliman and Lee study, the same power law equation was used, but in this case it was necessary to approximate the full-scale depth of the boundary layer from a scaled dimension, since the scaling factor used for the wind tunnel model had not been documented. A height of 100m can be equated to about five times the average building height of an urban area. Applying this approximation to the model height of 20mm, the scaled dimension of δ would be 320m at full scale. The conversion factor can then be calculated from Equation 3.3 and the given power law exponent. Clearly, there will be some uncertainty associated with these conversions; however, it is unlikely that these errors would substantially affect the overall estimates, particularly since we are most interested in the order of magnitude differences in ΔC_p between different layout densities.

For the Tsutsumi and Sini studies, profiles of the mean wind speed were available. These are shown in Figure 3-12. The Tsutsumi study included the mean wind speed profile of the approaching flow from which the conversion factor could be directly determined (Figure 3-12a). It is important to point out that the original reference velocity was measured at a height of 750mm (300m full-scale) without any models present, while the new reference condition to be used is at a full-scale height of 100m over an urban area, hence implying that models should be present. The point of view taken here, which is discussed in greater detail in Chapter 4, is that at a height of 300m, which is typically at least 10-15 times the average building height for an urban area, the velocity with or without models present would be about the same. For this reason, no correction is applied to account for the models being present in the new reference condition. In the numerical investigation by Sini, the pressure coefficients were referenced to building height. Additionally, the depth of the boundary layer was 100m, which, conveniently, is also the height of our new reference condition. We can therefore use the curve of the mid-canyon wind speed at roof level shown in Figure 3-12b to determine the necessary conversion factors, that is $u_H/u_\delta = u_{ref,orig}/u_{ref,100}$. The computed conversion factors were each substituted into Equation 3.2 to calculate the new wind pressure coefficients normalized to a reference velocity at a height of 100m over the urban area. The next section graphically summarizes the results.

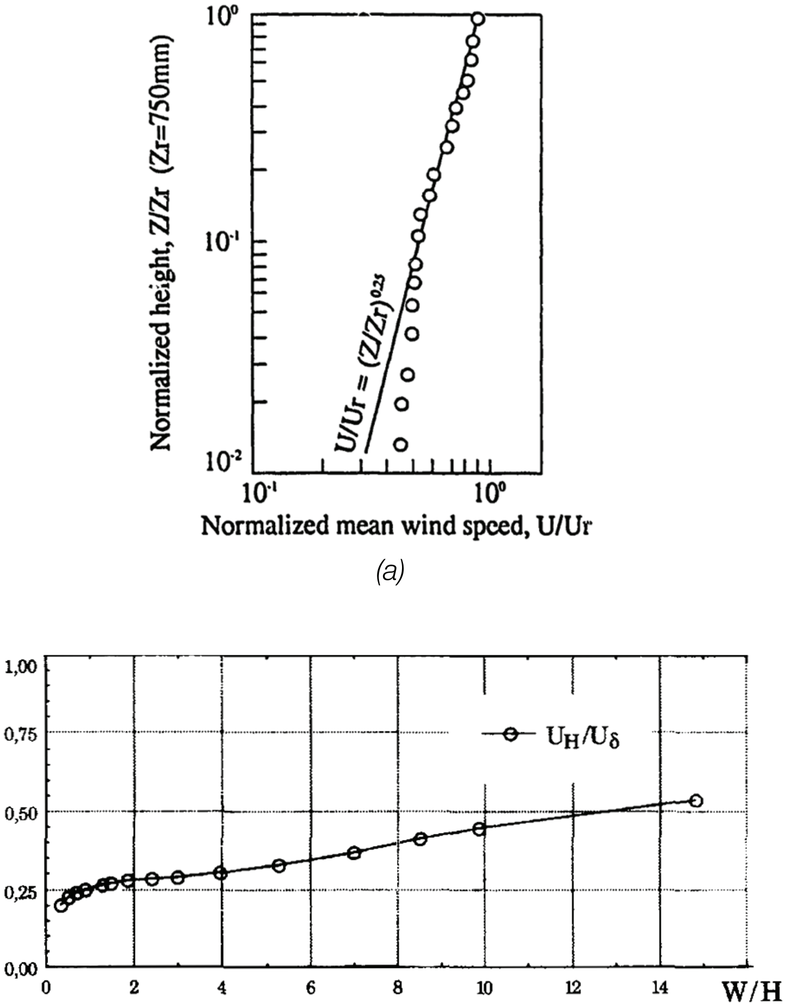

(a)

(b)

Figure 3-12: a) Mean wind speed profile of approaching flow, b) Mid-canyon wind speed at roof level U_H as a function of street aspect ratio $\frac{W}{H}$. Modified from [31, 26].

3.3 Relating pressure coefficients to the morphological parameters of urban areas

To ensure that the wind pressure coefficient data is easily accessible and comprehensible, the information is presented in terms of simple-to-calculate urban morphological parameters, λ_p and λ_f, which are commonly used by urban climatologists and have been shown to effectively synthesize the geometric features of a city [9]. The plan area density or planar area index λ_p has previously been introduced in Section 3.1.1; the frontal area density or frontal area index λ_f is defined as the building vertical area normal to the wind divided by the building lot area. The meaning of both indices is shown in Figure 3-13.

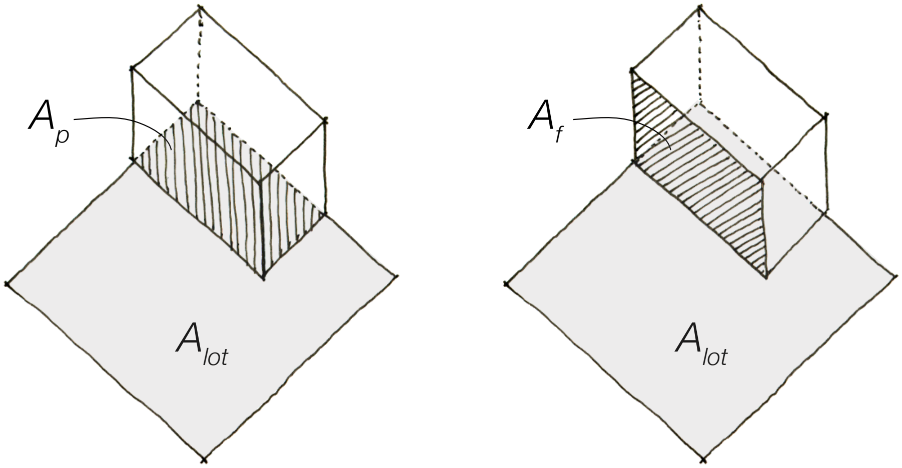

Figure 3-13: Definitions of plan area density λ_p and frontal area density λ_f.

We can obtain typical values for these morphological parameters from surveys that have been conducted on real urban areas [5, 9, 24]. In real urban areas, the obstacles are not all of uniform size and shape, and the λ parameters are defined as averages over the area of interest [18]. Figure 3-14 shows λ_p and λ_f values for 36 cities, primarily North-American but also a handful from Europe and Mexico. The data points are shown with their original land use classification: industrial, residential, or downtown. A table listing the λ_p and λ_f values and land use class for each urban area, together with the source from which the data was obtained, can be found in the Appendix. The plot confirms that industrial areas, with their shorter buildings and more dispersed configurations, have low λ_f and relatively low λ_p values, while downtown areas, with their tall buildings, have large λ_f values and somewhat larger λ_p values as well. The values of the residential areas are situated in-between these extremes. We now have a better idea of typical ranges for λ_p and λ_f, and we will soon be able to apply this information to develop a deeper, more realistic understanding of the wind pressure coefficient data that has been collected.

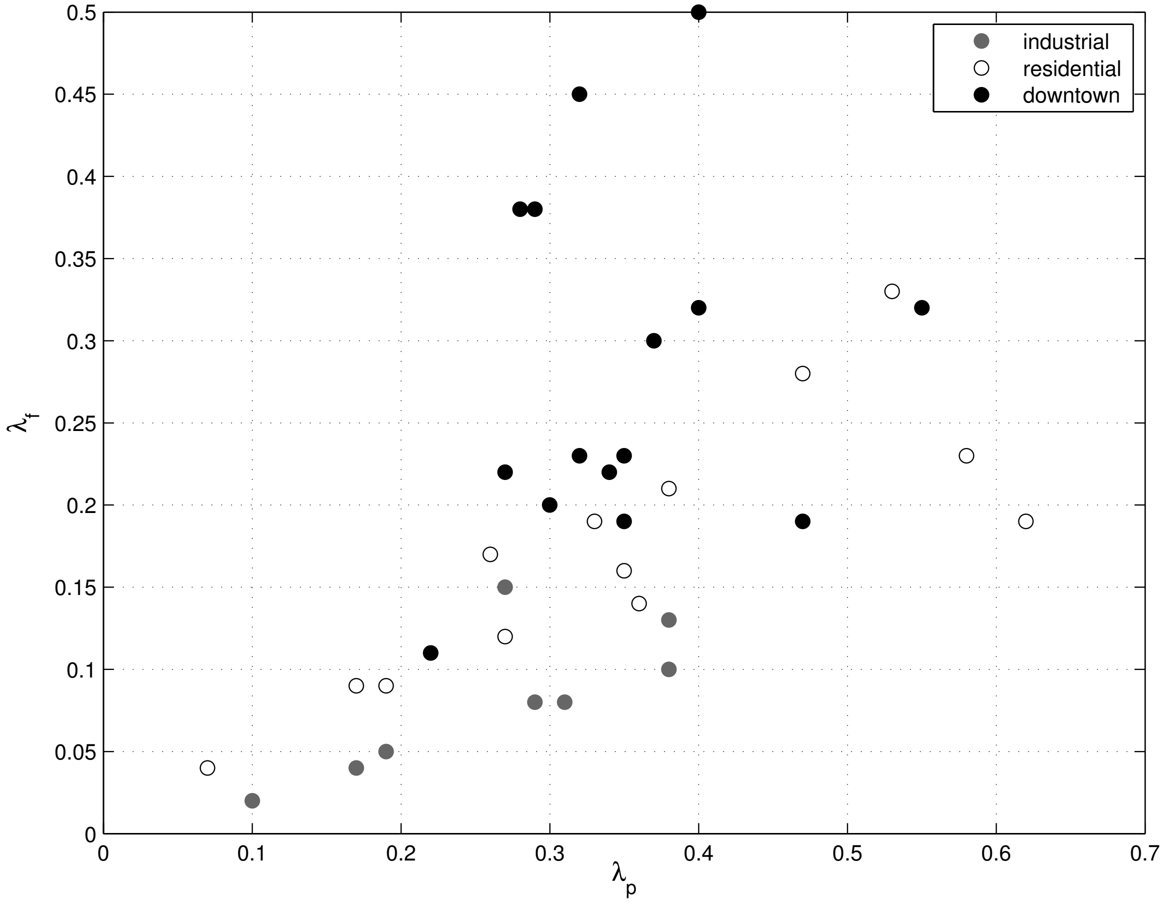

Figure 3-14: λ_p and λ_f values for real cities [5, 9, 24].

We can compute λ_p and λ_f for the layout densities of the collected pressure coefficient data, and visualize how ΔC_p varies with these morphological parameters. Figure 3-15 plots the surface-averaged wind pressure coefficient differences, referenced to a velocity at 100m above the urban area, as a function of λ_p and λ_f. The data obtained from the Sini study is not included here, since it is not possible to compute the λ

parameters for infinitely long street canyons. The figure indicates that as the plan

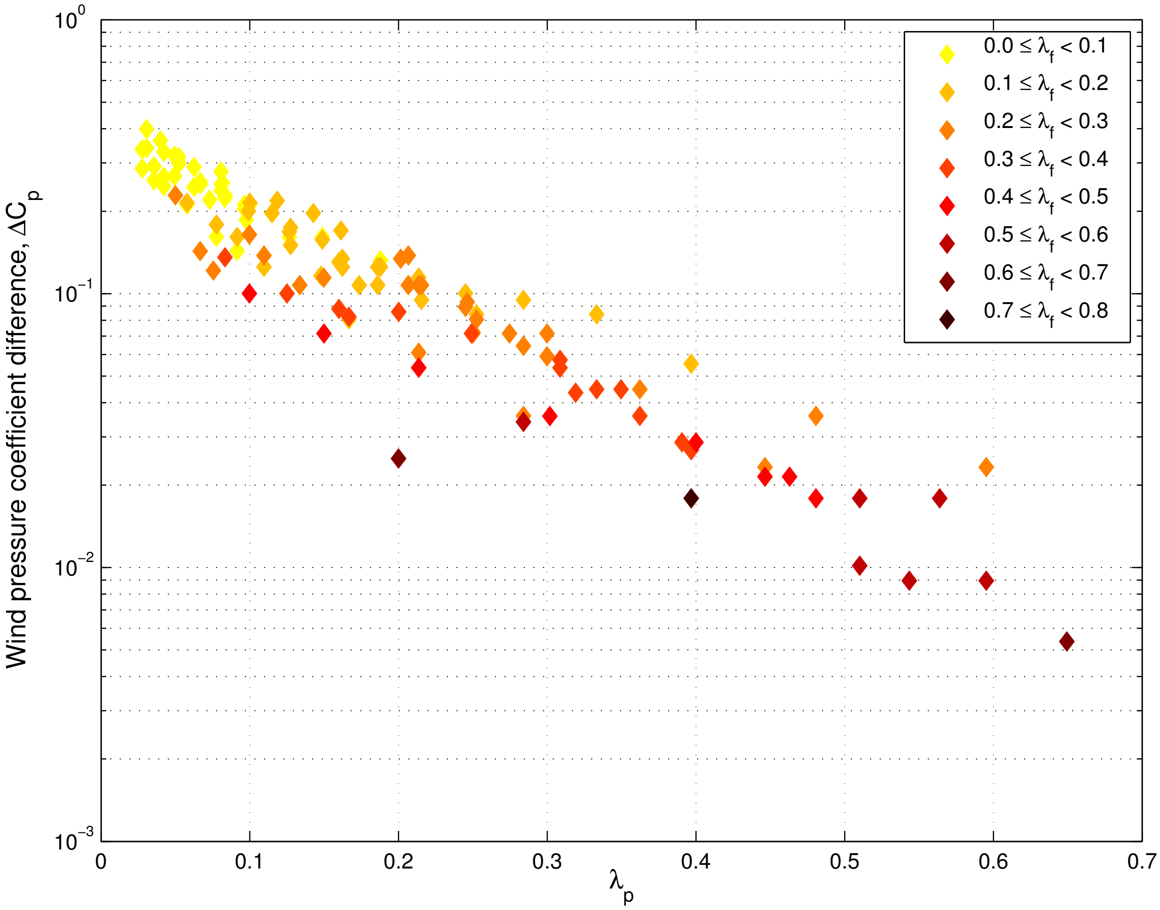

Figure 3-15: Variation of surface-averaged wind pressure coefficient differences with λ_p and λ_f.

area density is increased, ΔC_p decreases. Furthermore, as the frontal area density is increased, ΔC_p also decreases. The ΔC_p values range from about 0.005 to 0.5, hence spanning several orders of magnitude. The figure also suggests that small values of λ_p tend to correlate with small values of λ_f, and large values of λ_p with large values of λ_f. While at present this is only a feature of the dataset and the experimental studies conducted, it might in fact also be representative of real urban areas as was seen in Figure 3-14 above. The collected wind pressure coefficient data can alternately be visualized in terms of canyon aspect ratio $\frac{H}{W}$ and frontal aspect ratio $\frac{L}{H}$, where the side aspect ratio $\frac{D}{H}$ is kept square (see also Figure 3-5a); these results are shown in Figure 3-16 with the data by Sini included. We observe a clear trend of decreasing

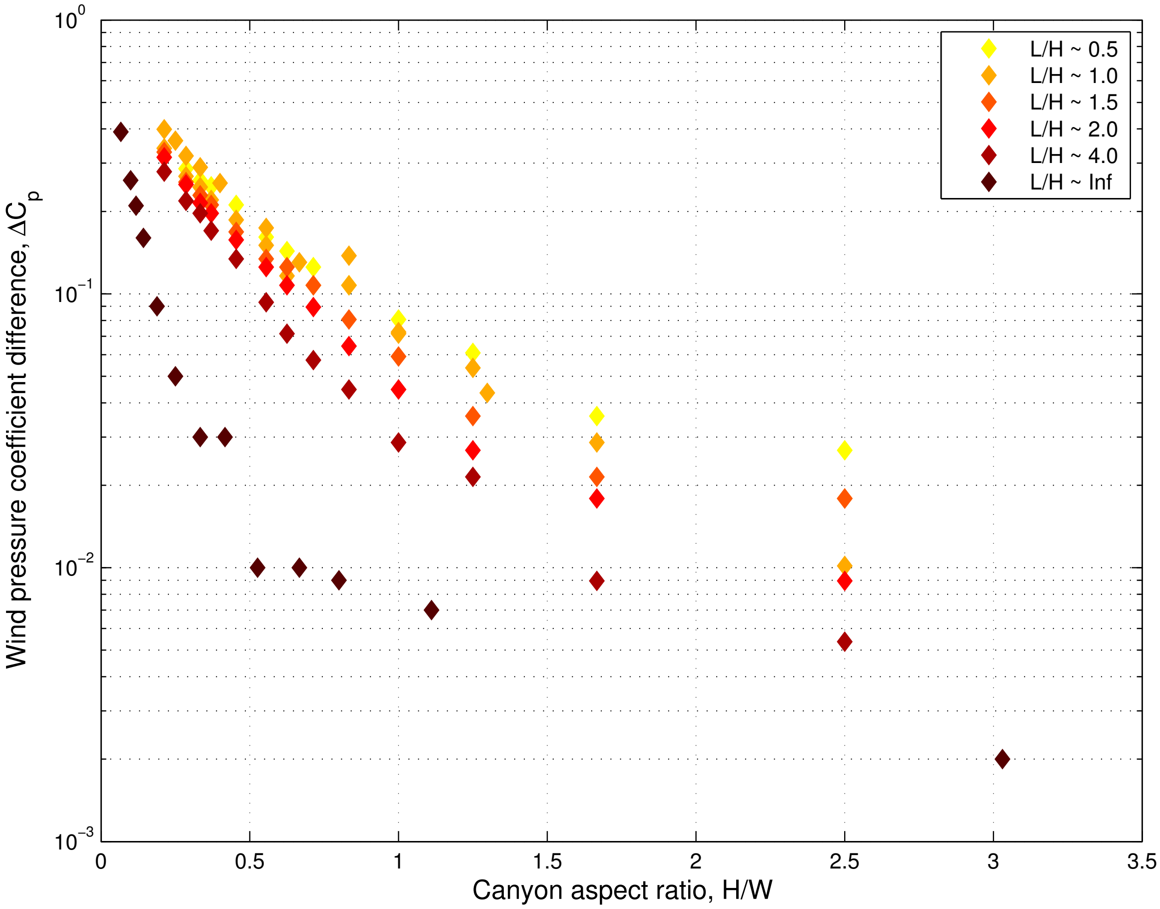

Figure 3-16: Variation of surface-averaged wind pressure coefficient differences with $\frac{H}{W}$ and $\frac{L}{H}$ for $\frac{D}{H} = 1$.

ΔC_p with increasing $\frac{L}{H}$ for a given $\frac{H}{W}$ and $\frac{D}{H}$, confirming that wind pressure coefficient differences indeed decrease with frontal aspect ratio, as was hypothesized from the experimental studies of Section 3.1. For very long street canyons with high aspect ratios $\frac{H}{W}$, the wind pressure coefficient difference can be less than 10^{-2}. Lastly, we can coarsely overlay the land use class information from Figure 3-14 onto Figure 3-15 to gain a better understanding of the magnitudes of ΔC_p that we might expect in real urban areas. This is shown in Figure 3-17. The three shaded regions represent the three different land use classes, with industrial land use at the very top, residential land use slightly below, and downtown land use at the bottom. As expected, the ΔC_ps for industrial areas are quite large, at an order of magnitude of about 10^{-1}, while the ΔC_ps for residential areas span a wide range from about 10^{-1} to 10^{-2}. For

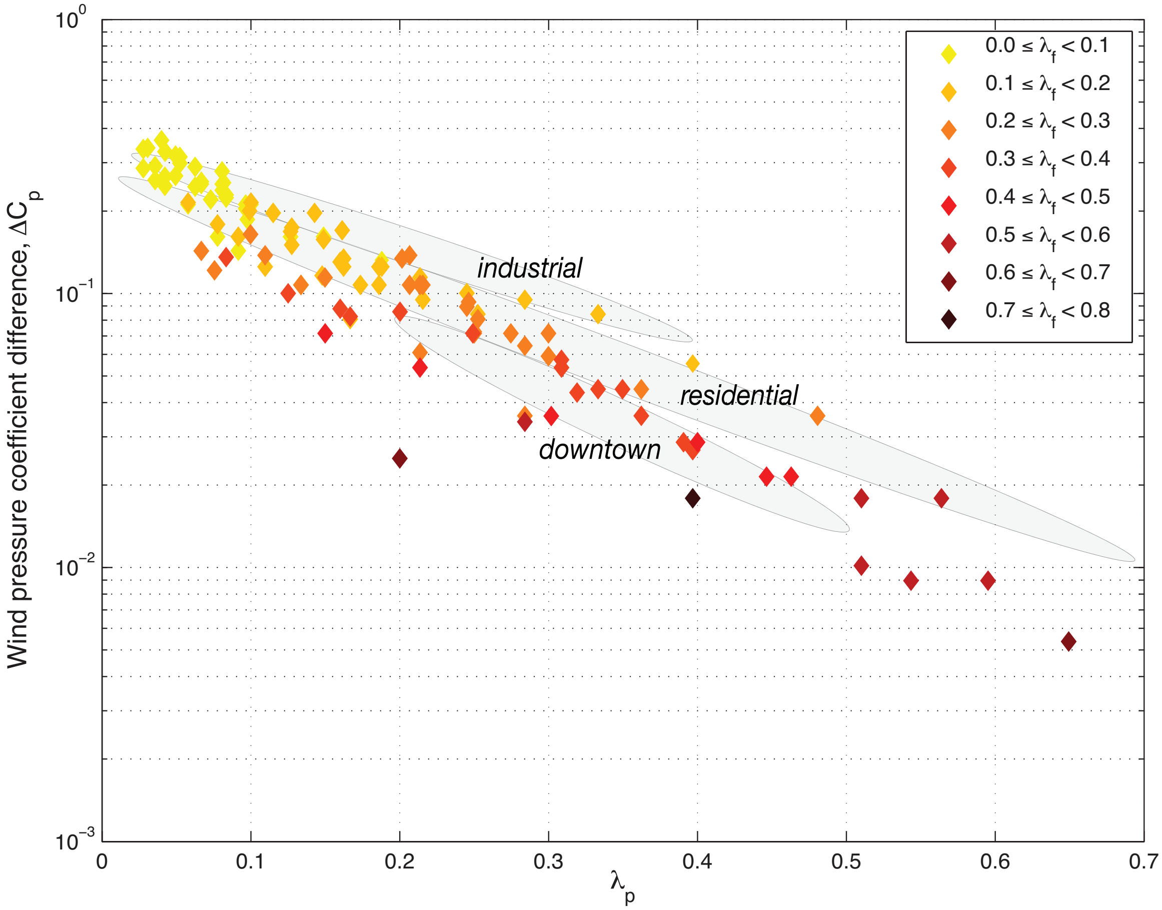

Figure 3-17: Surface-averaged wind pressure coefficient differences as a function of λ_p and λ_f with land use class data from real cities superimposed.

the downtown areas, the ΔC_ps are about 10^{-2}. Hence, based on the current land use data, none of the urban areas are identified by ΔC_ps lower than 10^{-2}. If we now refer back to Figure 2-6, which illustrates the variation of ΔT with ΔC_p, we might be quick to conclude that the buoyancy-dominated regime would never happen in actuality. However, there are several reasons why ΔC_ps in reality might actually be lower than those shown here and why the buoyancy-dominated regime matters. Firstly, the λ_p and λ_f data shown in Figure 3-14 is based primarily on surveys of North American cities with only a handful of data points from Europe and Mexico. European and also Asian cities typically have denser urban layouts with higher λ_p values and possibly also higher λ_f values, which would result in ΔC_ps lower than those within the shaded regions of Figure 3-17. Unfortunately, no other suitable data from surveys conducted on cities outside of North America could be found. Secondly, the ΔC_p data plotted in Figure 3-15 (and 3-17) is based on experimental studies where the wind direction was always kept normal to the windward face, meaning the ΔC_ps shown here are at their maximum value. In reality, the wind will change directions frequently, and the ΔC_p will therefore take on magnitudes that are less than this maximum value. Lastly, given that the flow field in urban areas is complex and constantly changing, the upper temperature bound of the buoyancy-dominated regime might actually be a preferred and more convenient first-order estimate to establish the indoor-outdoor temperature difference since it is easy to calculate and robust to many of these uncertainties.

In summary, Figure 3-17 with the superimposed land use class regions could serve as an alternative to computing λ_p and λ_f values at times when a quick assessment of ΔC_p is needed or when the geometric parameters are unavailable or unknown. Either approach, evaluating ΔC_p from land use class information or from λ_p and λ_f values, would provide a designer with a reasonable estimate of the wind pressure coefficient difference for the urban area under consideration, which could then be used in conjunction with Figure 2-6 to determine the indoor-outdoor temperature difference.

3.4 Limitations to the data

We conclude this chapter by briefly mentioning some of the limitations associated with the wind pressure coefficient data that has been collected. Figures 3-15 and 3-17 are only intended to provide designers with general trends and order-of-magnitude estimates of how the wind pressure coefficient difference varies with urban morphology; they are not capable of offering precise predictions of ΔC_p. This is in part due to the studies from which the data was collected, which in all cases were modeling idealized urban scenarios: a fully developed flow over large arrays of equally sized buildings with no variation in height. In real urban areas, the standard deviation of obstacle heights can be as large as 0.5 to 1.0 times the average obstacle height [18]. Despite these limitations, for most cases, the wind pressure coefficient data can still provide useful first-order estimates that could help guide decision-making during the early stages of the design process.

Chapter 4

Estimating velocities at the reference condition

In the previous chapters, we derived the natural ventilation physics for a simple geometry and presented wind pressure coefficient data obtained from literature applicable to urban areas. In this chapter, we will discuss the velocities that are needed to apply surface pressure coefficients to natural ventilation calculations. We begin by describing the flow in the atmospheric boundary layer and formulas for obtaining the wind speed profiles, followed by discussing what constitutes an appropriate choice of reference condition for urban areas, and lastly presenting ways for estimating the velocity at that reference location from measurements at meteorological stations.

4.1 Flow in the atmospheric boundary layer

The flow over a city is that of a rough-surface turbulent boundary layer flow, where the surface roughness consists of discrete bluff bodies with irregular geometry and spacing [21]. The influence of the surface is felt in the atmospheric boundary layer (ABL), which roughly forms the lowest 10% of the troposphere. In the ABL, which can reach a height of up to 1-2km during the daytime, wind speed, temperature and moisture profiles are affected by the fluxes of momentum, heat and humidity at the surface [32]. The lowest 10% of the ABL is called the surface layer (SL), and is often divided into three major sublayers: the urban canopy layer (UCL), which is the layer occupied by the buildings and closest to the ground; the roughness layer (RL), which extends from the ground to about twice the average obstacle height; and the inertial layer (IL), which spans from the top of the roughness layer to the top of the surface layer [18]. According to Britter and Hanna, the IL is the region where the boundary layer has adapted to the integrated effect of the underlying surface, while in the UCL, the flow at a specific point is directly affected by the local obstacles, and in the RL, the flow is still adjusting to the effects of many obstacles [3]. Figure 4-1 schematically illustrates the different layers. The ABL can be either neutral or non-neutral, and in the case of non-neutral, it can be either stable or unstable. A neutral boundary layer is dominated by mechanical effects generated by wind shear, while a non-neutral boundary layer is dominated by buoyant effects [18]. During the day, these buoyant effects are due to ground surface heating by the sun which increases the convective mixing and produces a deep and unstable boundary layer. At night, cooling of the ground surface suppresses the mixing and the ABL is stable and shallow [32]. More formally, the scaling parameter L can be applied to the surface layer to distinguish between these different characterizations. L is the Monin-Obukhov length and is proportional to the friction velocity u_* cubed divided by the ground surface sensible heat flux H_s:

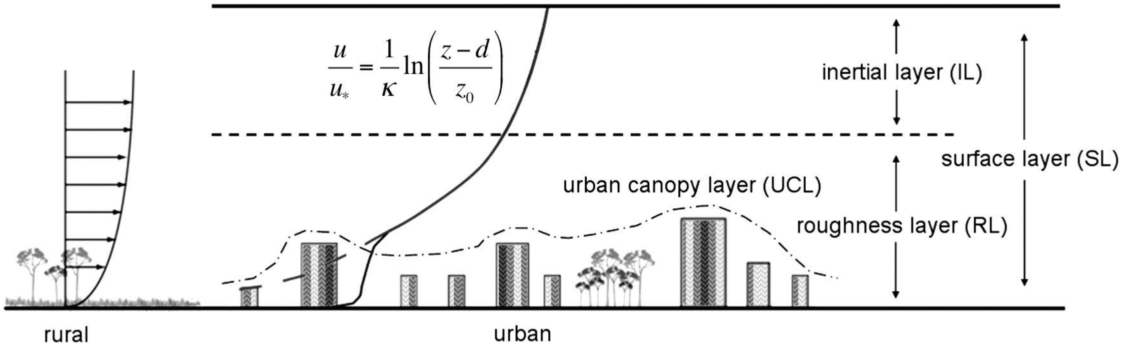

Figure 4-1: Schematic of the urban atmospheric boundary layer. Modified from [3].

$$L = -\frac{u_*^3/\kappa}{gH_s/c_p\rho T} \tag{4.1}$$

where g is the acceleration due to gravity, c_p is the specific heat of air at constant pressure, ρ and T are the air density and absolute temperature, and κ is von Karman's constant taken to be 0.40. The friction velocity is discussed in greater detail below. H_s is positive during the day, with typical values around 200W/m^2. At night, H_s is negative with values around -20W/m^2. The dimensionless ratio z/L indicates the ratio of turbulence suppression or turbulence enhancement by buoyancy to turbulence generation by mechanical wind shear [18]. At heights $z > L$, buoyant factors dominate over the mechanical production of turbulence; at heights $z < L$, mechanical production of turbulence dominates over buoyant factors [28]. When L is very large and z/L approaches zero, such as for very strong winds, the ABL is neutral. For all other values of L, and especially in light winds conditions, the ABL is non-neutral. During the day, L is negative since H_s is typically positive, and the boundary layer is unstable; at night, L is positive since H_s is typically negative, and the boundary layer is stable [18]. Figure 4-2 compares the wind speed profile in the surface layer under these different conditions. As can be seen, the neutral profile appears as a straight line on this semi-logarithmic plot, while for non-neutral situations, the profile deviates slightly from logarithmic, its shape depending on whether the boundary layer is stable or unstable [28]. The wind speed profile for a neutral boundary layer is given

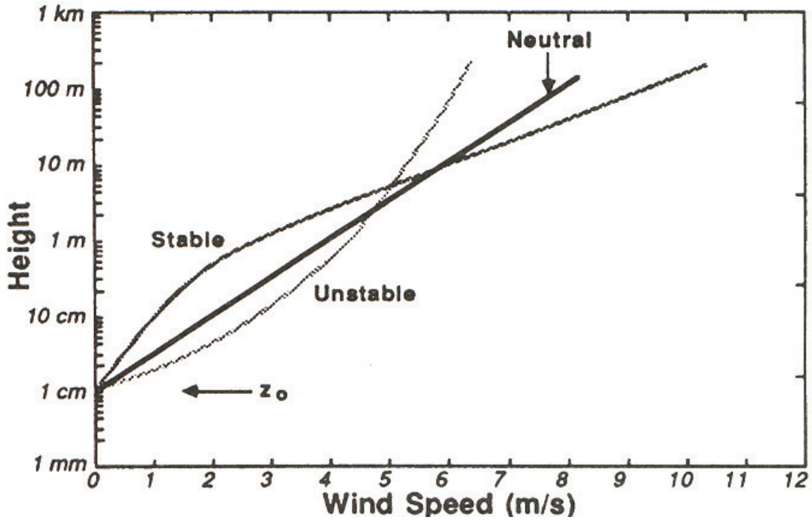

Figure 4-2: Neutral and non-neutral (stable and unstable) wind speed profiles in the surface layer [28].

by a logarithmic relationship that can be derived from similarity theory:

$$\frac{u}{u_*} = \frac{1}{\kappa} ln \left(\frac{z-d}{z_0} \right) \tag{4.2}$$

For non-neutral situations, an additional term that accounts for the buoyancy effects is included,

$$\frac{u}{u_*} = \frac{1}{\kappa} \left[ln \left(\frac{z-d}{z_0} \right) + \psi \left(\frac{z}{L} \right) \right] \tag{4.3}$$

The function $\psi \left(\frac{z}{L} \right)$ is defined for stable conditions, $z/L > 0$, by

$$\psi \left(\frac{z}{L} \right) = \frac{4.7z}{L} \tag{4.4}$$

and for unstable conditions, $z/L < 0$, by

$$\psi \left(\frac{z}{L} \right) = -2ln \left[\frac{(1+x)}{2} \right] - ln \left[\frac{(1+x^2)}{2} \right] + 2tan^{-1}(x) - \frac{\pi}{2} \tag{4.5}$$

where L is defined as above and x is

$$x = [1 - (15z/L)]^{1/4} \tag{4.6}$$

[28] As expected, when z/L approaches zero, Equation 4.3 reduces to Equation 4.2 for a neutral boundary layer. Under these conditions, for a wind speed observation u at a height z greater than approximately twice the average building height and for values of the surface roughness length z_0 and the displacement length d, we can obtain an estimate of u_* [3]. This scaling velocity can then be used to derive the wind speed profile from which the velocity at the desired reference location can be determined. For a non-neutral boundary layer, additional information pertaining to the ground surface heat flux and air temperature is needed to calculate L and u_*.

The friction velocity u_* is the fundamental scaling velocity and is defined as

$$u_* = \left(\frac{\tau_0}{\rho} \right)^{1/2} \tag{4.7}$$

where τ_0 represents the surface shear stress and ρ is the density of air. u_* typically ranges from about 0.05m/s in light wind conditions to about 1m/s in strong wind conditions. z_0 and d are important scaling lengths: z_0 provides a measure of the amount of mechanical mixing introduced by the surface roughness elements, and d describes the vertical displacement of the effective ground level. d is a required input in situations with densely packed obstacles and at heights less than $2H_r$, where H_r is the average obstacle height [18]. When these conditions do not apply, Equation 4.2 can be approximated by Equation 4.8,

$$\frac{u}{u_*} = \frac{1}{\kappa} ln\left(\frac{z}{z_0}\right) \tag{4.8}$$

and Equation 4.3 can be similarly simplified,

$$\frac{u}{u_*} = \frac{1}{\kappa}\left[ln\left(\frac{z}{z_0}\right) + \psi\left(\frac{z}{L}\right)\right] \tag{4.9}$$

There are several methods available for estimating z_0 and d: wind speed profile observations, use of obstacle size and shape (morphology), and use of land-use characterization. A detailed overview of the different approaches and their respective advantages and disadvantages is given in [18]. For typical urban areas, z_0 can be approximated by $0.1H_r$ and d by $0.5H_r$. For our purposes, precise values are unnecessary, especially since the wind speed estimate is not very sensitive to small uncertainties in z_0 and d. These lengths enter Equations 4.2 and 4.3 as natural logarithms, and the natural logarithm of a variable changes by only a factor of 2 for each order of magnitude change in the variable [18].

While the wind profile formulas of Equations 4.2 and 4.3 can provide a solution, that is a non-negative wind speed estimate, down to a height of $d + z_0$, observations from urban and industrial sites suggest that the wind speed profile generally deviates from the logarithmic solution at heights less than about $1.5H_r$ to $2.0H_r$ due to local flow effects around the obstacles [18]. Thus, an appropriate region of validity for the equations ranges from the top of the roughness layer to the top of the surface layer several hundred meters above the ground (Figure 4-1), at which point the velocity profile starts approaching the free-stream or geostrophic wind speed.

4.2 Choice of reference condition

For our discussion of reference conditions, it may be helpful to recall Equation 1.1 that defines the surface wind pressure coefficient:

$$C_p = \frac{2(\overline{p} - p_{ref})}{\rho u_{ref}^2}$$

The reference velocity u_{ref} to which the surface pressures are normalized can be any chosen value, and a commonly cited reference is the velocity measured at building height at or near the location of the building [10, 1]. While this might be a convenient reference condition for isolated buildings, in an urban area the presence of many obstacles leads to complex flow patterns near the rooftops, and hence a velocity at building height would be difficult to estimate. Another commonly chosen reference condition is at free stream; this was used for the reference velocity in many of the wind tunnels studies of Chapter 3. Often it is possible to measure the free stream velocity in controlled experimental studies; however, in real urban areas, additional thermal effects in the atmosphere tend to interfere with a clean estimate (R.E. Britter, personal communication, September 2011). For these reasons, a reference condition at a height of 100m above the urban ground surface is recommended and was chosen for this investigation. For typical urban areas, this height is equal to several times the average building height and is well above the roughness layer such that the flow has adapted to the effect of the urban surface and the standard logarithmic wind speed profile applies.

Now that we have established a suitable reference condition, the next step is to determine how this velocity can actually be estimated from a meteorological measurement, which is the only data a designer will typically have access to. Wind speeds are generally measured at a height of 10m in flat open areas such as airports. To estimate the velocity at a height of 100m in an urban area, the most reasonable approach would be to extrapolate up from the meteorological measurement to a height of 100m, and then across to the urban area at constant height, as illustrated in Figure 1-2. The remaining sections of this chapter formulate the details of this procedure.

4.3 Estimating the velocity at the reference location from meteorological data

4.3.1 Step 1: Going up

Our goal is to calculate a wind speed estimate at a height of 100m in the open or rural site using the wind speed data at a height of 10m. While the aforementioned logarithmic relationships can only be applied down to a height of about $2.0H_r$ for urban and industrial sites, the presence of only few obstacles at the rural site allows us to apply the logarithmic laws down to the height of the weather station.

In Section 4.1, we explained the distinction between a neutral and a non-neutral ABL and presented their wind profile formulations. For the purposes of our work, we are particularly interested in situations with light winds, where the buoyancy-dominated regime of Figure 2-6 is a solution for buildings in dense urban areas. Under these light wind conditions, one might wonder whether the buoyant effects in the atmosphere need to be considered, that is whether the expression for a neutral boundary layer (Equation 4.8) or the more intricate expression for a non-neutral boundary layer (Equation 4.9) should be applied to determine the wind speed profile and the velocity at $z = 100$m. Hanna and Britter have argued that the boundary layer is typically nearly neutral at urban sites due to the strong mechanical turbulence that results in substantial surface drag and large values of the friction velocity [18]. However, this argument pertains to urban sites and at present we are interested in obtaining a wind speed estimate at a height of 100m over a rural site. For the boundary layer to be considered neutral up to this height and for Equation 4.8 to be a good approximation, the magnitude of the Monin-Obukhov length L given by Equation 4.1 needs to be larger than 100m. Using Equation 4.1 and assuming daytime conditions, we can calculate the friction velocity for $L = -100\text{m}$ with $T = 300\text{K}$, $H_s = 200\text{W/m}^2$, and standard values for the remaining constants and variables. This yields a u_* of 0.6m/s for the unstable boundary layer, which is a fairly large value within the range of typical values of 0.05-1m/s given by [18]. For light wind conditions over rural sites, u_* will likely not be this large, meaning the boundary layer would not be considered neutral up to this height and Equation 4.8 might not be a good approximation.

We can investigate how much a wind speed estimate calculated using the neutral logarithmic law deviates from the wind speed in the actual non-neutral boundary layer over a rural site by plotting and comparing the two wind speed profiles for plausible wind speed values at a height of 10m. L is a function of u_* (Equation 4.1) and u_* is a function of L, z, z_0, and u (Equation 4.9). For a given u at $z = 10\text{m}$, a z_0 value of 0.1m appropriate to a rural site, and T, H_s and the physical constants as in the previous example, we can combine the two equations to solve for both u_* and L and the unstable wind speed profile. For the neutral case, the calculation is fairly straightforward using Equation 4.8 and the same values for $u_{10\text{m}}$ and z_0. Table 4.1 summarizes the calculated u_* and L values and the wind speed profiles are shown in Figure 4-3 for $u_{10\text{m}}$ of 1m/s, 3m/s, 5m/s, and 7m/s. As expected, the wind speed profile of the non-neutral boundary layer has a more uniform and flatter profile due to the increased convective mixing during the daytime. This is also reflected in the larger u_* values in Table 4.1. The figure indicates a discrepancy

Table 4.1: Friction velocities u_* for a neutral and a non-neutral (unstable) boundary layer calculated from wind speed values at 10m height. Monin-Obukhov lengths L for the unstable case are also listed.

$u_{10\text{m}}$ (m/s)	u_*, neutral (m/s)	u_*, unstable (m/s)	L, unstable (m)
1	0.09	0.16	-1.84
3	0.26	0.32	-15.41
5	0.43	0.48	-50.96
7	0.61	0.64	-121.20

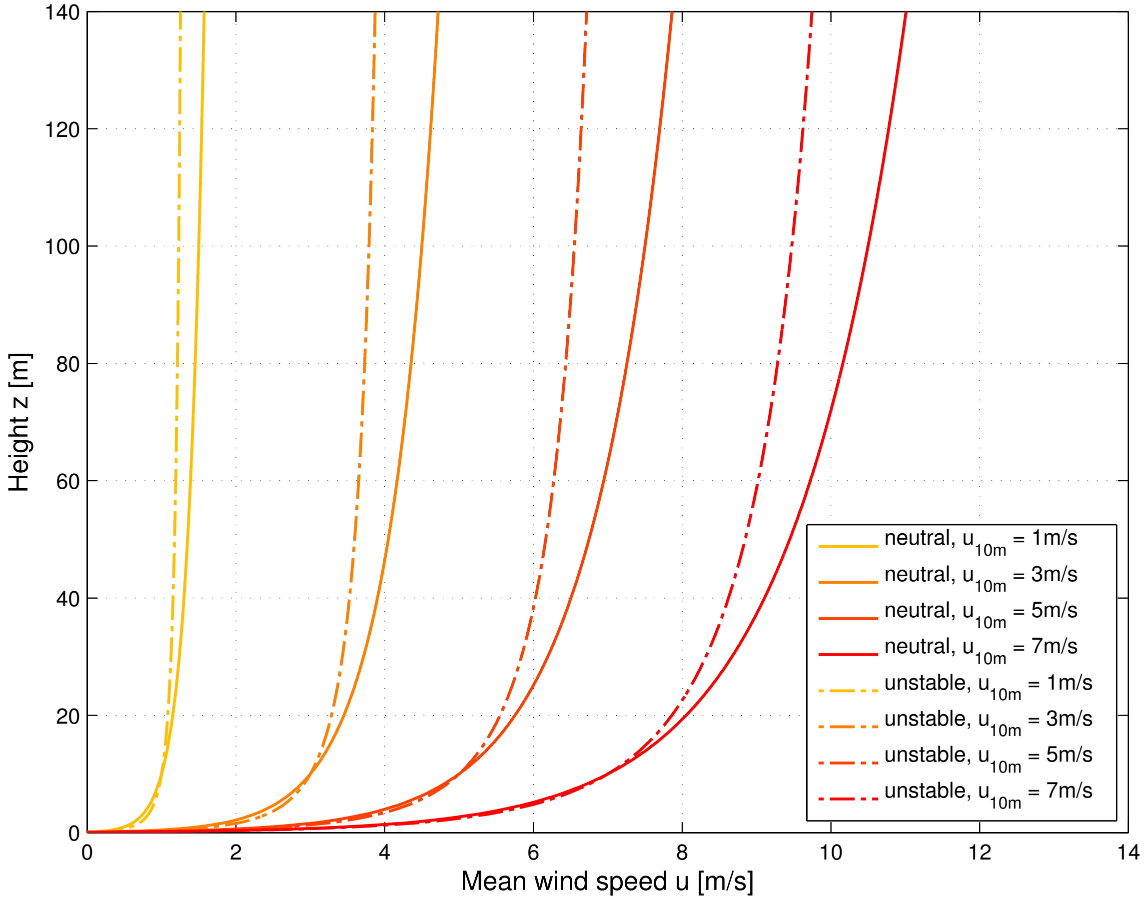

Figure 4-3: Daytime mean wind speed profiles for a neutral and a non-neutral (unstable) boundary layer calculated from wind speed values at 10m height.

of about 1m/s or less between the two profiles at z = 100m. To take a closer look at what is happening at z = 100m, we can plot the difference or absolute error $\Delta u_{100\mathrm{m}} = u_{100\mathrm{m},neutral} - u_{100\mathrm{m},non-neutral}$ as well as the normalized difference or relative error $\Delta u_{100\mathrm{m}}/u_{100\mathrm{m},non-neutral}$ as a function of L (Figure 4-4). We would expect that as L gets larger, the boundary layer becomes increasingly more neutral and the difference $\Delta u_{100\mathrm{m}}$ gets smaller. The curves in the above figure confirm this. We also see that the absolute error has a maximum value of about 1m/s while the relative error, the normalized difference, is no larger than about 20% even in very light winds and when the boundary layer is very non-neutral. The neutral logarithmic profile can thus adequately approximate the wind speed profile in a non-neutral boundary layer at a rural site, and we therefore recommend using the simpler Equation 4.8 instead of

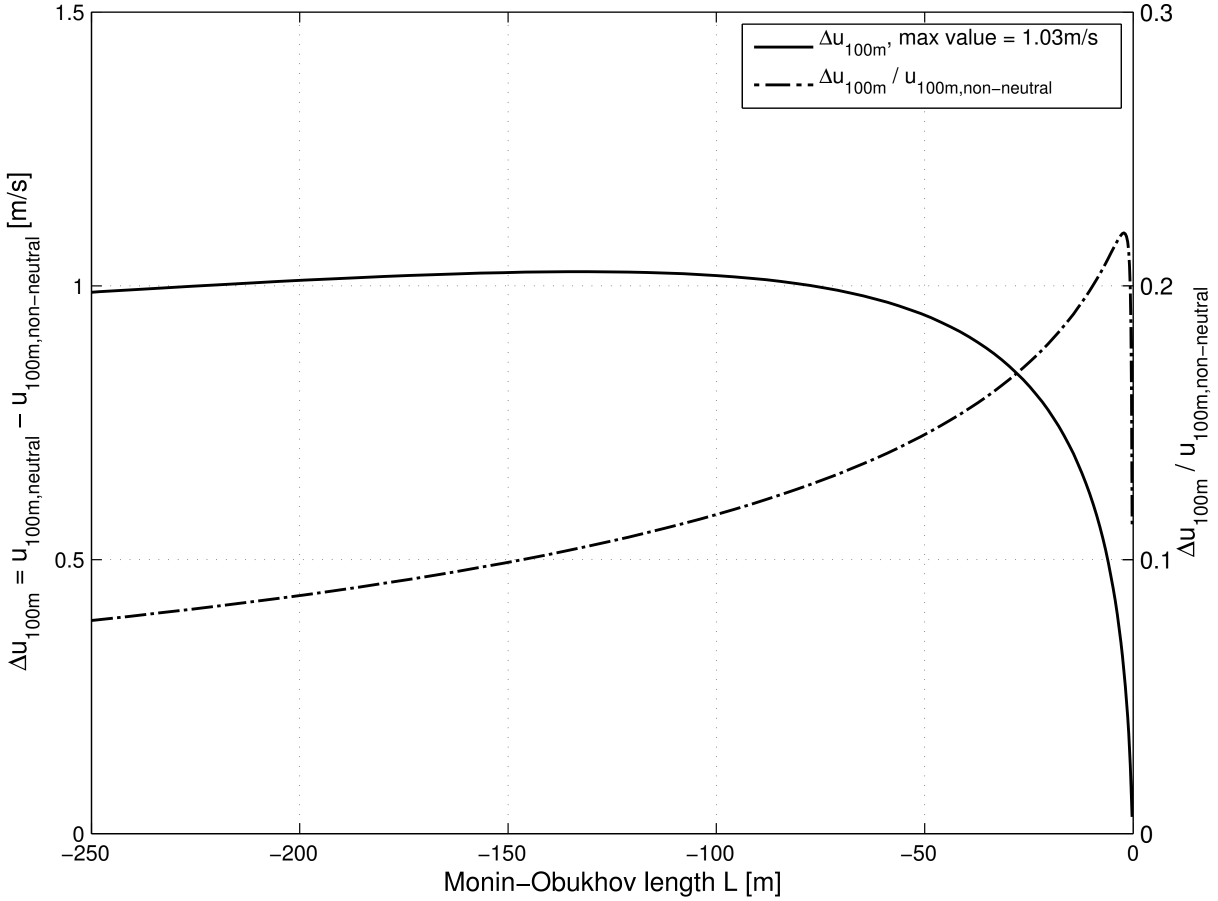

Figure 4-4: Difference between neutral and non-neutral wind speed estimates at a height of 100m and normalized difference, both as a function of L.

Equation 4.9 to estimate the wind speed at $z = 100$m from the meteorological data at $z = 10$m. For ease of application, Equation 4.8 can be simplified as follows:

$$\begin{aligned} u_{100m,rural} &= u_* \left[\frac{1}{\kappa} ln\left(\frac{100}{z_{0,rural}}\right)\right] \\ &= \left[\frac{\kappa u_{10m,rural}}{ln\left(10/z_{0,rural}\right)}\right]\left[\frac{1}{\kappa} ln\left(\frac{100}{z_{0,rural}}\right)\right] \qquad (4.10) \\ &= u_{10m,rural}\left[\frac{ln\left(100/z_{0,rural}\right)}{ln\left(10/z_{0,rural}\right)}\right] \end{aligned}$$

where a typical value of $z_{0,rural} = 0.1m$ gives

$$u_{100m,rural} = 1.5 u_{10m,rural} \qquad (4.11)$$

4.3.2 Step 2: Getting across

We need to be able to relate the wind speed estimate at $z = 100$m at the rural site, obtained using the method discussed in the previous section, to our chosen reference condition of $z = 100$m at the urban site. A straightforward, first-order approximation would be to assume the wind speeds to be equal at this height. Both intuitively and from simple physical arguments, we would expect the wind speeds at the two sites to be close in value at a height this far up. As pointed out in Section 4.1, the dominant effects of the ground surface and obstacles are felt in the roughness layer, below about $2.0H_r$. At the top of the surface layer around 50-100m or at most 200m for an urban area, the velocities, whether over a rural or urban site, all start approaching the same geostrophic or free stream wind speed. Hence, it seems reasonable to assume that the difference in wind speeds at a height of 100m would be small (R. Britter, personal communication, October 2011). We can also study Figure 4-5, which plots the wind speed profiles in a neutral boundary layer as a function of typical surface roughness lengths on a semi-log scale. If we compare the wind speeds at $z = 100$m for $z_0 = 1$m representative of an urban site and $z_0 = 0.1$m representative of a rural site, the difference is negligible. Hence, we will assume that the wind speeds above the rural and the urban site at a height of 100m are equal, an approximation that will likely suffice for our beginning design stage applications:

$$u_{100m,urban} = u_{100m,rural} = 1.5u_{10m,rural} \tag{4.12}$$

4.3.3 Logarithmic law vs. power law

Before concluding this chapter, it is important to mention that an alternate formulation to the logarithmic law exists for determining the wind speed profile in a boundary layer. While the logarithmic profile is well-established among climatologists, in the engineering community the power law is well-known and widely-used. The power law is not a law in the strictest sense; it does not have a physical basis but rather is a mathematical approximation of observed wind speed profiles [32]. In Section 3.2.2, we

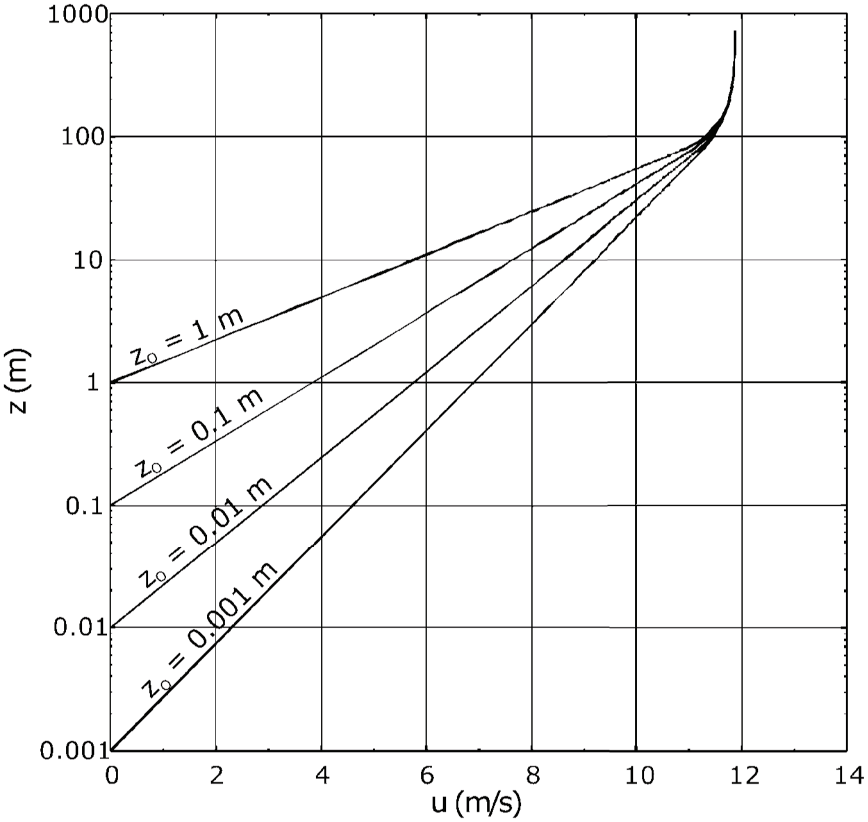

Figure 4-5: Wind speed profiles in a neutral atmospheric boundary layer for four typical surface roughness lengths. A constant free-stream or geostrophic wind speed is assumed at the top of the boundary layer, about 1000m above ground level [18].

made use of the power law to convert between reference velocities. As given by Equations 4.13 and 4.14, the power law can be applied across different terrain categories to determine the wind speed values at, say, an urban site using the meteorological data at a rural site [1]:

$$u(z) = u_G\left(\frac{z}{\delta}\right)^{\alpha} \tag{4.13}$$

where the free stream wind speed u_G is given by

$$u_G = u_{met}\left(\frac{\delta_{met}}{z_{met}}\right)^{\alpha_{met}} \tag{4.14}$$

α and δ denote the power law exponent and atmospheric boundary layer thickness, respectively, and both are a function of terrain category. Values for four different terrain categories are tabulated in [1]. From a single meteorological measurement,

u_{met} at z_{met}, the free stream wind speed u_G is calculated using appropriate boundary layer parameters α_{met} and δ_{met}. Once u_G is known, the wind speed profile $u(z)$ can be derived for any of the other terrain categories from Equation 4.13.

For a wind speed of 10m/s at $z = 100$m, we computed wind speed profiles based on the power law for three terrain or roughness categories, open, urban/suburban, and city center, using the boundary layer values listed in [1]. For the same wind speed at $z = 100$m and the same terrain categories, we also determined the wind speed profiles based on the neutral logarithmic law (Equation 4.2). Referencing data in [18], we assigned z_0 and d values to the different terrain categories: $z_0 = 0.1$m and $d = 0$ for open, $z_0 = 1$m and $d = 5$m for urban, and $z_0 = 2$m and $d = 10$m for city center. These values more or less correspond to categories of roughly open, very rough/skimming, and chaotic [18]. The profiles are shown in Figure 4-6. The curves suggest that the two laws do not differ much in their profiles, especially at higher elevations.

We also compared the approach of going up and getting across for estimating the wind speed at a height of 100m at an urban site (Sections 4.3.1 and 4.3.2) to the power law method. Assuming a meteorological measurement of 5m/s at $z = 10$m, the wind speed profiles for the three different terrain categories were computed first using the power law (Equations 4.13 and 4.14). These profiles were then compared to those obtained from applying steps 1 and 2 of Sections 4.3.1 and 4.3.2 to the same meteorological measurement of 5m/s at $z = 10$m. The resulting profiles are shown in Figure 4-7.

At $z = 100$m, the wind speed estimates from the power law are substantially lower than those obtained using the logarithmic approach, especially for the city center or chaotic terrain category. From Equation 4.13, we can see that the power law relies on an estimate of the free stream wind speed u_G to determine the wind speed profile $u(z)$. While this value is easily obtained from Equation 4.14, one might wonder how applicable the law is at the height of the boundary layer thickness, very far above the meteorological measurement. As pointed out in Section 4.2, in real urban areas additional thermal effects in the atmosphere tend to interfere with a clean estimate

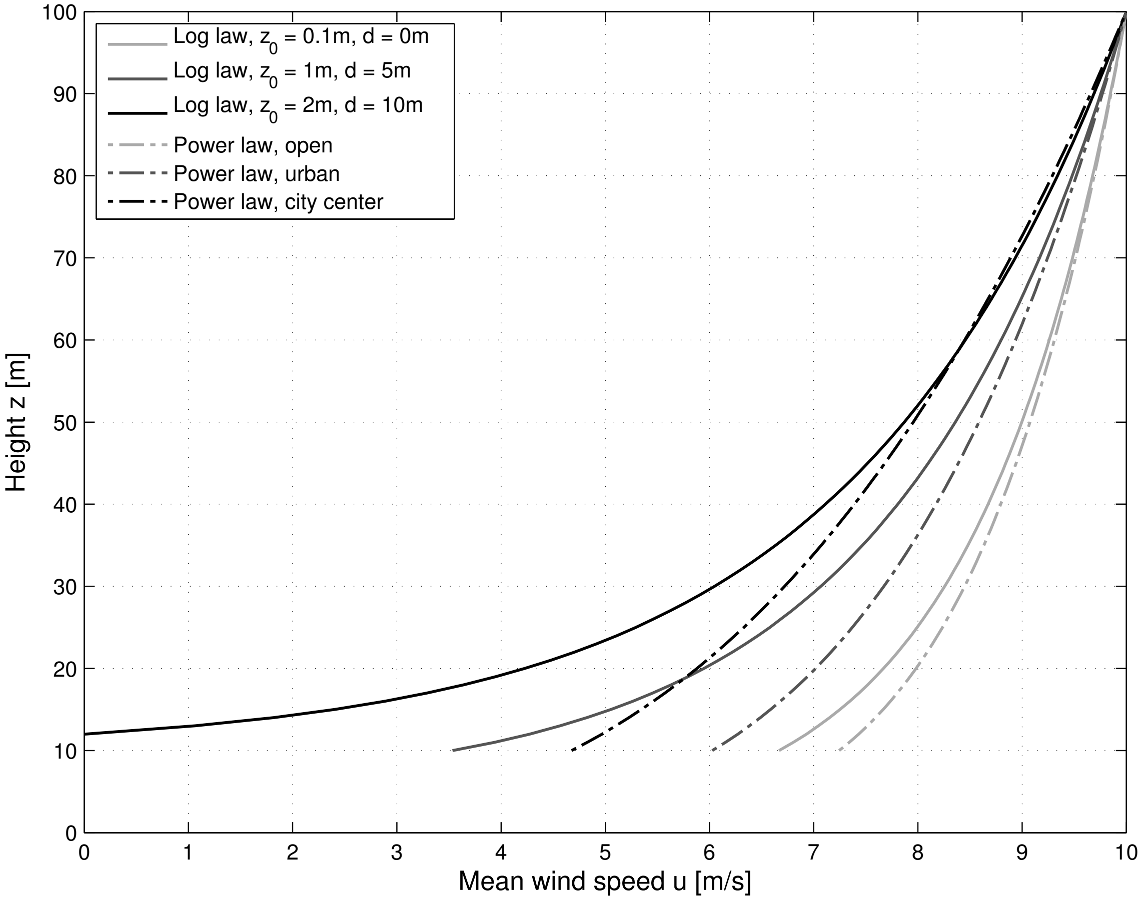

Figure 4-6: Wind speed profiles obtained from the neutral logarithmic law and the power law for three terrain categories. A wind speed of 10m/s at $z = 100$m was assumed for all cases.

of the free stream wind speed. It is unlikely that the power law approximation has been validated against empirical data for the entire depth of the ABL.

Still, many factors could be contributing to the discrepancy observed in Figure 4-7, and this area certainly deserves further research. For now, we recommend for designers to proceed with the logarithmic law to estimate wind speeds at the reference location. The logarithmic profile is valid within a limited region of the boundary layer, and there is some general agreement among climatologists as to what constitutes that region of applicability. Because of this, and because of its physical basis, the logarithmic law represents a more established and judicious method for determining the wind speed profile.

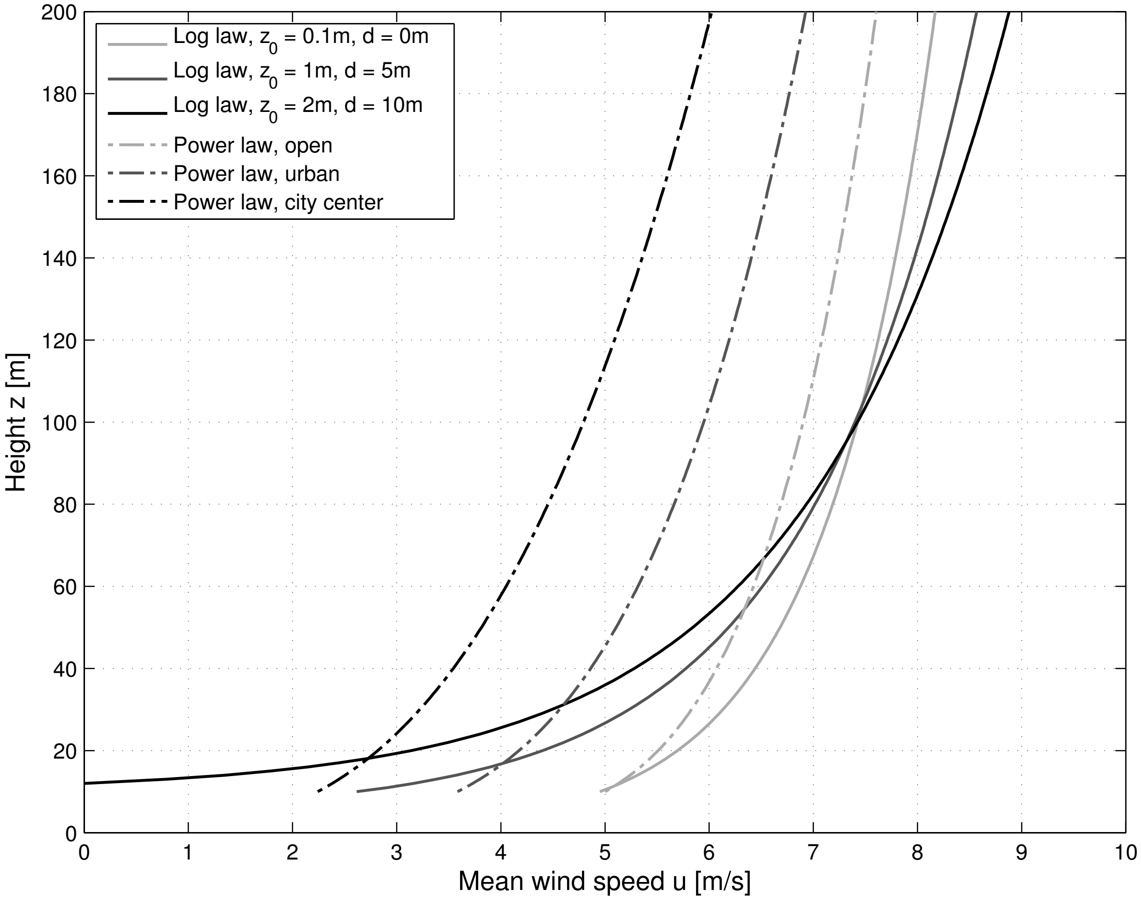

Figure 4-7: Wind speed profiles obtained from the neutral logarithmic law and assuming a constant wind speed at a height of 100m compared to profiles obtained from the power law, for three terrain categories. A meteorological measurement of 5m/s at $z = 10$m was assumed for all cases.

Chapter 5

Summary and recommendations for future research

5.1 Summary of basic procedure

The main motivation behind this work was to obtain a better understanding of how a building's natural ventilation potential is affected by the complexities introduced by the urban environment. To this end, we have derived in detail the physical principles of wind- and buoyancy-driven natural ventilation for a standard apartment geometry, documented and analyzed the existing data on wind pressure coefficients, and examined the flow in the urban boundary layer and how it relates to the boundary layer over a rural site.

The information and understanding that emerged from this research has been assembled into a set of graphical methods and simple guidelines that can be applied by designers to the early design phases of natural ventilation projects in urban areas. These methods can be used to estimate indoor-outdoor temperature differences and airflow rates for several opening geometries. The procedure is as follows, with the graphical methods consolidated at the end of this chapter:

1. Calculate λ parameters or make use of land use class approximations to estimate wind pressure coefficient difference (Figure 5-1).

2. From a meteorological measurement, determine the wind speed at the reference location of $z = 100\text{m}$ above the urban surface by assuming a neutral logarithmic wind speed profile to go up at the rural site and a constant wind speed at 100m height to get across:

$$u_{100m,urban} = u_{100m,rural} = 1.5u_{10m,rural}$$

3. Approximate building heat gains from canyon aspect ratio (Figure 5-2).
4. Using the computed wind speed, heat gain, and wind pressure coefficient difference values, estimate the indoor-outdoor temperature difference (Figure 5-3) and/or volumetric airflow rate in air changes per hour (Figure 5-4). Account for uncertainties in inputs and provide conservative estimates as necessary.
5. The temperature difference can be used with a site-corrected outdoor temperature to obtain a thermal comfort prediction for evaluating the feasibility and potential of the natural ventilation strategy.

Our hope is for these methods to offer a good overview of how natural ventilation calculations can be applied to urban areas and to help resolve some of the main difficulties that a designer might encounter during this process. While the approach is primarily intended to inform decision-making during the beginning design stages, we imagine that, from applying it, designers will also acquire a more physical and intuitive understanding of how the forces of natural ventilation are altered in progressively denser urban sites and that this could also aid in the interpretation of results at the simulation stage.

5.2 Summary of design implications

Figure 5-3 illustrates the three flow regimes applicable to the naturally ventilated geometry considered. We can summarize the main features of each flow regime and include recommendations for estimating the indoor-outdoor temperature difference:

- When the building is relatively isolated from surrounding obstacles, the wind pressure coefficient differences are of order 1. For this case, the flow is dominantly wind-driven, the natural ventilation potential is high, and the indoor temperatures can be estimated by the outdoor temperatures.

- For dense urban areas in light winds, or for typical urban areas under conditions when the wind incident angle is *not* normal to the windward facade or there is high uncertainty in the inputs, the wind pressure coefficient differences are very small, of order 10^{-3}. The flow is then dominantly buoyancy-driven, and the indoor-outdoor temperature difference approaches a constant value; this upper bound can be calculated from knowledge of the heat gains and opening height.

- For typical urban areas in North America under conditions when the wind incident angle is normal to the windward facade, the flow is in-between these extremes, driven by both wind and buoyancy forces. For this case, it has been shown that the indoor-outdoor temperature difference can be approximated by a purely wind-driven calculation.

It is essential for a designer to recognize what flow regime is relevant to his or her project. For a geometry with a standard opening height of 0.75m (Figure 5-3b), the difference between a wind-dominated and a buoyancy-dominated regime is about 2.2K (4°F). This is a very large difference in temperature prediction, one that could easily alter the thermal comfort outcome.

The flow regime classification leads to an important conclusion, that buoyancy-driven bidirectional flow contributes tremendously to the feasibility of natural ventilation of buildings in dense urban areas. Buoyancy effects can reduce the indoor temperatures by several degrees centigrade and thereby provide a considerable amount of space cooling in urban areas where the potential for wind-driven ventilation is very low. This is convenient particularly because airflow patterns in dense urban areas are complex and a challenge to predict, so if natural ventilation is generated primarily by buoyancy effects in these dense urban areas, much of the complexity can be stripped away. The analysis is then considerably simplified, since a readily computed upper bound to the indoor-outdoor temperature difference can provide designers with a reasonable first-order estimate of thermal comfort.

Because of the central role that buoyancy-driven ventilation plays in dense urban areas, the window opening height becomes a key architectural feature that a designer can control to enhance the natural ventilation potential of a space. It would be advantageous to implement openings that are more vertical rather than horizontal in configuration. This could be achieved by simply increasing the height of the opening or by using two openings, one located at the very bottom and one at the very top of each facade, where the increased separation distance between the two openings promotes the buoyantly-driven flow.

5.3 Recommendations for future research

We conclude with some recommendations and ideas for future research. It is necessary to further assess and validate the results of this work using experiments and/or detailed simulations. In particular, studies modeling an actual naturally ventilated building within an array of obstacles could be very useful for understanding the connection between the interior and the exterior flow. These studies could help evaluate the assumption of parallel streamlines at the opening used in the derivation of Chapter 2. More work needs to be done to understand the energy losses that the flow incurs as it passes through the opening and separates, especially how well a single value of the discharge coefficient can approximate these losses. High-resolution time-dependent CFD simulations are needed to assess the magnitudes of turbulent fluctuations in dense urban areas and how they compare to the time-averaged wind and buoyancy driving forces for natural ventilation.

As seen in Chapter 3, fairly limited data is available on surface wind pressure coefficients for building arrays, and nearly none for groups of buildings that more closely resemble real urban sites characterized by large variations in building size and shape. Morphological data on real cities is scarce, particularly planar and frontal area densities for European and Asian cities. More generally, further research is also needed to understand how well pressure coefficients obtained from wind tunnel experiments of closed buildings with solid surfaces can extend to actual buildings with openings.

The relationship between the urban and rural wind speed profiles has been much discussed and debated by the author and her colleagues. Simulations of the atmospheric boundary layer over rural and urban sites could be very helpful in clarifying this relationship in addition to other conclusions of Chapter 4, such as how well the power law and the logarithmic law (both neutral and non-neutral) can estimate the wind speed profile.

An important question that arises, and that deserves much further study, is to what accuracy can a program or a set of methods incorporate the complex airflow patterns and many uncertainties of urban areas to predict the indoor temperatures of naturally ventilated spaces and equally importantly, whether that accuracy is necessary. Simulating the details of the turbulent flow in the urban canopy layer could quickly exhaust current computational capabilities, and even for models that only attempt to provide wind speed estimates within the canyon, the question still remains as to whether that level of detail is necessary for thermal comfort purposes. While incorporating greater detail can yield a prediction that is precise for a certain deterministic state of the input values, given the fluctuations and uncertainties of the urban flow field, this prediction might not be accurate or even useful. Hence, the question brings up the point whether providing less precise, but more robust design predictions, that can accommodate some of the uncertainties and are of appropriate (thermal-comfort-defined) accuracy, is a better approach for tackling the problem of natural ventilation in urban areas. This was the approach taken in this work, by differentiating between order-of-magnitude wind pressure coefficient differences to estimate indoor temperatures, and by stressing the importance of the upper temperature bound in the buoyancy-dominated regime as an example of a robust design prediction that can better accomodate the complexities and uncertainties of the urban flow field.

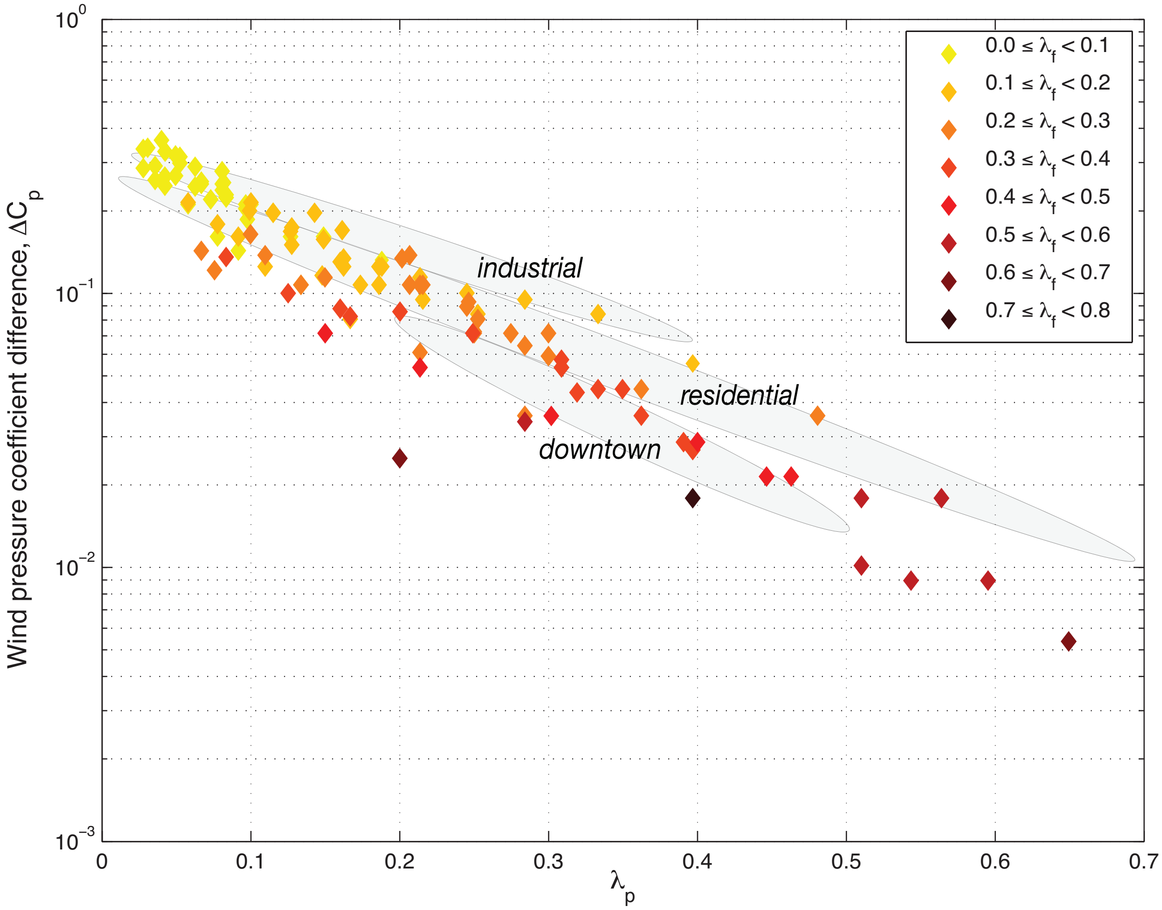

Figure 5-1: Surface-averaged wind pressure coefficient differences as a function of λ_p and λ_f with land use class data from real cities superimposed.

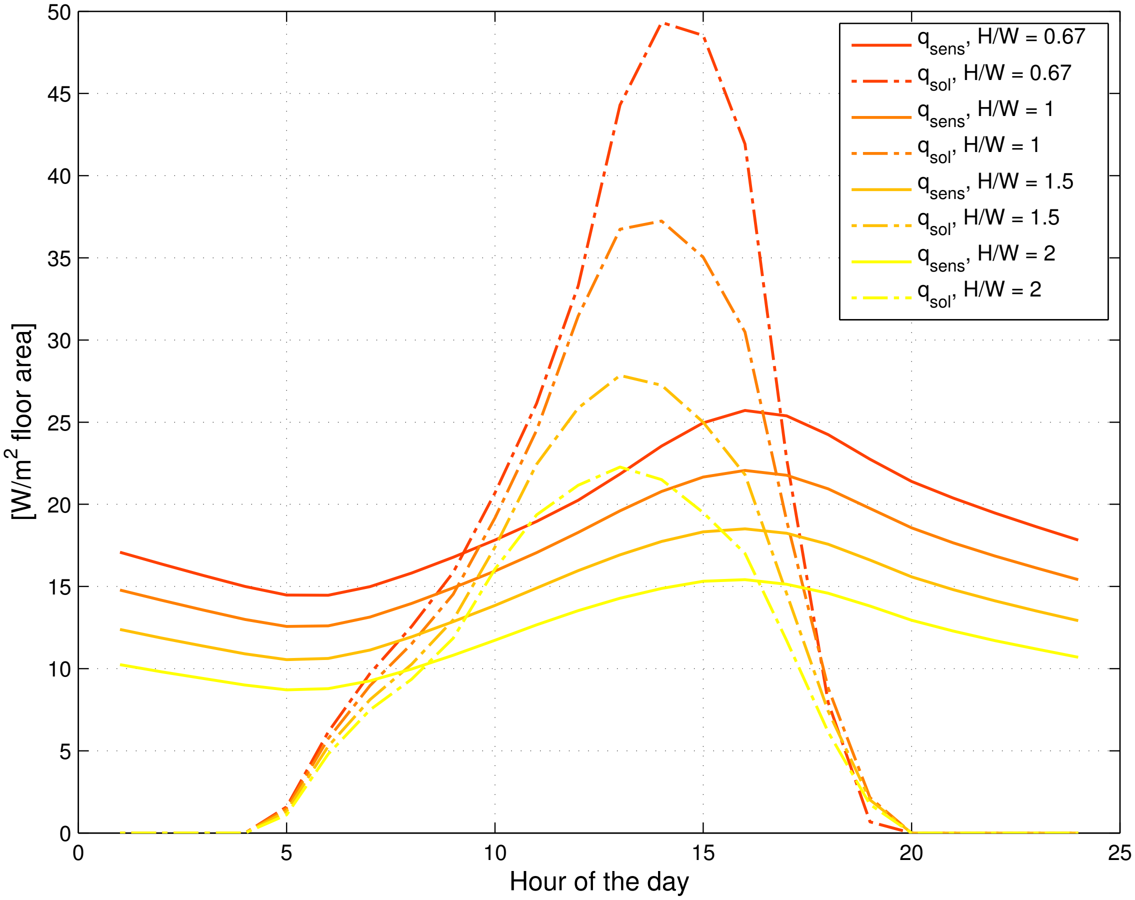

Figure 5-2: Heat gain density profiles for various canyon aspect ratios.

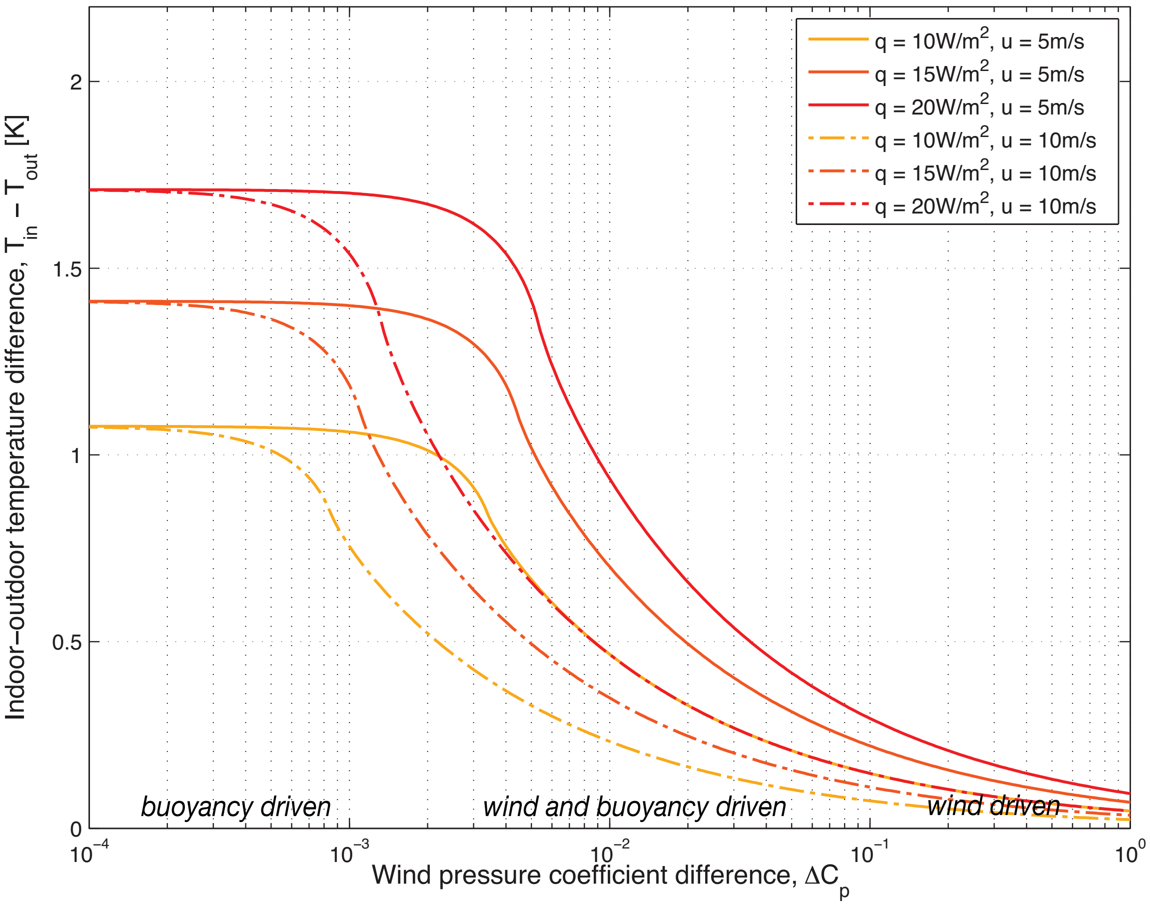

(a) Geometry with opening height h = 1.5m.

Figure 5-3: Indoor-outdoor temperature difference as a function of wind pressure coefficient difference. q is the zone heat gain density and u is the wind speed measured at a location that matches the reference condition of the pressure coefficient.

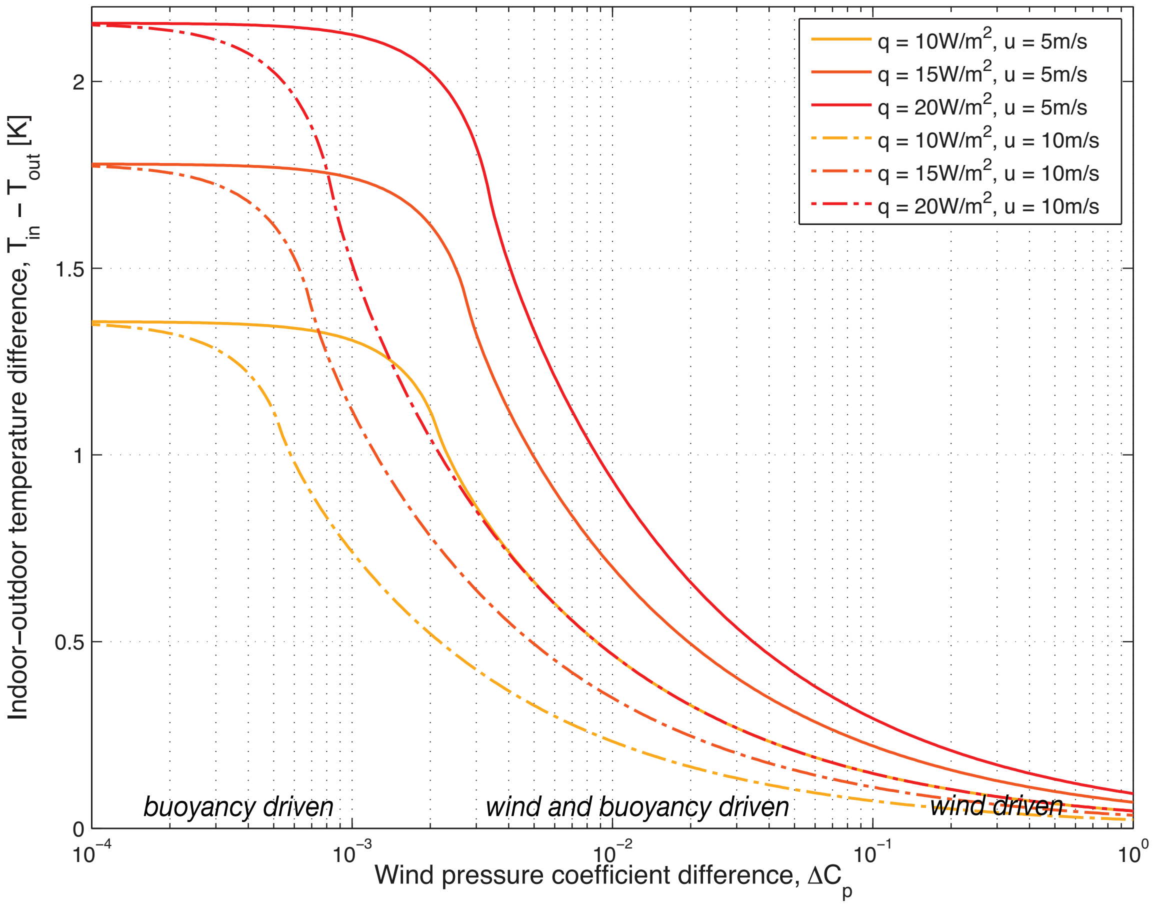

(b) Geometry with opening height h = 0.75m.

Figure 5-3: Indoor-outdoor temperature difference as a function of wind pressure coefficient difference. q is the zone heat gain density and u is the wind speed measured at a location that matches the reference condition of the pressure coefficient.

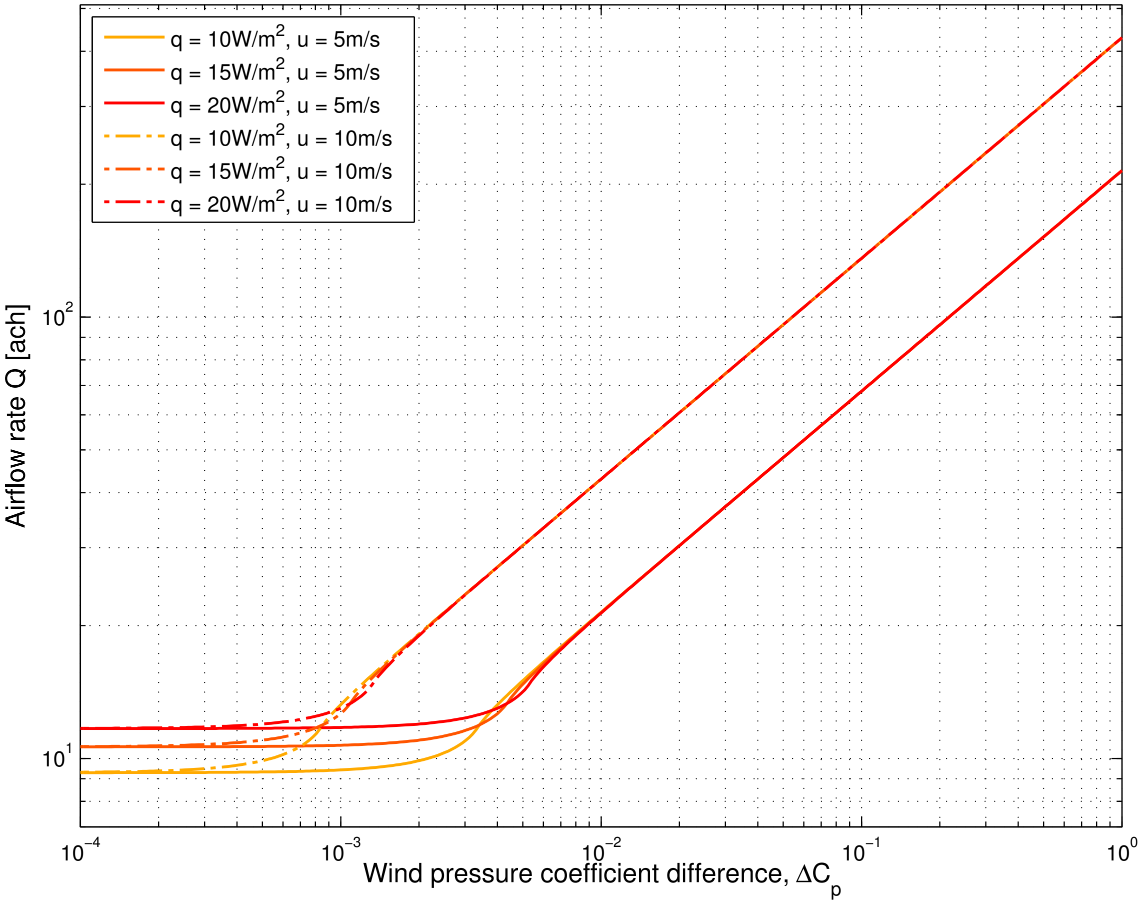

(a) Geometry with opening height h = 1.5m.

Figure 5-4: Airflow rate as a function of wind pressure coefficient difference. q is the zone heat gain density and u is the wind speed measured at a location that matches the reference condition of the pressure coefficient.

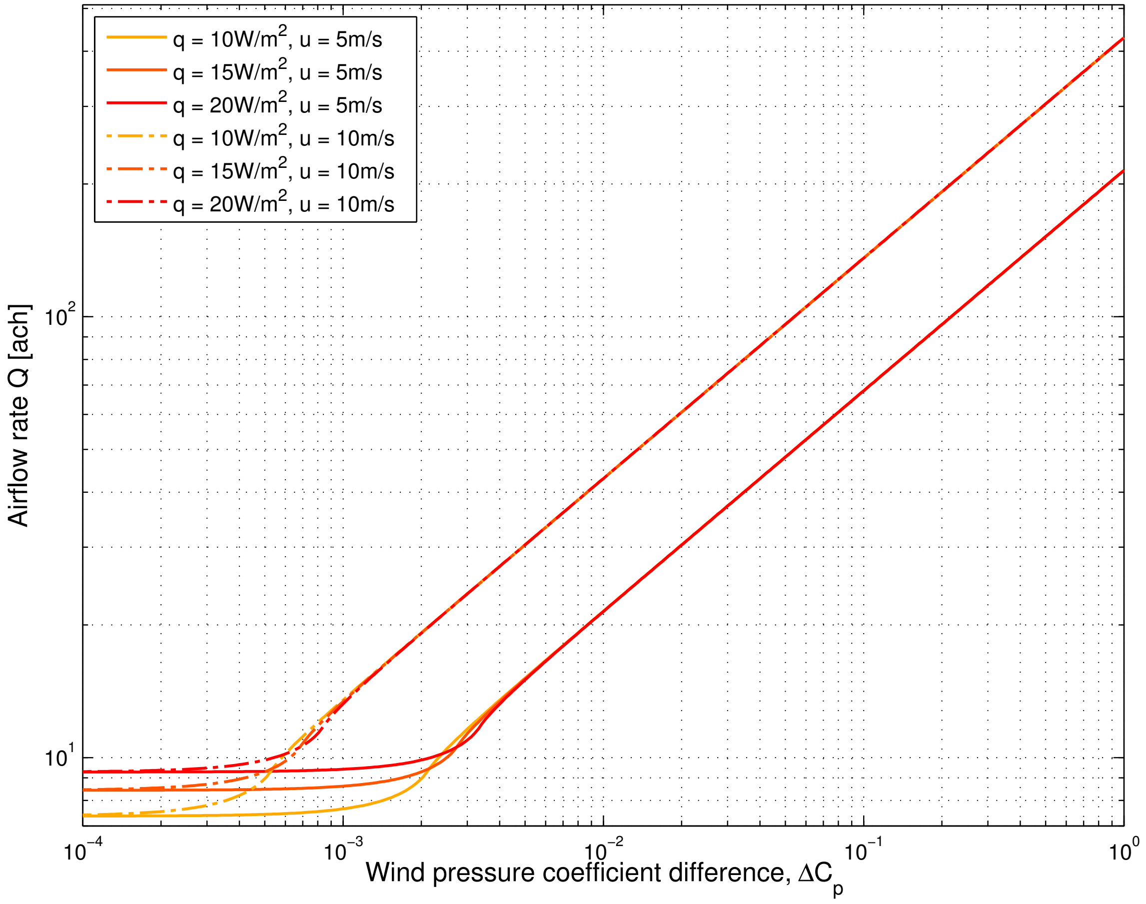

(b) Geometry with opening height h = 0.75m.

Figure 5-4: Airflow rate as a function of wind pressure coefficient difference. q is the zone heat gain density and u is the wind speed measured at a location that matches the reference condition of the pressure coefficient.

Appendix A

λ_p and λ_f values

[1] These values are averages over four wind directions (N, NE, E, SE).

[2] These values are averages over all wind directions.

[3] As cited in [5].

Table A.1: Plan area density λ_p and frontal area density λ_f for 36 cities in North America, Europe, and Mexico.

Location	Land use class	λ_p	λ_f	Source
Albuquerque, NM	Industrial	0.29	0.08 [1]	Burian et al. (2003a)[3]
Houston, TX	Industrial	0.17	0.04 [1]	Burian et al. (2003b)[3]
Los Angeles, CA	Industrial	0.38	0.10 [1]	Burian et al. (2002b)[3]
Oklahoma City, OK	Industrial	0.10	0.02 [1]	[5]
Phoenix, AZ	Industrial	0.19	0.05 [1]	Burian et al. (2002c)[3]
Portland, OR	Industrial	0.31	0.08 [1]	Burian et al. (2002d)[3]
Salt Lake City, UT	Industrial	0.27	0.15 [1]	Burian et al. (2002e)[3]
Vancouver, Canada	Light Industrial	0.38	0.13	Voogt and Oke (1997)[3]
Arcadia, CA	Suburban residential	0.53	0.33	Grimmond and Oke (1999)[3]
Chicago, IL	Suburban residential	0.38	0.21	Grimmond and Oke (1999)[3]
Chicago, IL	Suburban residential	0.47	0.28	Grimmond and Oke (1999)[3]
Miami, FL	Suburban residential	0.35	0.16	Grimmond and Oke (1999)[3]
Sacramento, CA	Suburban residential	0.58	0.23	Grimmond and Oke (1999)[3]
San Gabriel, CA	Suburban residential	0.36	0.14	Grimmond and Oke (1999)[3]
Tucson, AZ	Suburban residential	0.33	0.19	Grimmond and Oke (1999)[3]
Vancouver, Canada	Suburban residential	0.62	0.19	Voogt and Oke (1997)[3]
Oklahoma City, OK	Single-family residential	0.07	0.04 [1]	[5]
Portland, OR	Multifamily residential	0.26	0.17 [1]	Burian et al. (2002d)[3]
Albuquerque, NM	High-density residential	0.19	0.09 [1]	Burian et al. (2003a)[3]
Houston, TX	High-density residential	0.17	0.09 [1]	Burian et al. (2003b)[3]
Los Angeles, CA	High-density residential	0.27	0.12 [1]	Burian et al. (2002b)[3]
Albuquerque, NM	Downtown core area	0.30	0.20 [1]	Burian et al. (2003a)[3]
Houston, TX	Downtown core area	0.27	0.22 [1]	Burian et al. (2003b)[3]
Los Angeles, CA	Downtown core area	0.29	0.38 [1]	Burian et al. (2002b)[3]
Oklahoma City, OK	Downtown core area	0.35	0.19 [1]	[5]
Phoenix, AZ	Downtown core area	0.32	0.23 [1]	Burian et al. (2002c)[3]
Portland, OR	Downtown core area	0.34	0.22 [1]	Burian et al. (2002d)[3]
Berlin, Germany	Downtown/Central city	0.35	0.23 [2]	[24]
Leece, Italy	Downtown/Central city	∼0.4	∼0.5 [2]	[9]
London, England	Downtown/Central city	0.55	0.32 [2]	[24]
Los Angeles, CA	Downtown/Central city	0.28	0.38 [2]	[24]
Mexico City, Mexico	Downtown/Central city	0.47	0.19	Grimmond and Oke (1999)[3]
Salt Lake City, UT	Downtown/Central city	0.22	0.11 [2]	[24]
Toulouse, France	Downtown/Central city	0.4	0.32 [2]	[24]
Vancouver, Canada	Downtown/Central city	0.37	0.3	Voogt and Oke (1997)[3]
Los Angeles, CA	Urban high-rise	0.32	0.45 [1]	Burian et al. (2002b)[3]

Appendix B

MATLAB script

```
function [delT,Q] = plotdelTandQ(minCp,maxCp,nCp,h,u,q,Cd,A,rho,Aflr)

% This function calculates the indoor—outdoor temperature difference for
% combined wind and buoyancy forcing for a simple cross—ventilated
% geometry with two windows of equal area placed on opposite walls at
% equal heights above the floor.

% For the function to run, the file calcdelTandQ.m needs to be placed
% in the same folder as this file.

% Two plots are generated:
% 1. Indoor—outdoor temperature difference as a function of wind
%    pressure coefficient difference (semilogx).
% 2. Airflow rate as a function of wind pressure coefficient difference
%    (loglog).

% Since the wind pressure coefficient difference is plotted
% logarithmically, the function will sample these values exponentially
% for efficient computation.  To do this, the following inputs are
% needed:
% minCp     smallest value of the wind pressure coefficient difference
%           used in the calculations
```

```
% maxCp     largest value of the wind pressure coefficient difference
%           used in the calculations
% nCp       number of sample points

% Other (physical) inputs:
% h         operable height of the opening (m)
% u         wind speed measured at a location that matches the reference
%           condition of the pressure coefficient (m/s), can be a vector
%           of up to two entries, e.g. [5 10]
% q         zone heat gain density (W/m^2), can be a vector
% Cd        discharge coefficient, typically 0.6 for sharp-edged openings
% A         operable area of the opening, m^2
% rho       density of air, kg/m^3
% Aflr      zone floor area, m^2

% Outputs:
% delT      indoor-outdoor temperature difference (K)
% Q         airflow rate (ach)

% A few examples:
% [delT,Q] = plotdelTandQ(1e-4,1,300,1.50,[5 10],[400 600 800],0.6,...
%            3.375,1.2,40);
% [delT,Q] = plotdelTandQ(1e-4,1,300,0.75,[5 10],[400 600 800],0.6,...
%            3.375,1.2,40);



% For more information, please refer to P. Truong, Recommendations for
% the analysis and design of naturally ventilated buildings in urban
% areas. Thesis (S.M. in Building Technology), Massachusetts Institute
% of Technology, Dept. of Architecture, 2012.

% Author:  Phan Truong, ptruong@mit.edu
% Last updated:  January 18, 2012

%%%%%%%%%%%%%%%%%%%%%%%%%%%%%%%%%%%%%%%%%%%%%%%%%%%%%%%%%%%%%%%%%%%%%%%%%%
```

```
close all;

% samples wind pressure coefficient difference values exponentially
delCp = minCp*(maxCp/minCp).^((0:nCp)/nCp);

% since the dependence of the indoor temperature on the outdoor
% temperature is negligible for Tout values typically encountered in
% natural ventilation (¬10−30 deg C), the Tout value is preset to a value
% of 300K
Tout = 300; % outdoor temperature (K)

%% plot delT vs. delCp (semilogx)
cmap = colormap(autumn(length(q)+1));
subplot(2,1,1);
for i = 1:length(u),
    for j = 1:length(q),
        [delT,Q] = calcdelTandQ(h,u(i),q(j),Cd,A,rho,Aflr,delCp,Tout);
        p(i,j) = semilogx(delCp,delT);
        if i == 2,
            set(p(i,j),'Color',cmap(length(q)+1−j,:),'LineStyle','−.',...
                'LineWidth',1.2);
        else
            set(p(i,j),'Color',cmap(length(q)+1−j,:),'LineStyle','−',...
                'LineWidth',1.2);
        end
        hold on;
    end
end

% formatting
grid on;axis tight;
set(gca,'FontSize',13,'FontName','Helvetica');
xlabel('\DeltaC_p','FontSize',15,'FontName','Helvetica');
ylabel('T_{in} − T_{out} (K)','FontSize',15,'FontName','Helvetica');
t = title(sprintf(['Indoor−outdoor temperature difference as a '...
    'function of wind pressure coefficient difference (A = %3.2fm2, '...
```

```
    'h = %3.2fm)'],A,h));
set(t,'FontSize',15,'FontName','Helvetica');

for i = 1:length(u),
    for j = 1:length(q),
    str{i,j} = sprintf('q = %dW/m^2, u = %dm/s',q(j)/Aflr,u(i));
    end
end
if length(u) == 2,
    h_legend = legend([str(1,:) str(2,:)],'Location','NorthEast');
else
    h_legend = legend(str,'Location','NorthEast');
end
set(h_legend,'FontSize',13,'FontName','Helvetica');

set(gcf,'Color','w');

%% plot Q vs. delCp (loglog)
subplot(2,1,2);
for i = 1:length(u),
    for j = 1:length(q),
        [delT,Q] = calcdelTandQ(h,u(i),q(j),Cd,A,rho,Aflr,delCp,Tout);
        r(i,j) = loglog(delCp,Q,'LineWidth',1.2,'Color','k');
        if i == 2,
            set(r(i,j),'Color',cmap(length(q)+1-j,:),'LineStyle','-.',...
                'LineWidth',1.2);
        else
            set(r(i,j),'Color',cmap(length(q)+1-j,:),'LineStyle','-',...
                'LineWidth',1.2);
        end
        hold on;
    end
end

% formatting
grid on;axis tight;
```

```
set(gca,'FontSize',13,'FontName','Helvetica');
xlabel('\DeltaC_p','FontSize',15,'FontName','Helvetica');
ylabel('Q (ach)','FontSize',15,'FontName','Helvetica');
t = title(sprintf(['Airflow rate as a function of wind pressure '...
    'coefficient difference (A = %3.2fm2, h = %3.2fm)'],A,h));
set(t,'FontSize',15,'FontName','Helvetica');

for i = 1:length(u),
    for j = 1:length(q),
    str{i,j} = sprintf('q = %dW/m^2, u = %dm/s',q(j)/Aflr,u(i));
    end
end
if length(u) == 2,
    h_legend = legend([str(1,:) str(2,:)],'Location','NorthWest');
else
    h_legend = legend(str,'Location','NorthEast');
end
set(h_legend,'FontSize',13,'FontName','Helvetica');

set(gcf,'Color','w');

end
```

```
function [delT,Q] = calcdelTandQ(h,u,q,Cd,A,rho,Aflr,delCp,Tout)

%% initialize variables
V    = Aflr*3; % calculate zone volume
eps  = 0.00001; % initial guess for Tin = Tout + eps
Tin1 = [];
Q1   = [];
Tin2 = [];
Q2   = [];

%% compute values for 0 < hnw,hnl < h

```

```
% indoor temperature Tin (K)
% solve nonlinear equation for Tin using delCp values
for i = 1:length(delCp),
    fh1 = @(Tin) q - (rho*1000*(A/h)*(1/3)*(2^(3/2))*Cd*((9.8*(Tin-...
        Tout)/Tin)^(1/2)) * ((0.5*(h+(Tin/(9.8*(Tin-Tout))*(0.5*u^2*...
        delCp(i)))))^(3/2) + (h-(0.5*(h+(Tin/(9.8*(Tin-Tout))*(0.5*...
        u^2*delCp(i))))))^(3/2)) * (Tin-Tout));
    Tin1(end+1) = fsolve(fh1,Tout+eps);
end
% remove imaginary Tin values from Tin1 (keep Tin for 0 < hnw,hnl < h)
C = imag(Tin1); % find complex parts of Tin values
keep = abs(C) < 0.0000001; % keep Tin with complex parts < 0.0000001
Tin1 = real(Tin1(keep)); % removing the very small complex part
delT1 = Tin1-Tout; % ∆ T values for 0 < hnw,hnl < h

% airflow rate Q (ach)
for i = 1:length(Tin1),
    Q1(end+1) = (A/h)*(1/3)*(2^(3/2))*Cd*((9.8*(Tin1(i)-Tout)/Tin1(i))...
        ^(1/2)) * ((0.5 * (h + (Tin1(i)/(9.8*(Tin1(i)-Tout))*(0.5*u^2*...
        delCp(i)))))^(3/2) + (h-(0.5*(h+(Tin1(i)/(9.8*(Tin1(i)-Tout))*...
        (0.5*u^2*delCp(i))))))^(3/2));
end
Q1 = Q1*3600/V; % convert to air changes/hour

%% compute values for hnw > h

% indoor temperature Tin (K)
% solve nonlinear equation for Tin using the remaining delCp values
delCp1 = delCp(keep);
for i = (length(delCp1)+1):length(delCp),
    fh2 = @(Tin) q - (rho*1000*(A/h)*(1/3)*(2^(3/2))*(-1)*Cd*((9.8*...
        (Tin-Tout)/Tin)^(1/2)) * (((0.5*(h+(Tin/(9.8*(Tin-Tout))*(0.5*...
        u^2*delCp(i)))))-h)^(3/2) - (0.5*(h+(Tin/(9.8*(Tin-Tout))*...
        (0.5*u^2*delCp(i)))))^(3/2)) * (Tin-Tout));
    Tin2(end+1) = fsolve(fh2,Tout+eps);
end
```

```
delT2 = Tin2-Tout; % Δ T values for hnw > h

% airflow rate Q (ach)
for i = 1:length(Tin2),
    Q2(end+1) = (A/h)*(1/3)*(2^(3/2))*(-1)*Cd*((9.8*(Tin2(i)-Tout)/...
        Tin2(i))^(1/2)) * (((0.5 * (h+(Tin2(i)/(9.8*(Tin2(i)-Tout))*...
        (0.5*u^2*delCp(length(delCp1)+i)))))-h)^(3/2) - (0.5*(h+(...
        Tin2(i)/(9.8*(Tin2(i)-Tout))*(0.5*u^2*delCp(length(delCp1)+i)...
        ))))^(3/2));
end
Q2 = Q2*3600/V; % convert to air changes/hour

%% combining the two sets of values
Tin  = [Tin1 Tin2];
delT = [delT1 delT2];
Q    = [Q1 Q2];

end
```

Bibliography

[1] *Handbook of Fundamentals*. American Society of Heating, Air-Conditioning and Refrigeration Engineers, Atlanta, 2009.

[2] F. Allard and M. Santamouris. *Natural ventilation in buildings: A design handbook*. Earthscan/James & James, 1998.

[3] R.E. Britter and S.R. Hanna. Flow and dispersion in urban areas. *Annual Review of Fluid Mechanics*, 35(1):469–496, 2003.

[4] B. Bueno Unzeta. An urban weather generator coupling a building simulation program with an urban canopy model. Thesis (S.M. in Building Technology), Massachusetts Institute of Technology, Dept. of Architecture, 2010.

[5] S.J. Burian, W.S. Han, and M.J. Brown. Morphological analyses using 3D building databases: Oklahoma City, Oklahoma. Technical report, LA-UR-05-1821, Los Alamos National Laboratory, Los Alamos, New Mexico, 2005.

[6] J. O. P. Cheung and C. H. Liu. CFD simulations of natural ventilation behaviour in high-rise buildings in regular and staggered arrangements at various spacings. *Energy and Buildings*, 43(5):1149–1158, 2011.

[7] D. Costola, B. Blocken, and J.L.M. Hensen. Overview of pressure coefficient data in building energy simulation and airflow network programs. *Building and Environment*, 44(10):2027–2036, 2009.

[8] S.B. Dalziel and G.F. Lane-Serff. The hydraulics of doorway exchange flows. *Building and Environment*, 26(2):121–135, 1991.

[9] S. Di Sabatino, L.S. Leo, R. Cataldo, C. Ratti, and R.E. Britter. Construction of digital elevation models for a Southern European city and a comparative morphological analysis with respect to Northern European and North American cities. *Journal of Applied Meteorology and Climatology*, 49(7):1377–1396, 2010.

[10] D.W. Etheridge and M. Sandberg. *Building ventilation: Theory and measurement*. John Wiley and Sons Chichester, 1996.

[11] United Nations Population Fund. UNFPA State of world population, 2011. Technical report, Information and External Relations Division of UNFPA, 2011.

[12] C. Georgakis and M. Santamouris. Experimental investigation of air flow and temperature distribution in deep urban canyons for natural ventilation purposes. *Energy and Buildings*, 38(4):367–376, 2006.

[13] C. Georgakis and M. Santamouris. On the estimation of wind speed in urban canyons for ventilation purposes, Part 1: Coupling between the undisturbed wind speed and the canyon wind. *Building and Environment*, 43(8):1404–1410, 2008.

[14] M. Germano, C. Ghiaus, C.A. Roulet, and F. Allard. Natural ventilation potential of urban buildings. *International Journal of Ventilation*, 4:49–56, 2005.

[15] V. Geros, M. Santamouris, S. Karatasou, A. Tsangrassoulis, and N. Papanikolaou. On the cooling potential of night ventilation techniques in the urban environment. *Energy and Buildings*, 37(3):243–257, 2005.

[16] C. Ghiaus, F. Allard, M. Santamouris, C. Georgakis, and F. Nicol. Urban environment influence on natural ventilation potential. *Building and Environment*, 41(4):395–406, 2006.

[17] M. Grosso. Wind pressure distribution around buildings: A parametrical model. *Energy and Buildings*, 18(2):101–131, 1992.

[18] S.R. Hanna and R.E. Britter. *Wind flow and vapor cloud dispersion at industrial and urban sites*. Wiley Online Library, 2002.

[19] R.P. Hosker. Flow around isolated structures and building clusters: A review. *ASHRAE Transactions*, 91(CONF-850606-), 1985.

[20] M. Hussain and B.E. Lee. A wind tunnel study of the mean pressure forces acting on large groups of low-rise buildings. *Journal of Wind Engineering and Industrial Aerodynamics*, 6(3-4):207–225, 1980.

[21] R.W. Macdonald. Modelling the mean velocity profile in the urban canopy layer. *Boundary-Layer Meteorology*, 97(1):25–45, 2000.

[22] H.M. Morris. Flow in rough conduits. *A.S.C.E. Transactions*, 120:373–398, 1955.

[23] T.R. Oke. Street design and urban canopy layer climate. *Energy and Buildings*, 11(1-3):103–113, 1988.

[24] C. Ratti, S. Di Sabatino, R. Britter, M. Brown, F. Caton, and S. Burian. Analysis of 3D urban databases with respect to pollution dispersion for a number of European and American cities. *Water, Air, & Soil Pollution: Focus*, 2(5):459–469, 2002.

[25] M. Santamouris, C. Georgakis, and A. Niachou. On the estimation of wind speed in urban canyons for ventilation purposes, Part 2: Using data-driven techniques to calculate the more probable wind speed in urban canyons for low ambient wind speeds. *Building and Environment*, 43(8):1411–1418, 2008.

[26] J.F. Sini, S. Anquetin, and P.G. Mestayer. Pollutant dispersion and thermal effects in urban street canyons. *Atmospheric Environment*, 30(15):2659–2677, 1996.

[27] B.F. Soliman. Effect of building group geometry on wind pressure and properties of flow. *Dept of Building Science. University of Sheffield. Report BS*, 29, 1976.

[28] R.B. Stull. *An introduction to boundary layer meteorology.* Springer, 1988.

[29] K. Syrios. *Natural ventilation of buildings in urban canyons.* PhD thesis, University of London, 2005.

[30] K. Syrios and G.R. Hunt. Urban canyon influence on building natural ventilation. *International Journal of Ventilation*, 6(1):43–50, 2007.

[31] J. Tsutsumi, T. Katayama, and M. Nishida. Wind tunnel tests of wind pressure on regularly aligned buildings. *Journal of Wind Engineering and Industrial Aerodynamics*, 43(1-3):1799–1810, 1992.

[32] J.W. Verkaik. Introduction to atmospheric boundary layers. *Lecture series: Von Karman Institute for Fluid Dynamics*, 2:1, 2006.

[33] G.N. Walton and W.S. Dols. CONTAM 2.4 User guide and program documentation. *National Institute of Standards and Technology, NISTIR*, 7251, 2005.